Electrochemical study of 3D graphene composites and the creation of ultralight 3D SiC

Submitted by Sakineh Chabi, to the University of Exeter as a thesis for the degree of Doctor of Philosophy in Engineering

August, 2015

I certify that all material in this thesis which is not my own work has been identified and that no material has previously been submitted and approved for the award of a degree by this or any other University.

S. Chabi

Abstract

This research fabricated and tested various graphene-related 1D, 2D and 3D materials. We described how using specifically designed graphene foam (GF) as templates can transform its unique structures and excellent properties to new materials. Graphene, GF, Polypyrrole (PPY), Polyaniline (PANI), PPY-GF, PANI-GF, SiC foam, SiC nanowires and SiC nanoflakes will be described in this thesis.

The chemical vapour deposition method was used to produce graphene and GFs. PPY-GF, PPY, PANI and PANI-GF were prepared by both chemical and electrochemical (Chronopotentiometry) methods. SiC foams were produced by a low-cost carbothermal reduction of SiO with GF, and then the SiC nanoflakes were separated from SiC nanowires and purified via a multistep sonication process.

The synthesised materials were characterised by a variety of techniques such as SEM, EDX, XRD, TEM, Raman, AFM and TGA. The electrochemical properties of the materials were measured in a three electrode cell using cyclic voltammetry (CV), galvanostatic charge-discharge and A.C impedance spectroscopy techniques. The mechanical properties of the GF and SiC foams were investigated by conducting compression tests under in-situ SEM imaging.

The as-produced graphene in this research was few layer graphene with layer number varies from 2 to 15. The GFs was found to be extremely light weight with an average density value of 5 mg cm^{-3}. Using GF as electrode materials for supercapacitors, we obtained 100% capacity retention after 10,000 of charge-discharge cycles. The PPY-

GF composite electrode exhibited an outstanding specific capacitance of 660 Fg^{-1}, which is superior to the performance of most of the existing PPY-CNT, PPY-graphite and PPY-Graphene electrodes reported to date. In contrast to the PPY which shows a big structure degradation and a 30% capacity loss after only hundreds of CV cycles, the PPY-GF composite showed nearly 100% capacity retention after 6,000 cycles of charge-discharge. Our post-test characterisations showed no structural loss for the GF and PPY-GF.

The excellent pseudocapacitive performance of the electrodes was found to be related to three key parameters: the open porosity feature of the GF which provides short pathways for ion diffusion and charge transportation, the dual charge storage mode in the composite, and the excellent mechanical properties of the GF. Due to its high flexibility and void spaces, the GF played successfully the role as a holder and stabilizer for the electroactive materials in protecting them from any structural degradation during the repeated ion intercalation-de-intercalation processes.

In the SiC project, we have successfully created extremely light-weighted SiC foams with a density range of 9-20 mg cm^{-3}, with various shapes, by using the GF as templates. These foams are the lightest reported SiC structures, and they consist of hollow trusses made from 2D SiC and long 1D SiC nanowires growing from the trusses, edges and defect sites. The 1D SiC nanowires, being confirmed as 3C-structure, appeared in a variety of shapes and sizes and are highly flexible; the 2D SiC is hexagonal, and upon breakup the resulting 2D nanoflakes have an average size of 2 μm and a thickness value of 2-3 nm which is 5-9 layers of SiC. They, to the best of our knowledge, are probably the thinnest and largest reported SiC flakes.

Ultimately, in this research we have successfully produced two extremely lightweight and simultaneously strong foams: the GF and SiC foam. We have explored the GFs by efficiently addressing a key issue in the cycle life of energy storage devices, by creating an ideal architecture of such 3D GF-based electrodes. We have developed a completely novel 3D SiC structure made from continuously linked 2D layered SiC reinforced with 1D SiC nanowires. In-situ compression studies have revealed that both the GF and SiC foams can recover significantly, up to 85% in the case of GF, after compression strain exceeding 70%. The SiC foam did not experience any dramatic failure under the compression loads, as do in conventional ceramics. Compared with most existing lightweight foams of similar density, the present 3D SiC exhibited superior compression strengths and an significantly enhanced strength-to-weight ratio.

Contents

Abstract 2
List of tables 14
List of abbreviations 15
List of publications 17
Conference proceedings 18
Acknowledgment 19
Chapter 1 : Introduction 20
Thesis format 22
Chapter 2 : Literature review 24
2.1 Graphene discovery 24
2.2 Graphene structure 25
2.3 Graphene synthesis 29
2.3.1 Exfoliation approach 29
2.3.2 CVD method 30
2.3.3 SiC graphitisation 32
2.4. Substrate effects on the measurement of graphene 33
2.4 Graphene Properties 35
2.4.1 Electronic properties of graphene 35
2.4.2 Mechanical properties of graphene 38
2.4.3 Optical properties of graphene 40
2.4.4 Thermal properties of graphene 41
2.5 Graphene modification 43
2.6 Few layer graphene and graphene foam 46
2.7 Applications of graphene 47
2.7.1 Graphene in electronic devices 47
2.7.2 Graphene in energy storage 49
2.7.4 Graphene foam as electrode support 58
2.8 Other 2D materials 58
2.8.1 SiC: 3D and 2D structures 59

2.8.2 Possibility of 2D SiC 62
2.9 summary 63
Chapter 3 : Experimental methodology and synthesis 65
3.1 Introduction 65
3.2 Sample preparation 66
3.2.1 CVD synthesis of GF 66
3.2.2 CVD synthesis of 2D graphene 67
3.2.3 Chemical and electrochemical synthesis of conductive polymer-GF composites 67
3.2.4 3D SiC preparation 68
3.2.5 2D SiC preparation 68
3.3 Characterisation techniques 69
3.3.1 Scanning electron microscopy (SEM) and energy dispersive X-ray spectroscopy (EDS) 69
3.3.2 Micro–computed tomography (µ-CT) 70
3.3.3 X-ray powder diffraction (XRD) 71
3.3.4 Transmission electron microscopy (TEM) technique 71
3.3.5 Raman Spectroscopy 73
3.3.6 Atomic force microscopy (AFM) technique 74
3.3.7 Thermogravimetric Analysis (TGA) 75
3.4 Mechanical properties measurement 76
3.5 Electrical conductivity measurement 77
3.6 Electrochemical characterisations 77
3.7 Electrode preparation 78
Chapter 4 Graphene synthesis and characterization 80
4.1 Introduction 80
4.2 GF synthesis and characterisations 81
4.2.1 CVD-growth of GF 81
4.2.2 Structural characterisation 83
4.2.3 Electrical conductivity of the GF 88
4.2.4 Electrochemical study of the GF 89
4.3 CVD synthesis of graphene on copper 91
4.4 Summary 94

Chapter 5 : GF-Conducting polymers composites as electrode materials for supercapacitors 95
5.1 Introduction 95
5.2.1 Structural characterisations of PPY-GF1 composites 98
5.2.2 Electrochemical study of the PPY-GF1 composite 104
5.3 Structural and electrochemical characterisation of the PPY-GF2 composite: Effects of the time deposition 118
5.3.4 Effects of the synthesis method 121
5.4 3D PANI-GF electrode: Effect of the electrode materials 122
5.5 Summary 124
Chapter 6 : From graphene to silicon carbide 127
6.1 Introduction 127
6.2 The synthesis of the SiC foam 128
6.3 Structural characterisation of the SiC foam 129
6.4 Growth mechanism of SiC 139
6.5 Structural characterisations of the 2D SiC 140
6.6 Summary 150
Chapter 7 : Mechanical properties of the light-weight graphene foam and SiC foam 152
7.1 Introduction: 152
7.2 In-situ compression of the GF 153
7.3 Effect of the pre-pressing on the mechanical properties of the GF 158
7.4 Mechanical properties of SiC foams 159
7.5 Summary 167
Chapter 8 : Conclusions and future work 169
8.1 introduction 169
8.2 The main achievements 169
8.3 Future work: 171
References 173

Table of figures

Fig 2.1 The orbital structures of graphene..... 26

Fig 2.2 The edge structures in a 2D graphene nanoribbon 28

Fig 2.3 Optical and AFM images of graphene films.. 30

Fig 2.4 SEM images of the first CVD-grown graphene film. 31

Fig 2.5 Optical image of graphene/BN device integrated into STM 34

Fig 2.6 The band structure of graphene. 37

Fig 2.7 Images of the graphene prepared for mechanical measurements. 38

Fig 2.8 Load-displacement curve of the suspended sheet 39

Fig 2.9 The optical properties of graphene. 40

Fig 2.11 Schematic of the Raman optothermal measurement 42

Fig 2.12 (a) LSV curve of various electrodes 44

Fig 2.13 Transmission spectra of G-OTE and ITO 48

Fig 2.14 Ragone plot of various electrochemical energy storage devices..... 51

Fig 2.15 Schematic of an ideal 3D electrode structure 53

Fig 2.16 Charge-discharge performance of NiOOH/Ni electrodes 56

Fig 3.1 Schematic diagram of SEM 70

Fig 3.2 illustration of TEM system 72

Fig 3.3 Energy transitions for elastic and inelastic Scattering 73

Fig 3.4 A schematic of an AFM 75

Fig 3.5 A photograph of the GF during mechanical test 77

Fig 3.6 A photograph of the electrochemical device. 78

Fig 3.7 Mounting GF on a working electrode by using a Teflon holder..... 79

Fig 4.1 (a) High resolution SEM image of graphene on Cu and (b) FESEM image of graphene on Ni substrate 81

Fig 4.2 Schematic processes for the preparation of the GF 83

Fig 4.3. (a) µ-CT scan of Ni template. The inset shows Top volume of the CT scan of the Ni from. (b) SEM image of the GF. 83

Fig 4.4 (a-c) SEM images of GF and (d) a photograph of a bended GF..... 84

Fig 4.5(a) EDS spectrum of the GF and (b) XRD pattern of the GF 85

Fig 4.6 TGA profiles. (a) The GF-Ni, and (b) pure GF. 86

Fig 4.7 Raman spectrum of the GF 87

Fig 4.8 TEM images of the GF.(a) low resolution TEM image and (b) HRTEM of the produced graphene 88

Fig 4.9 Electrical conductivity measurement of the GF. 88

Fig 4.10 cyclic voltammetry of GF (a, b) at scan rate of 0.1 Vs^{-1} 90

Fig 4.11 SEM image of the graphene grown on a Cu foil 92

Fig 4.13 Raman spectra of graphene on Cu. 93

Fig 5.1 Schematic of Pyrrole polymerisation through monomer oxidation process. 97

Fig 5.2 TGA profiles of PPY-GF1, GF and PPY. 99

Fig 5.3 SEM images of GF, PPY and PPY-GF1..... 100

Fig 5.4 TEM images of the PPY-GF. 101

Fig 5.6 Raman spectra of the GF, PPY and PPY-GF1. The inset is an enlarged Raman spectrum of the PPY. 102

Fig 5.7 CV curves of different electrodes in 0.5 M KCl at different scan rates. (a) GF, (b) PPY, and (c) PPY-GF1. 105

Fig 5.8 Galvanostatic charge-discharge curves of the electrodes. (a) GF at 1 Ag^{-1}, (b) PPY at 1.5 Ag^{-1}, (c) PPY-GF1 at 0.33 Ag^{-1}, (d) PPY-GF at 1.1 Ag^{-1}, and (e) PPY-GF1 at 5.2 Ag^{-1}..... 108

Fig 5.9 Nyquist plots of different electrodes in 0.5 M KCl: (a) GF, (b) magnified Nyquist plot of GF at high frequencies, (c) Nyquist plot of the PPY, and (d) Nyquist plot of the PPY-GF1 112

Fig 5.10 CV curves of the GF, PPY and PPY-GF1 after thousands of cycles in 0.5M KCl at a scan rate of 100 mV s^{-1}..... 114

Fig 5.11 SEM images of the GF after 10000 cycles of CV test, and (c, d) SEM images of PPY-GF1 after 6000 cycles of CV test..... 116

Fig 5.12 Nyquist plots of the PPY-GF1 electrode; (a) in 0.5 M H_2SO_4, and (b) in 0.5 M KCl. 117

Fig 5.13 The morphology and electrochemistry characterisation of the PPY-GF2 electrode: (a) SEM image, (b) the CV curve, (c) the Nyquist plot at OCP, and (d) CV curves showing the cycle stability at a scan rate of 50 mVs^{-1}..... 120

Fig 5.14 (a) Galvanostatic charge-discharge curve of PPY-GF3 at 1 Ag^{-1}, (b) the Nyquist plot at OCP of PPY-GF3. 121

Fig 5.15 (a) CV curve of PANI-GF at scan rate of 100 m V s^{-1}, and (b) Nyquist plot of PANI-GF in 0.5 M H_2SO_4 and frequency range of 100 K Hz- 100 m Hz..... 123

Fig 5.16 Schematic of the charge-discharge process in PANI. 124

Fig 6.1 Schematic for the preparation of the SiC. (a) SEM image of GF and (b): micro-ct image of 3D SiC 128

Fig 6.2 SEM image and XRD profile of SiC sample prepared at 1380 °C. 130

Fig 6.3 TEM images of SiC samples prepared at 1380 °C. (a) HRTEM of (a) SiC flakes and (b) SiC nanowires 131

Fig 6.4 XRD profiles of a characterised SiC sample before (a) and after (b) etching. 132

Fig 6.5 Morphological and structural characterisations of the foam. (a) SEM image of the GF, (b) Micro-CT image of the SiC foam, (c) SEM image of the SiC foam, (d, e) High magnification SEM images of the SiC foam, and (f) XRD profile of the SiC foam. 133

Fig.6.6 EDS spectrum of the 3D SiC foam showing 134

Fig.6.7 Raman spectrum of the 3D SiC foam 135

Fig 6.8 Thermal properties of the SiC foam. (a) TGA profile of the SiC sample in air; (b) XRD profile of the sample after TGA experiment. 136

Fig 6.9 TEM images of the SiC. (a, b) Low magnification TEM images showing the 2D SiC sheets and 1D SiC nanowires (c) HRTEM image of a SiC nanowire and (d) TEM image of 2D SiC flakes 137

Fig 6.11 High resolution SEM and TEM images. (a) SEM image of SiC nanowires and (b) HRTEM image showing mainly twinned nanostructure of an individual SiC nanowire. 138

Fig 6.12 Morphological and compositional results of the 2D SiC flakes. (a) Optical microscopy image, (b) and (c) SEM images, and (d) EDS result. 141

Fig 6.13 TEM images of the 2D SiC. (a-c) low resolution TEM images of SiC flakes, (d, e) TEM images, and (f) NBD pattern of the SiC. 143

Fig 6.14 Line elemental scan of the 2D SiC. (a) Mixed scan of Si, C and O. The inset in (a) shows a TEM image of the scanned SiC sheets. (b) Individual line scanning of C, (c) individual line scanning of (Si), and (d) individual line scanning of O. .. 145

Fig 6.15 Raman results of the 2D SiC. (a) Spectroscopic Raman mapping of SiC flake taken at 10 x 50 objectives, (b) Raman spectrum of the flake shown in (a).146

Fig 6.15 Raman spectra of 3 polytypes of SiC 147

Fig 6.16 AFM results of the SiC sample. (a) AFM image of the tested SiC sample showing a large SiC flake and some SiC nanowires across the horizontal scan line, (b) the height-length profile of the SiC structures shown in (a), (c) AFM image of a single SiC flake, and (d) the height-length profile of the flake shown in(c). 149

Fig 7.1In-situ SEM images of the GFa during compression test. (a) before compression, (b) under maximum load, and (c) unloading stage. 154

Fig 7.2 High magnification SEM image of GF_a before the compression test (a), and under 0.88 N load (b). 155

Fig 7.3 In-situ SEM images of the GF_b under compression cycles. 156

Fig 7.4 In-situ SEM images of the GF_b under compression tests. 157

Fig 7.5 Stress-strain curves of the GFs. (a) GF_a (ρ: 3-5 mg cm^{-3}), (b) GF_b (ρ: 8 mg cm^{-3}) 157

Fig 7.6 Load-strain curves of (a) non-pressed GF and (b) pressed GF..... 159

Fig 7.7 In-situ SEM images of the SiCa during the compression test. 161

Fig 7.8 Compressive stress-strain curves of the SiC foams. 162

Fig 7.9 In-situ SEM images of the SiC_b during the compression test. (a) Pre-compression, (b) under 1.55 N load, (c) under 6 N load, and (d) under 17.5 N load. 163

Fig 7.10 (a) The recorded stress-strain curve of the SiC_b foam and (b) a magnified strain-stress plot of the SiC_b. 164

Fig 7.11In-situ SEM images of the SiC_b under testing. (a) Under maximum load, and (b): unloading stage..... 165

Fig 7.12 High magnification SEM image of the SiC_b 166

List of tables

Table 2.1 Atomic parameters of different SiC allotropes 60

Table 5.1 Preparation conditions of various electrodes. 97

Table 5.2 Specific Capacitance of the electrodes at different current densities.109

List of abbreviations

AFM	Atomic force microscope
CVD	Chemical vapour deposition
CP	Conductive polymer
CV	Cyclic voltammetry
EDX	Energy dispersive x-ray
EES	Electrochemical energy storage
EESS	Electrochemical energy storage systems
GF	Graphene foam
LED	Light emitting diode
OCP	Open circuit potential
PMMA	Poly methyl meta acrylate
PDMS	Polydimethylsiloxane
PPY	Polypyrrole
PANI	Polyaniline
TEM	Transition electron microscopy
TGA	Thermogravimetric analysis
TPa	Tera Pascal (10^{12} pascals)
Sccm	Standard cubic centimetre per minute
XRD	X-ray diffraction

List of publications

1-**Chabi, S**., Peng, C., Hu, D., & Zhu, Y. (2014). Ideal Three-Dimensional Electrode Structures for Electrochemical Energy Storage. Advanced Materials, 26(15), 2440-2445

2-**Chabi, S**., Peng, C., Yang, Z., Xia, Y., & Zhu, Y. (2015). Three dimensional (3D) flexible graphene foam/polypyrrole composite: towards highly efficient supercapacitors. RSC Advances, 5(6), 3999-4008.

3-Yang, Z., Yan, C., Liu, J., **Chabi, S**., Xia, Y., & Zhu, Y. (2015). Designing 3D graphene networks via a 3D-printed Ni template. RSC Advances, 5(37), 29397-29400.

4- **Chabi, S.**, et al., Ultra-light SiC foam: a novel super strong structure (Submitted to ACS NANO).

Conference proceedings

1- **Chabi, S**., Yang, Z., Peng, C, Xia,& Y, Zhu, Synthesizing 3D graphene foam with direct etching for energy storage applications, Graphene 2014 Toulouse, France

2- **Chabi, S**., Xia, Y, & Zhu, Y, The creation of graphene-Polyaniline nanocomposites for supercapacitor applications, The 21st Joint Annual Conference of CSCST-SCI Oct 2014, University of Surrey, UK

3- **Chabi, S**., Chong, H., Xia,& Y, Zhu, Graphene-based nanocomposites for energy storage applications, 7th European Summer School on Electrochemical Engineering ,(ESSEE) 2015, Leeuwarden, the Netherlands

4- **Chabi, S**., Chong, H., Xia, Y, & Zhu, Y, Three dimensional Silicon carbide structures: Catalyst free synthesis, 12th International Conference on Material Chemistry (MC12)20 - 23 July 2015 University of York, UK

5- **Chabi, S**., Chong, H., Xia, Y, & Zhu, Y, Binder Free Graphene- Based Electrodes with Excellent Pseudocapacitive Performance, ECS 26-31 July 2015 Glasgow, Scotland

Acknowledgment

For the individuals who paved the way for this research and who inspired and supported me during my PhD study.

This thesis is dedicated to my family, on whose shoulders I stand.

In full gratitude I would like to acknowledge my supervisor Professor Yanqiu Zhu, whose encouragement and care were sometimes all that kept me going.

I am grateful to Dr Chuang Peng who gave me the chance to carry out my PhD programme at the University of Exeter, also thank the college for the full Scholarship.

Thank Dr Yongde Xia for his advices, Dr Hong and Dr Lesley for their assistance with imaging suite facilities.

Thanks also to our collaborators in Imperial college of London and Trinity College Dublin for helping with mechanical measurement and n-doping experiments.

I am grateful to Prof Geoffrey Nash and Dr Loretta Lawton for assistance in the electronic measurements, and to Ms Angela Elliott in the Geophysics group for helping with SiC etching.

Thanks to all the fellow post-docs and PhD students I have worked with: Dr Zhuxian Yang, Dr Chunze Yan, Ms. Bahareh Yazdani, Mr. Binling Chen, Ms. Kunyapat (Ploy) Thummavichai, Mr. Nannan Wang and Mr. Laicong (Keven) Deng. It was a great pleasure to work with you all.

Chapter 1 : Introduction

Graphene has lots of superior properties that are important for materials science, physics, electronic and chemistry. It has a large theoretical surface area of 2630 m^2 g [1], excellent thermal conductivity (5000 W m^{-1} k^{-1}) [2], very high intrinsic mobility (200 000 cm^2 v^{-1} s^{-1}) [3], and a very high Young's modulus of 0.5 TPa [4]. Therefore, extensive research worldwide has been invested in the fabrication and modification of graphene, to take advantage of these remarkable values to develop high performance graphene-based devices.

This wonder material has the potential to replace many materials including silicon, indium tin oxide (ITO), titanium oxide, plastic, and glass. It has been used to make ultrafast transistors as electrons can travel along the material at extremely high speeds [5]. It could also be used to replace the expensive and brittle ITO to create flexible touch screens [6]. Further, graphene beats diamond in the thermal conductivity, and is about 200 times stronger than steel.

However, despite all these astonishing properties and promises, there are some intrinsic issues with graphene that need to be overcome. On top of the zero-band gap issue which restricts its full applications in electronic devices, its principle structure or single layer one atom thick feature does not suit many applications. Instead, few layer graphene can contribute much more efficiently to device performance.

A 3D network of few layered curved graphene or graphene foam can transform efficiently the merits of 2D graphene to the macroscopic level. By increasing the number of layers, the thermal, mechanical and electronic properties of graphene

changes correspondingly, and it also exhibits many advantages over the bulk graphite and other materials in terms of thermal and mechanical properties [7].

In a 3D network of graphene, one can take advantage of both the strong in-plane covalent bond and the π-π stacking between layers. While the covalent bonds are interesting by nature as they are responsible for the mechanical strength of the materials, the non-covalent π-π interactions are attractive too as they allow fast movement between graphene layers. They can be used for both structural modifications such as engineering specific 3D architectures, and for generating new 1D, 2D and 3D materials. Thus it offers more chances for the so-called graphene revolution.

With this in mind, this thesis investigates the use of specifically engineered 3D graphene networks to address some concerns with energy storage devices, and to develop new structured materials.

Energy density, power density and cycle life are the three most important parameters of electrochemical devices. Despite the astonishing properties of single layer graphene such it its high surface area, high flexibility and high electrical conductivity, still much in-depth research are needed to allow this truly 2D materials to replace the conventional electrode architecture. Between existing concerns and the promising future of graphene, we decided to explore the possibilities of few layer graphene for further development in the electrode architecture

Strictly speaking, this PhD research seeks to tackle the problem of cycle life by designing new electrode architectures with minimum structural loss after long term charge-discharge cycles. The proposed 3D graphene-based architectures are also

expected to bridge the gap between capacitor and battery, showing minimum compromise between the specific energy density and the specific power density.

Further exploration of the few layer graphene foams will be focused on using them as the starting material for the production of new materials, specifically SiC, as such new possibility could emerge for generating 2D and 2D SiC from these graphene networks. It is likely that under optimum experimental conditions graphene flakes could transform to SiC nanoflakes.

Thesis format

The thesis has been structured to include 8 chapters including the Introduction. Chapter 2 provides an overview from the literature and research inherent in the graphene synthesis and applications, with particular focus on the energy storage. Chapter 2 also identifies the structural relations and similarities between graphene and SiC, and the possibility of producing novel SiC structures. Chapter 3 describes the laboratory techniques that have been used for this project, focussing on sample preparation methods and the types and operation of instruments used.

The main research work is presented in Chapters 4-7. Chapter 4 describes the synthesis and general structural characterisation of the as-produced GFs. The application of GFs in supercapacitor system and their role as the scaffold in various 3D electrodes are discussed in Chapter 5, with focus on the GF-Polypyrrole composites as the electrode for supercapacitors.

Chapters 6 and 7 will focus on the SiC study. The newly explored phase of 3D SiC, the ultra-thin 2D SiC nanoflakes and the 1D nanowires will be presented in Chapter 6.

Chapter 7 investigates the mechanical properties of both the GF and SiC foams, using in-situ compression technique.

Finally, Chapter 8 highlights the new knowledge gained from this thesis and recommends potential avenues for future research.

Chapter 2 : Literature review

2.1 Graphene discovery

It was long believed that nature forbids the growth of large, free-standing 2D dimensional crystals, and that it was impossible to thermodynamically stabilize a one atomic thick layer. It was postulated that one could grow flat molecules into nm-sized particles and crystallites, but as their lateral size increased, the phonon density would force the 2D crystallites to morph into a variety of stable 3D structures [5]. Stabilising through a supporting substrate was the main accepted solution for stabilising a 2D material, and the so-called quasi-two dimensional films were believed to relax themselves on supporting substrates [8]. Despite all earlier theories, and the fact that the history was against 2D materials, in 2004, a very simple approach to obtain graphene led to a revolution in the 2D materials field.

Andrew Geim and Konstantin Novoselov, at the University of Manchester, joint winners of the Nobel Prize in Physics in 2010, first isolated single layer graphene, from 3D graphite by using a micromechanical cleavage strategy. By using the top-down approach and starting with 3D crystals, the researchers avoided all the issues associated with the stability of low-dimensional crystallites [9]. The resulting graphene sheet was attached to the SiO_2/Si substrate by only Van der Waals forces, and hence was presented as free-standing 2D materials after etching away the substrate [10].

2.2 Graphene structure

Graphene is a 2D planner sheet of sp^2 hybridized carbon atoms arranged in an hexagonal crystal lattice with the C-C bond length around 0.142 nm. Its extended honeycomb network is the basic building block of several carbon allotropes. It can be assembled and stacked to form 3D graphite, rolled to form 1D nanotubes, and wrapped to form 0D fullerenes [11]. Recently, a phase transformation from graphene in thin diamond film was also reported in the literature [12]. Compared with other carbon allotropes, graphene has showed a wide range of unusual features and properties which can be explained by understanding the crystal structure, its sp^2 hybridisation and its unique physics laws.

In a graphene sheet, carbon atom bonds covalently to its neighbour atoms and due to the one atom thickness of the material, sp^2 hybrid needs to take place to stabilise the honeycomb network. The sp^2 hybridization between one S orbital and two P orbitals, P_x and P_y, leads to a trigonal planar structure with the formation of a σ bond between carbon atoms that are separated by a distance of 0.142 nm, Fig 2.1. The σ band is responsible for the robustness of the lattice structure in all carbon allotropes.

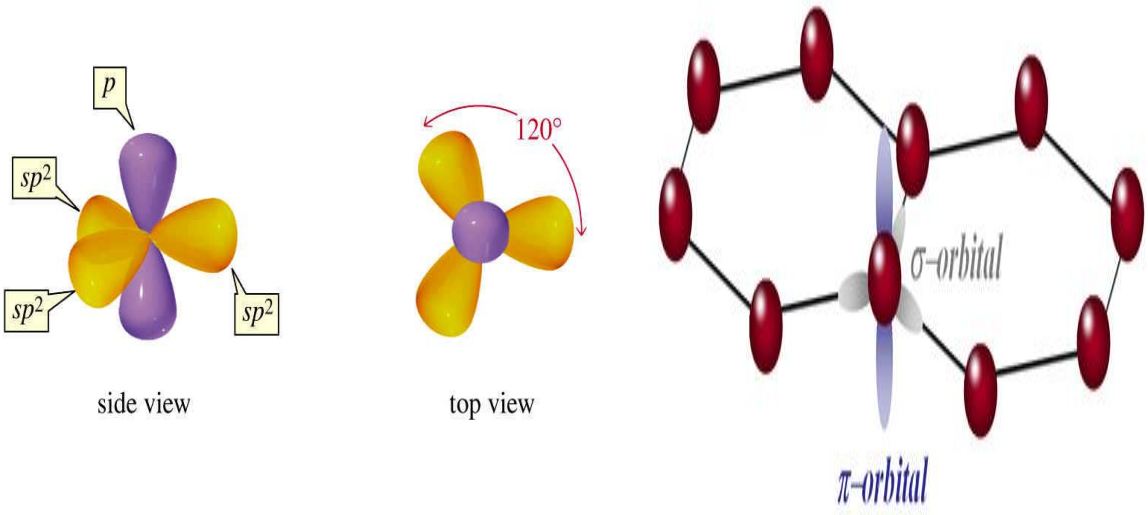

Fig 2.1 The orbital structures of graphene[11] .

The unaffected P orbital, P_z, which is perpendicular to the planar structure, can bind covalently with the neighbouring atoms, which leads to the formation of a π band. The π orbitals are half-filled and delocalized throughout the structure, such that all conjugated chemical bonds are equivalent [13,14]. The long-range π-conjugation in graphene yields extraordinary thermal, mechanical, and electrical properties [10]. The stability of the extended, delocalized π-system and the resonance network provides the basal plane of graphene with the required chemical stability [13].

From a chemist's point of view, graphene can be treated as a surface material without a bulk contribution [13], and indeed it is. Being one atom thick, every atom in a graphene film is at the surface and contacts directly with the surrounding environment, which opens up numerous opportunities for graphene modifications and for new device fabrications [15]. However, since it is surface materials, this could also result in a fast degradation for the devices.

Regarding the graphene reactivity, it has been shown that its basal plane is fairly stable, and it is the edges and defect sites that are mostly involved in reactions [16]. The edge structure of a 2D graphene plays a significant role in the reactivity of the material, and can be used to tune its electronic behaviour and thus properties [17].

Generally, graphene grain boundaries are defined as defects (represented with D peak in a Raman spectrum), and it is believed that they degrade the electrical, thermal and mechanical properties of a graphene film [18]. However, the challenge is that the edge structures and chemical terminations of graphene synthesized by various methods are unknown, and are not easily controllable [19].

Two types of edge structures have been studied for graphene: the zigzag and the armchair. Fig 2.2 shows a schematic of these edges. Both edges have a regular hexagonal structure and they are defined by the orientation of the hexagons relative to the ribbon length. Thermodynamically, armchair edges are generally more stable than zigzag edges due to a less aromatic feature in the latter [20]. In the zigzag edges, there is a nonbonding edge state which is the origin of electronic, magnetic and chemical activities. Compared with armchair edges, zigzag edges also have a higher electron density of states near the Fermi level [21]. Armchair edges do not have such a feature in their structure.

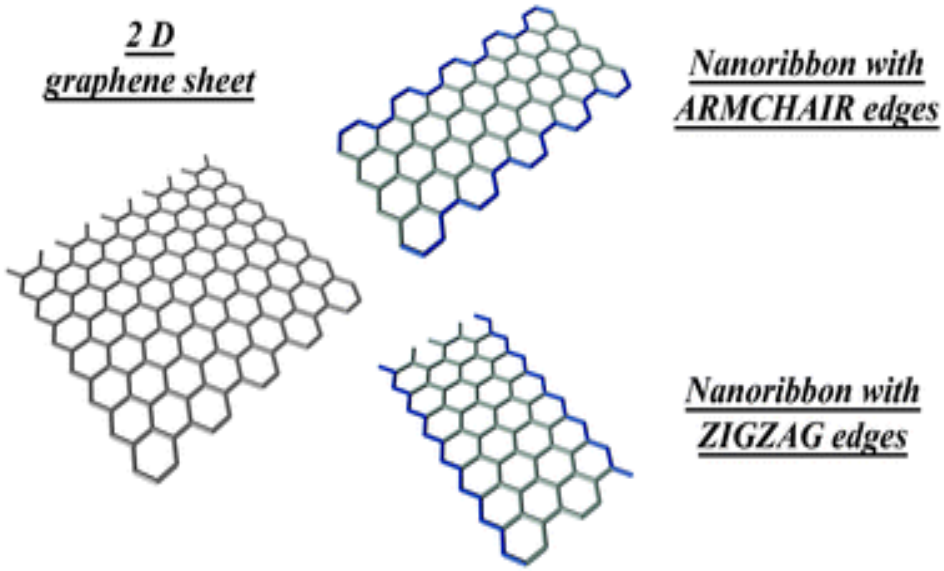

Fig 2.2 The edge structures in a 2D graphene nanoribbon [21].

Other edge types with polygonal structures, *e.g*. pentagon and heptagon, were also reported [24]. There is a less discussed edge structure, called the 'reczag' edge which is the reconstructed zigzag edge. Theoretical calculations have shown that zigzag edges are metastable and a planar reconstruction into pentagon-heptagon configurations spontaneously takes place at room temperature [22].

It has been shown that the crystallographic orientation in graphene significantly alters its overall properties, and further affects the performance of graphene-based devices [17]. Based on these investigations, a good understanding of the graphene edge structures is critical, and should be considered during designing any graphene modification experiments or device fabrications. An effective way of limiting the negative effects of the edge on device performance is to reduce the number of the edges in graphene by using large rather than small graphene flakes with lots of

uncontrolled grain boundaries [18]. Using the D peak in a Raman spectrum is a good way of assessing the level of defects in graphene.

2.3 Graphene synthesis

Several techniques have been successfully developed in the past years for graphene synthesis, of which the mechanical exfoliation [23], chemical vapour deposition (CVD) on transition metals [24], GO reduction [25], and the SiC graphitisation [26], are the most notable ones. The quality, quantity, morphology and properties of the resulting graphene vary significantly from one method to another, and each approach has its own advantages and drawbacks.

2.3.1 Exfoliation approach

The mechanical cleavage or exfoliation technique was first used by the Manchester team to isolate a 2D graphene sheet from the highly oriented pyrolytic graphite. The resulting sheets are shown in Fig 2.3 [27]. Since that time, this method has been widely used to produce graphene. To exfoliate a single-layer sheet, the Van der Waal attraction between the first and second layers must be overcome without damaging any subsequent sheets. The main advantage of this technique is the high quality of the produced graphene. Despite huge progresses in alternative methods, this simple mechanical exfoliation with tape still produces one of the highest quality graphene flakes. However, this method is un-scalable, only capable of producing very limited quantities [27]. Alternative approaches for the mass production of graphene are thus required.

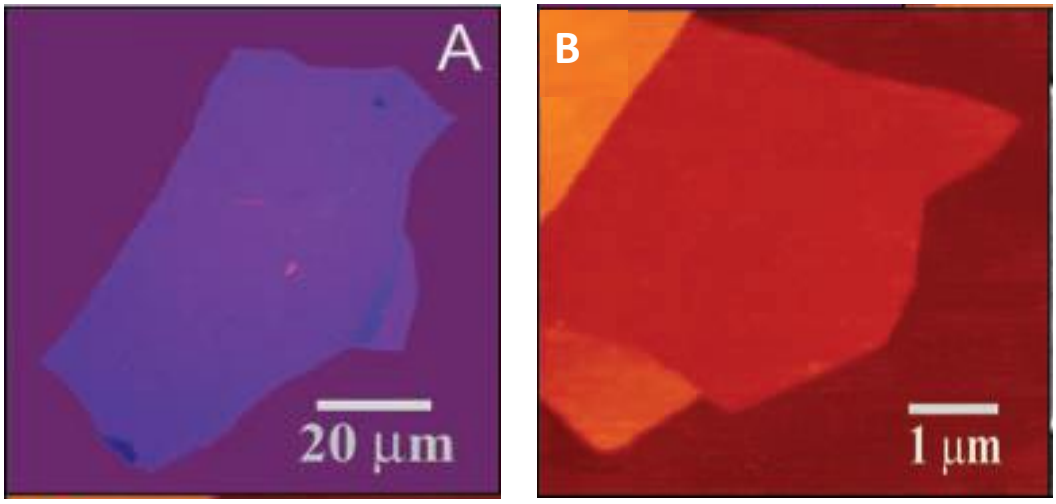

Fig 2.3 Optical and AFM images of graphene films prepared by mechanical exfoliation. (A) Optical (in normal white light) picture of a relatively large multilayer graphene flake with a thickness of 3 nm on top of an oxidized Si wafer. (B) AFM image of a single layer graphene [27].

2.3.2 CVD method

Shortly after the first mechanical exfoliation of graphene, CVD method became extensively used for the production of graphene [16,28-30]. During the process, the nucleation and growth of graphene usually occur through the exposure of a transition metal surface to a hydrocarbon gas, under specific gas pressure and temperature conditions [26]. The first CVD graphene was grown on 25 μm thick Cu foils [26]. It has been shown that the growth of graphene on Cu occurs via a surface adsorption mechanism, a self-limiting process that mostly yields single layer graphene rather than multilayer ones [31].

A typical growth procedure is: (1) loading the tube with the Cu foil and heating to 1000 ºC under continuous flow of H_2 and Ar; (2) stabilizing the Cu film at the desired temperatures, up to 1000 ºC, and introducing the carbon source; (3) cooling down the

furnace to the room temperature; (4) coating the surface of graphene-Cu with PMMA or PMDS to protect the graphene; and finally (5) etching away the Cu foil in an aqueous solution of iron nitrate. The etching time was found to be a function of the etchant concentration, and the area and the thickness of the Cu foils. After that, the produced graphene can be transferred to a suitable substrate, such as SiO_2/Si, for characterisations and for device fabrications [24,32,33].

Fig 2.4 presents images of the first synthesised graphene by the CVD method. As shown, a large area, 30 inch in length, single layer graphene has been successfully prepared by using a flexible copper substrate [33].

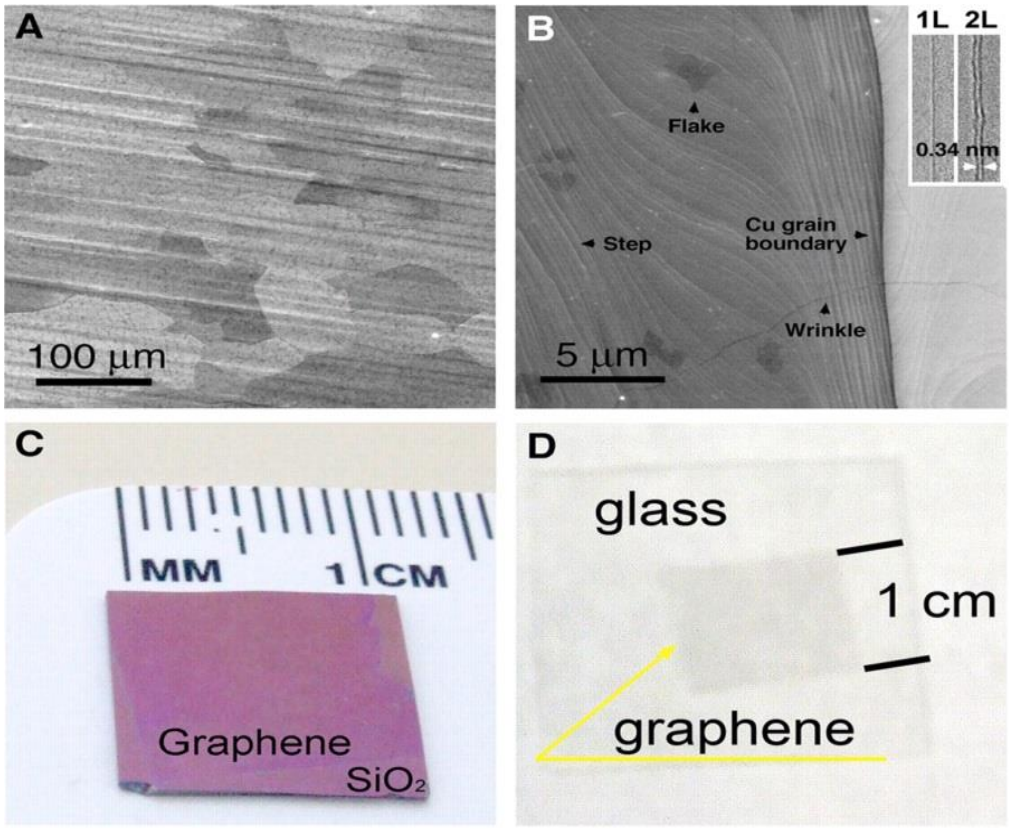

Fig 2.4 SEM images of the first CVD-grown graphene film [32].

The growth of monolayer graphene on single crystalline transition metals such as Co, PT, Ir, Ru, and Ni, has been reported in the literature [26]. Furthermore, polycrystalline

Ni and Cu foams have also been used as templates for the CVD graphene growth. With specifically designed features of the Ni foam, such as porosity level, density and thickness, together with optimised process parameters including the reaction time and concentrations of the carbon source, the graphene products can be engineered to exhibit desired features [26]. Compared with the Cu substrate which yields single layer graphene, the Ni template generally results in the formation of few layer graphene, especially at the grain boundaries.

2.3.3 SiC graphitisation

High quality graphene sheets were also prepared by a SiC graphitization technique, using both ex-situ and vacuum SiC annealing procedures[17,28]. By controlling the crystal orientation of the SiC, one can control the number of graphene layers. The growth on the C-face of SiC results in the formation of a few layer graphene with very high mobility; whilst the growth on the Si-face of SiC yields single and double layer graphene [15].

One of the main advantages of this method is the avoidance of transferring the formed graphene to an insulating substrate for further device development, as SiC is an extrinsic semiconductor. However, the high cost of SiC and the relatively small size of available SiC wafers, significantly limit the use of this technique for large scale applications [15,26].

Ultimately, it is worth noting that chemical routes, such as CVD and GO reduction [33-35], are preferred over the micro-cleavage or SiC graphitisation for the large scale production of graphene.

2.4. Substrate effects on the measurement of graphene

Since the discovery of graphene, the search for efficient substrates that improve the measurement of monolayer graphene has been the main focus of many researchers, as it has been shown that the underlying substrate unavoidably affects the charge transport properties of graphene.

So far, graphene layers have been prepared on a variety of substrates, including SiO_2/Si, SiC, metal surfaces, and mica [36]. The first graphene reported in 2004 was deposited on a SiO_2/Si substrate. The 300 nm thick SiO_2 layer deposited between the Si wafer and the graphene layer has two functions. First, its thickness was optimized to maximize the optical contrast between the graphene flakes and the substrate, in order to allow the flake being observed. Second, the SiO_2 layer acted as a gate dielectric. However, due to the high thickness of the SiO_2 layer, the resulting device transconductance was very low, severely degrading the device properties [15].

In the case of SiO_2, the most commonly used substrate for graphene devices, the presence of impurities induces charge density fluctuations that lead to a reduction in electronic mobility. Suspension of graphene sheets over a hole has been successfully attempted to remove the unwanted effects of SiO_2 substrates, but these devices are difficult to fabricate and to measure using scanning probe techniques [36].

BN substrates however have been reported to result in extraordinarily flat graphene layers that display microscopic Moire patterns arising from the relative orientation of the graphene and BN lattices [38,39]. Transport experiments have shown that the graphene/BN combination generated a higher mobility than that of graphene/SiO_2 [37,38]. The gate-dependent dI/dV plots of graphene on the BN substrate exhibit spectroscopic

features that are sharper than those obtained for graphene on SiO_2, which was attributed to the more homogenised charge density and improved local electronic properties [36]. Fig 2.5 illustrates the graphene/BN device integrated into an ultrahigh vacuum STM.

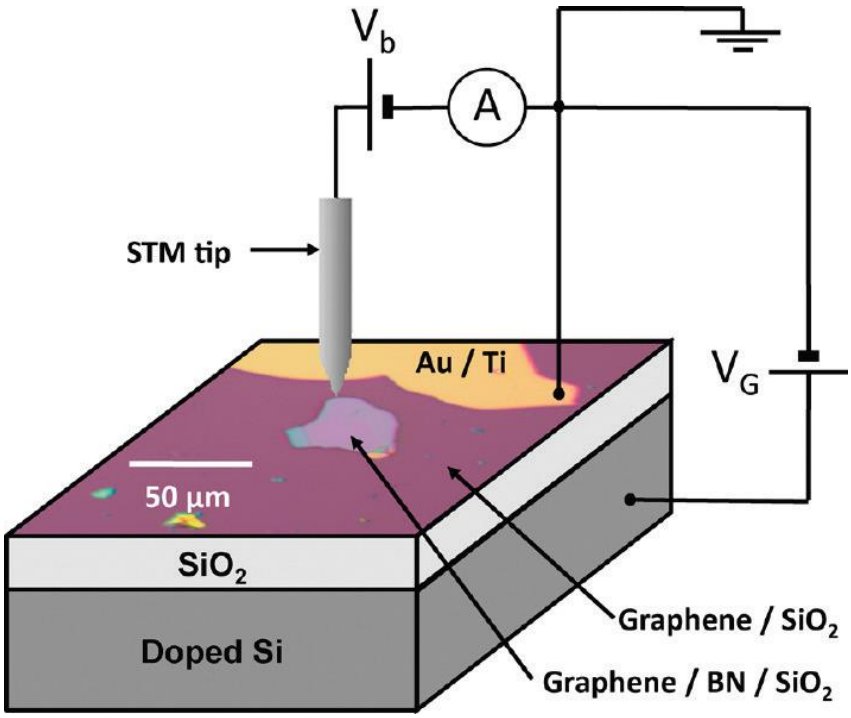

Fig 2.5 Optical image of graphene/BN device integrated into STM. The graphene is grounded via a gold/titanium electrode [36].

By carefully controlling the graphene-substrate interface, an optimised substrate can be designed, which allows for proper characterisations with a minimum contribution from the substrate [15]. A comparative investigation between existing substrates suggests that preparing suspended graphene on an appropriate hole, is the best approach for eliminating substrate inferiors.

2.4 Graphene Properties

Graphene is a truly 2D material with very rich physical and chemical properties. Owing to its atomic level thickness, the 2D hexagonal carbon lattice possesses remarkable electrical and thermal properties. Graphene also has a robust but flexible structure with unusual phonon modes that do not exist in ordinary 3D solids [13,14]. Interestingly, these properties can be easily tuned by chemical doping, structural modification, the application of electric and magnetic fields, and by the addition of extra layers [14].

2.4.1 Electronic properties of graphene

The most explored aspect of graphene is its electronic properties, and some of its key features make it truly unique and different from any other materials. First, graphene is an interesting mix of a semiconductor zero density of states and a metal. Further, the electrons in graphene lose their effective mass and almost insensitive to disorder and electron-electron interactions, and can be described by a Dirac-like equation instead of by the Schrödinger equation used in traditional semiconductors [5,14]. This very low effective mass is responsible for a very high electron mobility which exceeds 200,000 cm^2/Vs at T = 5 K and 100,000 cm^2/Vs at T = 240 K in suspended graphene, the highest ever reported for any semiconductor. The electron mobility of graphene is up to 150 times greater than its electronic opponent Si. The actual velocity is equivalent to about 1/300 of the light velocity [17,19,39]. The symmetry of the honeycomb lattice structure also confers very unique transport properties to graphene [13]. Its sheet resistance has been measured by both four probe and two probe systems, and resistance values of 125 $\Omega\ cm^{-1}$ and 30 $\Omega\ cm^{-1}$ at 97.4% and 90% transparency were reported [30,33].

Furthermore, the electronic structure of graphene nanoribbons has been predicted to depend sensitively on the crystallographic orientation of their edges. Some of the reported edge dependant features are: zigzag-edges with 7 – 8 nm average width are metallic, owing to the presence of zigzag edge states; nanoribbons with a higher fraction of zigzag edges exhibit a smaller energy gap than a predominantly armchair-edged ribbon of similar width [17].

2.4.1.1 Band gap problem in graphene

One of the very challenging facts about graphene is its zero-bandgap, in which the conduction and valence bands touch each other at a point called the Dirac point [15]. Being only one atom thick, graphene holds big promises for electronic applications, as it could be performed perfectly for high frequency applications. However, its bandgap structure issue needs to be overcome first. Fig 2.6 illustrates the band structure of graphene.

In usual semiconductors, the electron motion is described by an effective-mass approximation, in which the wave function has vanishingly small amplitudes at the boundary. In graphene, however the condition that the wave functions vanish at the boundary cannot be imposed. As a result, the amplitudes of the wave functions are almost the same at the edges as on the inside of a graphene ribbon [39].

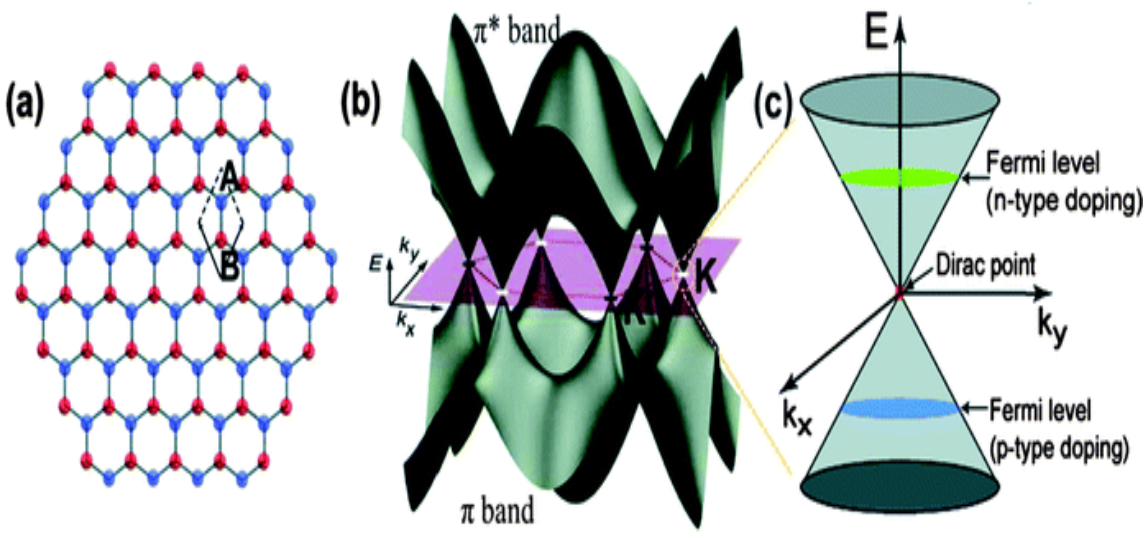

Fig 2.6 The band structure of graphene. (a) hexagonal lattice of graphene (b) and (c) illustrations of the band gap structure [40].

Various attempts to introduce a band gap for the purpose of converting graphene into a semiconductor have been documented. Owing to the proven dependency of the band gap to the crystal orientation at its edges, one of the efforts was to create an effective electronic active edge on graphene ribbons, as it was believed that graphene nanoribbons with narrow widths (below 20 nm) can generate such a bandgap [21,39]. However, the edges of the ribbons fabricated by conventional lithography techniques suffered from a disordered structure and were far from the ideally well-defined band gap. Similar studies tried to engineer the band gaps by fabricating nanoribbons for graphene transistors, but the results were not very successful [15,30].

An alternative approach to open the band gap was to apply vertical electric fields into a bilayer graphene. Although this method has been successful in opening optical bandgaps (100 – 200 m eV), the electrical bandgap has been much smaller than

expected (< 20 m eV), and more work is needed to understand the full potential of this technology [15,30].

2.4.2 Mechanical properties of graphene

Graphene has been recognized as the strongest, stiffest, and the most stretchable crystal, up to 20% elasticity [10], in the world. It has been extensively investigated as reinforcements for many purposes, including making composites, and for energy storage materials [41]. One interesting technique for evaluating the mechanical property of single layer graphene is the AFM-assisted experiments by suspending it over open holes, so that substrate influence can be eliminated [42,43]. As shown in Fig 2.7, the graphene sheet was stretched tightly across the hole opening. Values of 42 N m^{-1} and 1.0 T Pa were reported as the intrinsic strength and Young's modulus, respectively. These results confirmed experimentally the excellent mechanical strength of a free standing graphene [28].

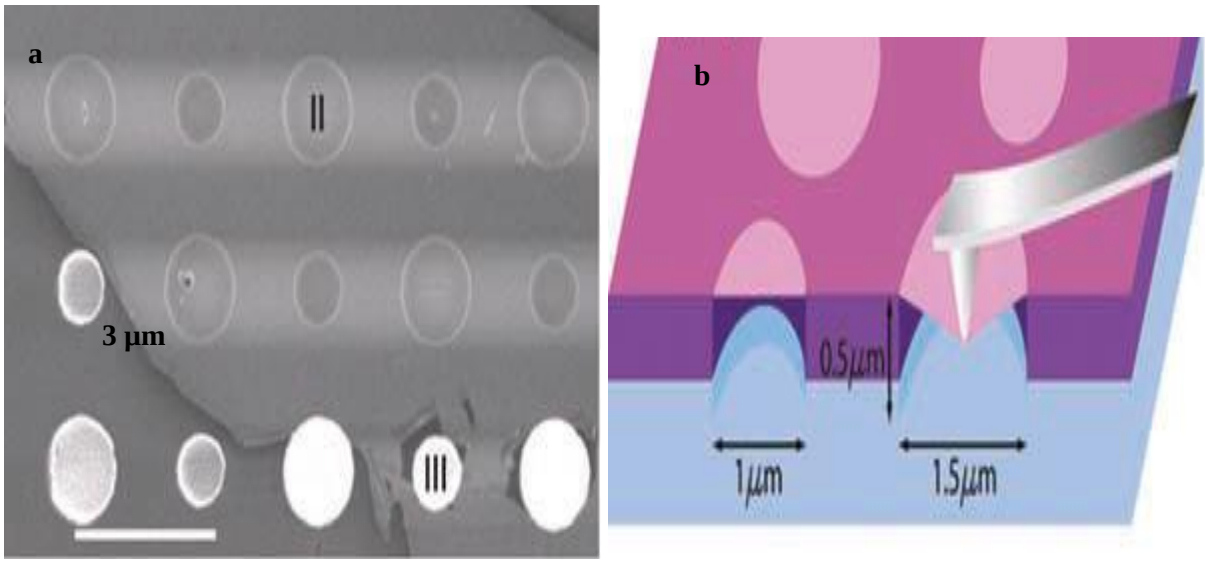

Fig 2.7 Images of the graphene prepared for mechanical measurements. (a) An SEM image of suspended graphene on a SiO_2/Si substrate, and (b) schematic of AM nono-indentation experiment on graphene [28].

Similar AFM nanoindentation study on few layer graphene (less than 5 layers) reported 0.5 TPa as the Young's modulus for sheets with a thickness of 2 - 8 nm, at a high stretching rate of 100 nm s^{-1} [42]. Fig 2.8 shows the load-displacement curve of the measured graphene sheets.

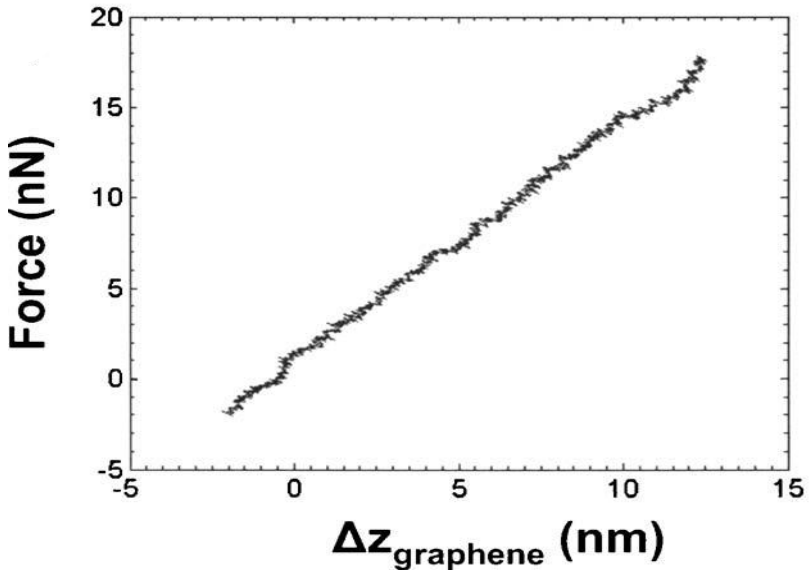

Fig 2.8 Load-displacement curve of the suspended sheet [42].

These high Young's modulus and high intrinsic strength of graphene made them a strong candidate for use as a reinforcement in many materials, to make advanced composites [44,45]. The stress transfer in graphene reinforced polymer composite can be well-traced and monitored by advanced Raman spectroscopy, by monitoring the Raman band shifts which are related to the stress transferring [45].

A study on graphene/polyvinyl alcohol (PVA) composites reported a 150% improvement in the tensile strength and a nearly 10 times increase of Young's modulus (compared with neat PVA) at a graphene loading of 1.8 vol% [46]. Other studies compared the mechanical properties of 3 epoxy-based composites containing graphene platelets, single-walled CNTs and multi-walled CNTs. Compared with pure

epoxy, the epoxy-graphene showed a 31% increase in Young's Modulus, while in the case of CNTs the increase was only 3% [46]. This superiority of graphene platelets over CNTs in terms of mechanical properties was attributed to the high specific surface area, enhanced nanofiller−matrix adhesion/interlocking, and the two-dimensional geometry of graphene platelets.

2.4.3 Optical properties of graphene

Graphene is the first experimentally available 2D chiral material. However, the origin of the optical properties lies in the 2D nature and gapless electronic spectrum of graphene, and does not directly relate to the chirality [47]. Despite being only one atom thick, graphene is found to absorb a significant amount of incident white light (2.3%), Fig 2.9, as a consequence of its unique electronic structure. It has been discussed, the opacity increases with the thickness, and each graphene layer adds another 2.3% absorption [47].

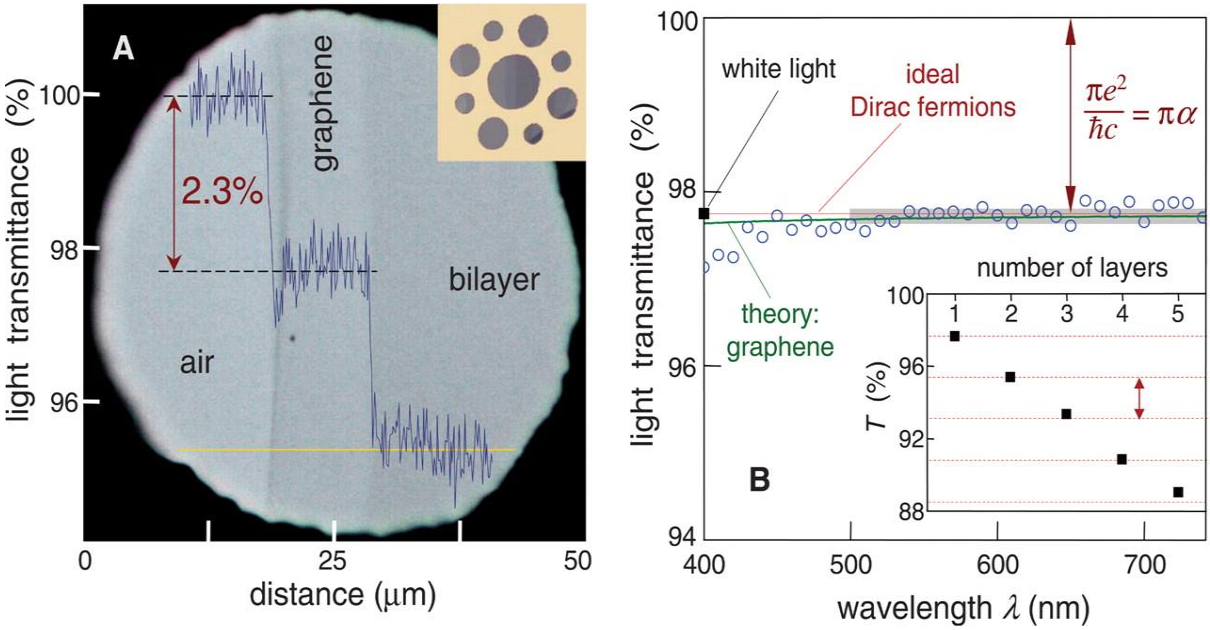

Fig 2.9 The optical properties of graphene. (a) Photograph of single and bilayer graphene suspended on a 50 μm device and (b) Light transmittance- distance curve also shown in image [47].

2.4.4 Thermal properties of graphene

Thermal conductivity of any material is a very important feature as it defines the structural capability and thus the applications. Carbon allotropes and their derivatives occupy a unique place in terms of their ability to conduct heat. The room temperature thermal conductivity of carbon materials shows an extraordinary large range from the lowest in amorphous carbon to the highest in low dimensional carbon materials [48]. Thermal conductivity (K) measurements can be divided into two types: the steady state [49], and the transient state [50].

In transient state measurements, the thermal gradient is recorded as a function of time, enabling fast measurements of the thermal diffusivity (DT) over large T ranges. Cp and mass density (ρm) have to be determined independently to calculate the thermal conductivity from the following equation [51]:

$$K = DTC_P\rho_m \qquad (2.1)$$

where K is the thermal conductivity, T the temperature, Cp specific capacity, D thermal diffusivity, and ρ is the density.

Although many methods rely on electrical means for supplying heating power and measuring T, there are other techniques where the power is provided by light. In steady-state methods, T is measured by thermocouples. The thermal properties of graphene were first measured by an optothermal Raman technique [2]. In this method, the heating power ΔP was provided by a laser light focused on a suspended graphene layer connected to heat sinks at its ends, as shown in Fig 2.10.

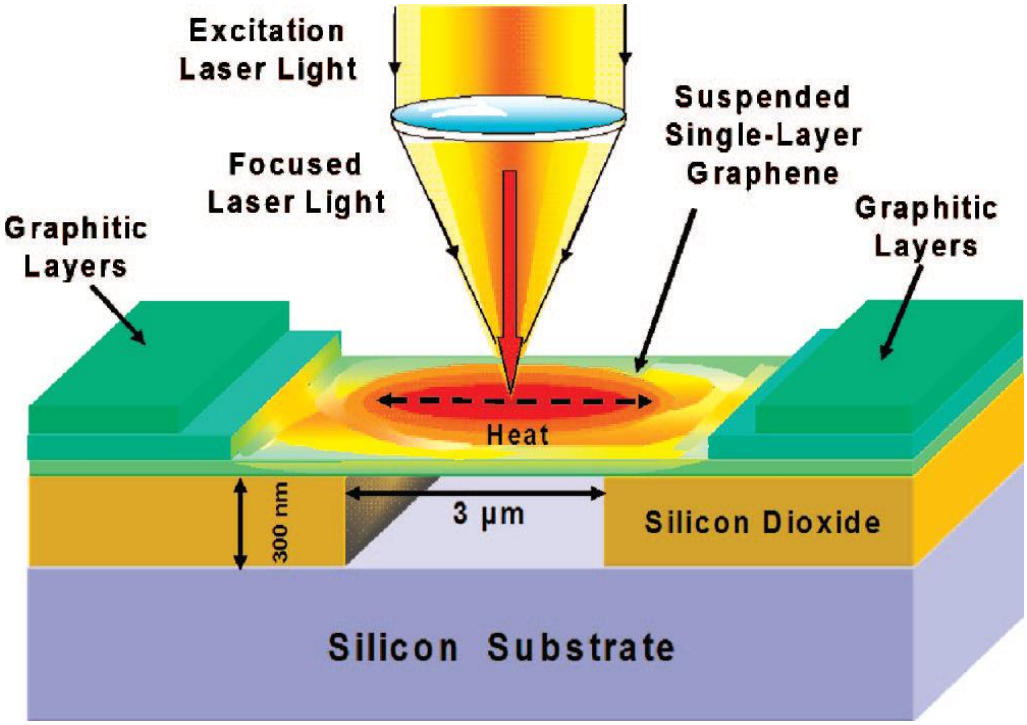

Fig 2.10 Schematic of the Raman optothermal measurement showing the excitation laser light focused on a graphene layer suspended across a trench. The focused laser light creates a local hot spot and generates a heat wave inside SLG propagating toward heat sinks [2].

During the measurements, the suspended graphene layer was heated by increasing the laser power. The G peak in the Raman spectrum of graphene exhibits a strong T dependence, thus allowing for converting a Raman spectrometer into an 'optical thermometer'. Following equation was used to obtain thermal conductivity, K, of graphene:

$$K = \chi_G \left(\frac{L}{2hW}\right)\left(\frac{\partial w}{\partial P}\right)^{-1} \qquad (2.2)$$

Using this method, a maximum value of 5300 W/mK was obtained as the thermal conductivity of the suspended single layer graphene at room temperature [2]. This extraordinary heat conduction of graphene extends its range of applications, as

promising thermal management materials in optoelectronics, photonics, and bioengineering devices, or as heating elements for industrial blast furnaces [8].

The thermal expansion coefficient of graphene was measured to be *ca*. -6×10^{-6} /K which is 5 – 10 times larger than that of ordinary graphite [52]. Negative thermal expansion is a rare case in which the material contracts upon heating rather than expanding as most materials behave. This large negative thermal expansion coefficient, which is a direct consequence of the two-dimensionality of graphene originating from the abundant out-of-plane phonons, and could play an significant role in the management of thermal stress in graphene-based devices [52].

2.5 Graphene modification

The modification of graphene with various materials has been considered as the main strategy towards tailoring the functionalities and expanding its applications [16]. Chemical modification can lead to entirely new physical properties for graphene. Depending on the nature of chemical dopants and on how they are introduced into the graphene lattice, such as adsorption, substitution, or intercalation, the results vary. Significant efforts have focused on covalently functionalizing graphene to achieve band gap tuning and modulation. In contrast to the non-covalent functionalization, the covalent schemes are more robust, imposing strong changes to the electronic properties due to the disruption of the crystallographic lattice [13]. the exploration of applications in catalysis and energy has become a hot research subject [2].

Simple N-doping is one of the interesting approaches to functionalise graphene, and can lead to the n-type transistor behaviour [11,53]. N-doping methods include NH_3 + H_2 plasma [54], electrochemistry modification [55], chemical N-doping [56], and electrothermal

doping [53]. High power electrical annealing [57] and e-annealing in NH_3 atmosphere have also been used successfully to dope graphene and the n-type behaviour has been achieved, as expected. It is believed that the annealing process preferably introduced the N dopant at the edges and defect sites [53].

Another very promising application of the functionalised graphene is in the renewable energy field. The N-doped graphene has been documented as a successful metal-free catalyst for oxygen reduction reaction (ORR) in PEM fuel cell [58]. In contrast to the two steps two electrons process for pure graphene, the N-doped sample showed a one-step four electrons mechanism for the ORR, as detailed in Fig 2.11. N-doped graphene also showed less sensitivity to the CO than traditional Pt/C electrocatalyst which is poisoned quickly under CO effect **[58].**

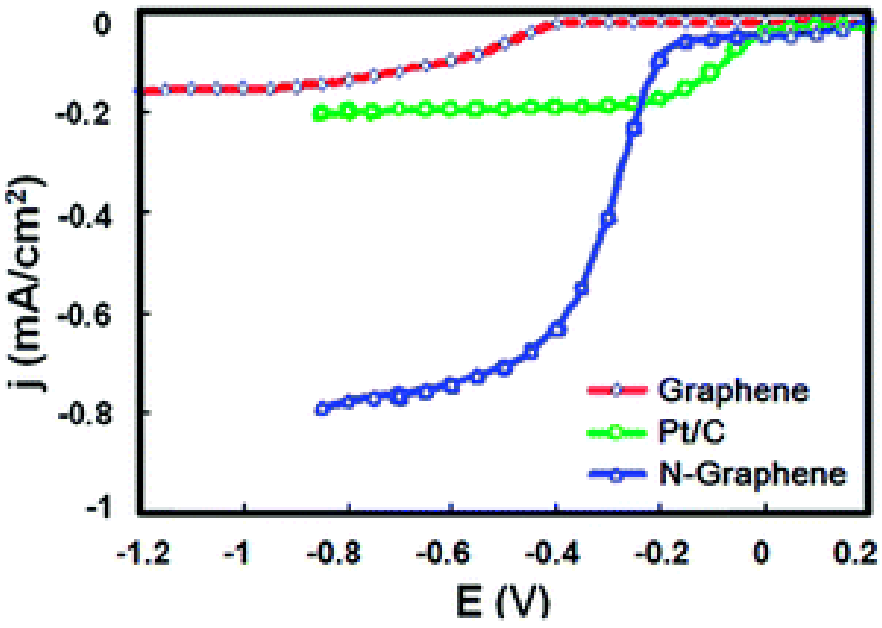

Fig 2.11 (a) LSV curve of various electrodes in air-saturated 0.1 M KOH electrolyte and (b) Chronoamprometry response of the electrodes [58].

Co-doping with two or three hetero atoms is becoming another new topic in graphene-doping research [59,60]. It has been shown that co-doping with two elements, one with higher and one with lower electronegativity than that of C (c = 2.55), for example, B (c = 2.04) and N (c = 3.04), can result in a unique electronic structure with a synergistic coupling effect between heteroatoms. It has been discussed that co-doping makes such dual-doped graphene much more catalytically active than singly doped graphene catalysts. B- and N-co-doped graphene was prepared by a two-step doping method, and was tested as catalyst for ORR. The new catalyst showed higher activity in the ORR and better selectivity for the four-electron ORR pathway in an alkaline medium, than that observed for singly B- or N-doped graphene [59-61].

Oxygen functionalization has also been discussed in the literature and there are many ongoing works on functionalising GO [62]. In addition to the effects of the oxygen functional group on the property of the base materials, the chemistry and structure of GO make it very appropriate templates for creating a wide range of materials and composites. It is covalently bonded to oxygen-containing functional groups either on the basal plane or at the edges, so that it contains a mixture of sp^2- and sp^3-hybridized carbon atoms [46].

Compared with graphene, GO showed some advantages over graphene including the improved water solubility, whereas after the oxygen functionality groups being removed, the resulting graphene sheets cannot be dispersed in water, instead they aggregate and eventually precipitate [34].

Finally, it is worth noting that the chemistry of graphene remains largely unexplored and indeed it is less developed than its physics, thus more works are required in this field. For example, the functionalization and optimised modifications of graphene could lead to solutions for a number of challenging problems associated with graphene, such as the solubility and the band gap problems [11].

2.6 Few layer graphene and graphene foam

Although single layer graphene has showed extraordinary properties, for specific macroscopic applications multilayer graphene is more preferable in some areas [30]. A bilayer graphene consists of two graphene sheets which bonded together via the weak Van der Waals force, and the electronic states become quite different from those in monolayer graphene due to strong interlayer interactions [39]. It has been shown that by increasing the number of layers, the properties of graphene differ significantly from those of single layer ones [48].

Three dimensional graphene or the so-called graphene foam (GF) has also been prepared by a temple-assisted CVD method using Ni and CH_4 as the template and carbon source, respectively [63]. The free-standing GF is extremely light and flexible, consisting of an interconnected graphene network. To obtain GFs, before etching away the Ni skeleton by a hot HCl (or $FeCl_3$) solution, a thin layer of poly-methyl methacrylate (PMMA) was deposited on the surface of the GFs, as a support to prevent from their collapsing during the etching. After the PMMA layer was carefully removed by hot acetone, the GF, a monolith of a continuous and interconnected graphene 3D network was obtained, normally accompanied with a small shrinkage in overall dimension. The GF copies and inherits the interconnected 3D scaffold structure

of the Ni template, and the graphene sheets appear to be in direct contact with each other [63].

2.7 Applications of graphene

The unique and excellent mechanical properties, rich electronic and thermal properties of graphene have motivated intense research virtually across all disciplines. Graphene has shown very promising uses for high frequency electronics [64], advanced sensors [65], transparent electronics [23], low-power switches [66], solar cells [67], and energy storage applications[15,68] . Here we focus on the main applications of graphene in the electronic industries and in the energy storage field.

2.7.1 Graphene in electronic devices

The high flexibility, atomic thickness, and unusual electronic properties of graphene have attracted extensive researches to develop new electronic devices in an effort to overcome the difficulties with traditional materials, such as the main limitations of traditional radio frequency electronics in terms of maximum frequency, linearity, and power dissipation [15].

The higher mobility of graphene allows higher operating frequencies for frequency doubling in high efficiency operations and mixer applications than existing materials [17,67]. Graphene is an ideal material for flexible electronics [23]. Furthermore, the 2D geometry, in combination with the excellent chemical and thermal stability of graphene makes the fabrication of graphene circuits fully compatible with and merged into silicon technology, which is the main material of the semiconductor industry. Field effect

transistors and transparent conductive films based on graphene have already been fabricated [15,68].

Andre Geim et al. have succeeded in fabricating a field-effect transistor (FET) made of graphene on a Si/SiO_2 substrate [39]. Graphene can be used in touch screens too, as it meets the electrical and optical requirements for transparent conductive electrodes. It also benefits from the advantage of high flexibility and robustness, which make it superior to indium titanium oxide (ITO) in some aspects [39]. Spectroelectrochemical studies on graphene based electrodes in a comparison between ITO and graphene-based optically transparent electrodes (G-OTEs), showed that while the ITO transmittance drops significantly at about 375 nm, the G-OTEs have a broad optical transparency, Fig 2.12, suggesting that the latter is highly suitable for spectroelectrochemical purposes over the entire UV–Vis region [69].

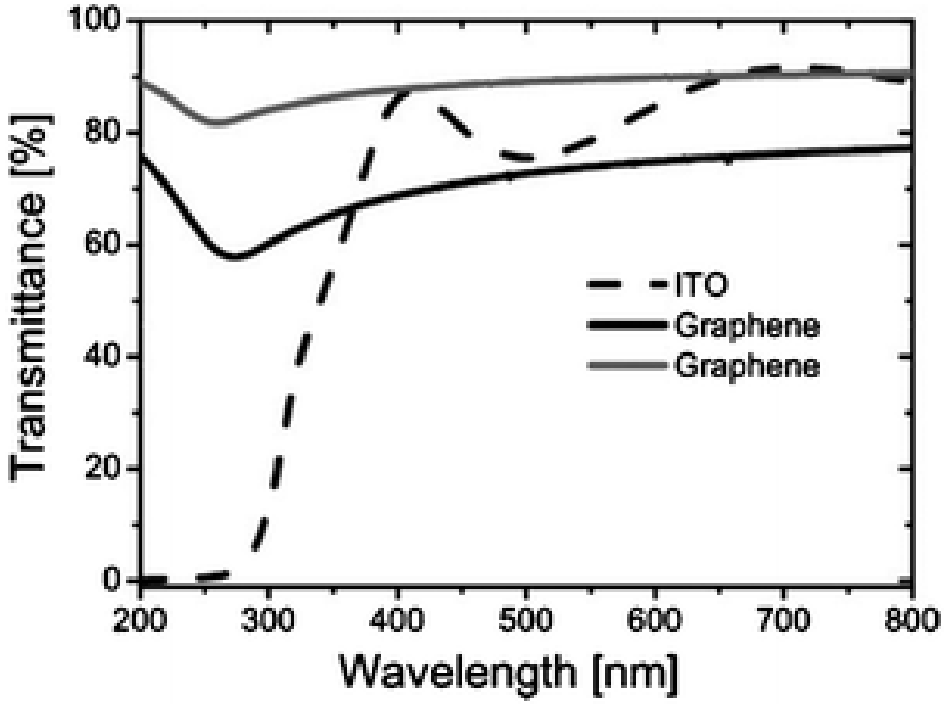

Fig 2.12 Transmission spectra of G-OTE and ITO on quarts (24 nm thick, solid black line and 8 nm, solid grey line) [69].

2.7.2 Graphene in energy storage

The extraordinary mechanical strength, very high surface areas, high flexibility, and excellent conductivity make graphene very promising for energy storage uses. Graphene can be used as the electrode materials [70], current collectors [71], scaffold [55], and reinforcement in this area [29,72]. In this section, we first discuss in detail the mechanism of energy storage in the electrochemical devices, then we will focus on the graphene based materials and summarise why they are considered suitable for uses as electroactive materials.

2.7.2.1 Electrochemical energy storage

Electrochemical energy storage systems (EESSs), e.g. batteries and supercapacitors, store electricity electrochemically via a charge-discharge process associated with chemical reactions that take place in the anode or cathode. The performance of an electrochemical system is evaluated by three parameters: power capability, cycle life and energy density. The electrode kinetics and mass transport are the key to the performance of electrochemical devices, because an improved kinetics can: (a) directly enhance the power capability [72], (b) improve the system's reversibility and thus the cycle life [73], and (c) improve the material utilisation and hence the energy density [74]. Reducing the electron transport length and the ion diffusion distance during charge-discharge processes is an effective strategy to improve the efficiency of the system [73-75].

2.7.2.2 Conventional architecture of energy storage electrodes

Energy storage electrodes traditionally have a 2D plane structure with a layer of redox active material attached to a planar current collector. This structure suffers from a trade-off between the energy and power densities on a given apparent area of the current collector. This is because the kinetics of thicker films of the redox active material becomes poor, leading to a low power capability.

Fig 2.14 shows a Ragone plot of various EESSs. As shown, batteries sit in the far right of the plot and capacitors stand on the far left. This different is related directly to their energy storage modes and electrode architectures. In battery, both the surface and the bulk of electroactive materials are involved in the energy storage process, thus the thickness does play a big role in the energy density and power density of the system. In capacitors, the charge storage process occurs only on the surface via charge separations, so naturally they have very high power density, i.e. very quick charge-discharge cycles.

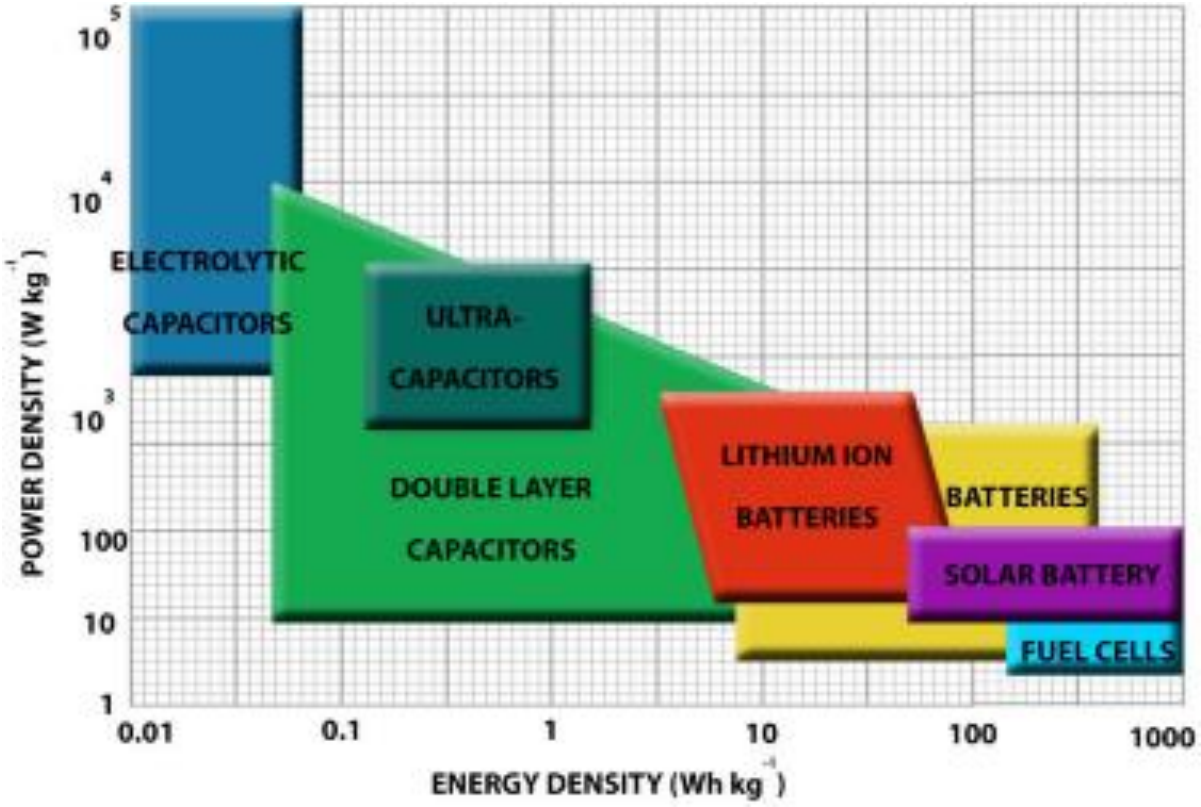

Fig 2.13 Ragone plot of various electrochemical energy storage devices [76].

One of the very interesting EESSs is the ultra-capacitor or supercapacitor which stands in the middle of the Ragone plot, expressing the compromise between the two edges. Obviously, this plot and performance is not optimum. Nature demands system with battery-like energy density and capacitor-like power density. The gap between the two systems could be bridged, if we could design a very efficient electrode architecture [77]. One proposed architecture to achieve this, is 3D design.

2.7.2.3 3D design vs. 2D

In an efficient 3D architecture, electrodes or devices, the materials do not suffer from the high trade-off between the power and the energy as they do in a traditional plane 2D electrode, since the third dimension allows for storing more energy without the

need of increasing the thickness of electroactive materials, thus the specific power is less compromised. The next advantage of a 3D design is that it naturally does not need a binder. Conventionally, a considerable amount of conductive fillers and binders have to be used during electrode preparation. The electrode materials have to be sufficiently thin to achieve good electrode kinetics. Therefore, in a 2D electrode, this inherited disadvantage limited the energy and power densities on a given footprint area. By combining a thin coating of redox active material with self-supported 3D current collectors in a 3D design, not only the conductive fillers and organic binders are eliminated, but also the energy and power performances are significantly improved [77-79].

2.7.3.3Ideal 3D electrode structures

3D structures have been extensively reported as the next generation electrodes for electrochemical energy storage. 3D electrodes have been reported for battery [78], supercapacitor [80], fuel cell [81], and solar cell applications [82], and to date very good results have been reported. However, not all of them satisfy the criteria of an ideal 3D structure. In the next section two important types of ideal structure will be discussed.

Fig 2.14 shows a schematic of an ideal core-shell 3D electrode structure, in which the red and black double headed arrows are used to depict the electron transport and solid-state ion diffusion lengths of different redox sites, respectively.

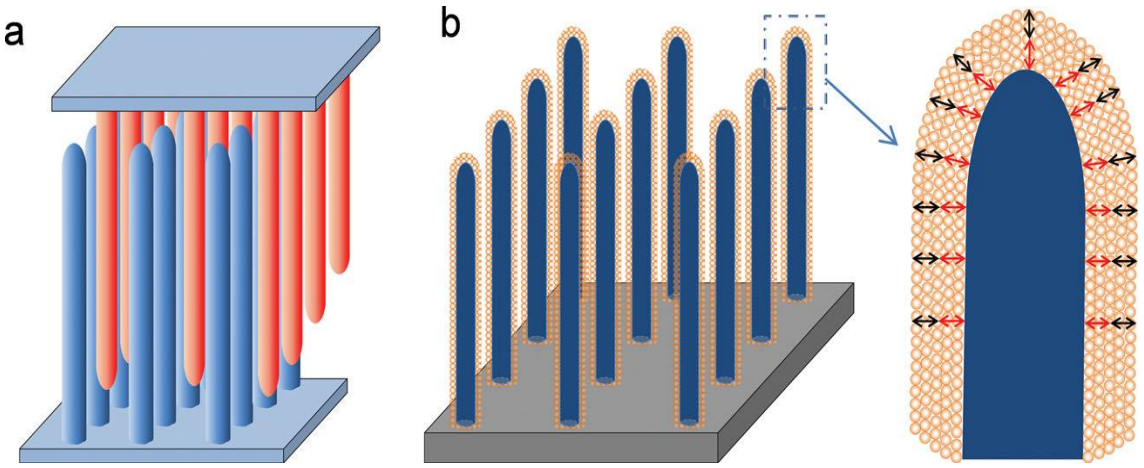

Fig 2.14 Schematic of an ideal 3D electrode structure [83].

An ideal 3D electrode requires the redox active material to be a thin coating on a 3D current collector. Due to the presence of this 3D current collector, the electrons of any redox site only need to reach the conducting core. In addition, the nano/microscale current collector is beneficial for a uniform current distribution and hence reduces the mechanical stresses during repeated charge-discharge processes [79].

Another important feature of an ideal 3D structure is that the electrode as a whole is continuous and porous, so no added binder is needed. Thus, the space within the electrode can accommodate the large volume changes during the charge-discharge. Therefore, an ideal 3D electrode not only has a high energy capacity per unit footprint area, but also offers improved power performance and a longer cycle life.

Apart from the above vertically aligned core-shell pillars, various other structures can be considered ideal as long as they possess these key structural features.

2.7.3.3.1 Monolithic and self-supported architectural carbon

Unlike the conventional powdered carbon materials, carbon monoliths are porous, self-supported, and do not require any binder or conductive agent (e.g. carbon black)

during electrode preparation [84]. Elimination of binders could significantly reduce the polarization by lowering the electrical and mass transport resistance. Further, handling carbon monolith is much easier than conventional porous carbons, such as activated carbon, CNTs and ordered mesoporous carbon [84,85]. Different methods have been used to prepare monolithic carbon [86-89], including selective etching of carbide [90], nano-casting with silica template [91], and mould conforming [92].

Low dimensional carbon materials including CNTs and graphene are at the forefront of energy storage research due to their unique structures and high surface areas. The theoretical maximum surface area is 1315 and 2600 m^2 g^{-1} for CNT and graphene, respectively [93]. However, in practical applications, their surface areas are largely reduced due to agglomeration and the use of polymeric binders. As a result, the double layer capacitances of both CNTs and graphene are far below the theoretical maximum values.

Recent researches have shown that self-supported carbon architectures can be synthesised with low dimensional nano-carbon as the building block. These spongy-like structures are continuous and porous, resembling that of a monolithic carbon. Furthermore, they preserve the desirable properties of their building blocks. A typical example is the GF prepared by CVD method with Ni foam template [94]. The as-prepared GF is highly flexible and mechanically stable. Similar methods have been used to prepare self-supported graphene-CNT foam architectures [95,96]. These electrodes have revealed a mass specific capacitance as high as 387 F g^{-1}, with a capacitance retention of 99.34% after 85000 charge-discharge cycles [54,55]. Using graphene or CNTs as the building block, other groups have also prepared similar

interconnected architectural carbon electrodes with high electrochemical performances by freeze-drying and hydrothermal methods [97,98].

2.7.3.3.2 Composite electrodes prepared by template-assisted methods

Monolithic and self-supported architectural carbon stores electrical charges by the double layer process. Their unique structures provide excellent power and cycle performances, but suffer from low energy density performance. To combat this, the incorporation of a thin layer of redox-active materials to make a composite electrode is a logical solution. The composite possesses the structural merits of the interconnected carbon framework, and the thin coating of redox active material enhances the energy capacity. Compared with metal foam current collector, porous carbons not only have a higher specific surface area, but also offer additional advantages such as low density and a wide electrochemical potential window. A common method to prepare this type of composite is electrochemical deposition which takes place at the interface between the 3D current collector and the electrolyte [99,100].

This heterogeneous reaction is highly beneficial for preparing thin and uniform coatings of redox-active materials. In a typical example, a porous 3D Ni foam was prepared with an opal template. The Ni was further used as a 3D current collector for the electrodeposition of NiOOH and MnO_2, and the performance is shown in Fig 2.15. The composite as a whole is self-supported, uniform and porous, featuring an ideal 3D electrode. Electrochemical tests unveil its high capacity retention at ultrafast charge-discharge rates or charge rates (C-rates) up to 1000C and 400C for NiOOH and lithiated MnO_2 on porous Ni. These ultrafast C-rates suggest a very high power and rapid recharge feature [100]. These results have demonstrated that both the power and energy density can be notably improved in the ideal 3D structured electrodes.

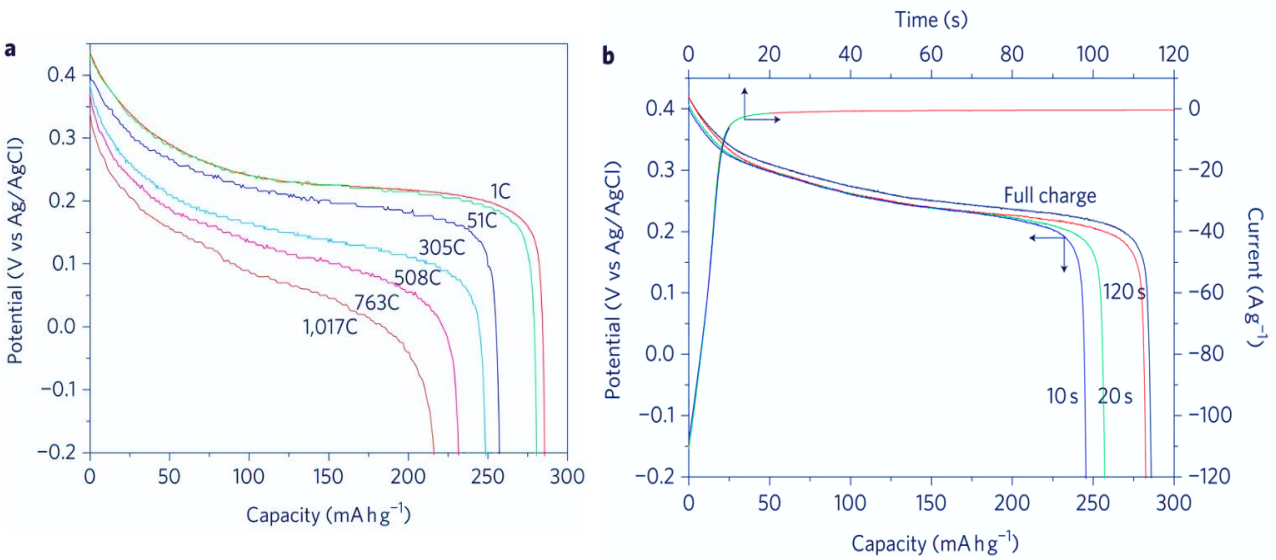

Fig 2.15 Charge-discharge performance of bicontinuous NiOOH/Ni electrodes. (a) Discharge curves of NiOOH/Ni cathode at various C-rates. (b) Constant potential charge curves (0.45 V) and 6C discharge curves after charging at constant potentials for the indicated time [100].

Other methods to synthesize a thin coating of redox active material on a porous template include magnetron sputtering [101], solution casting [102], chemical vapour deposition [102], and hydrothermal method [103].

2.7.3.3.3 Composites prepared by template-free methods

The template-assisted approach yields well-defined 3D structures controlled by the template and synthesis conditions. However, the synthesis processes are normally tedious and expensive, hence posing difficulties for commercial production. Some recent studies have successfully developed temple-free syntheses of ideal 3D electrodes.

Conducting polymers (CPs) such as polyaniline PANI [104], polypyrrole (PPY), polythiophene (PTh) and polyethylene dioxythiophene (PEDOT) are a group of commonly used redox active materials in the template-free synthesis of 3D electrodes

[105,106]. Their corresponding monomers are dissolved in a solution that also contains dispersed anionic CNTs or graphene. By passing a DC current, the monomers are oxidized and deposit at the anode as a polymer, while the anionic CNTs or graphene move towards the anode under the electric field. This one-step co-deposition method combines the electropolymerisation of the redox active materials with the electrophoresis of the low dimensional carbon building blocks. After the co-deposition, a conducting scaffold is constructed by the CNTs or graphene and the redox active materials form a thin coating on the conducting scaffold [107]. Another method is the in-situ chemical polymerization by adding an oxidizing agent to the aforementioned mixture solution [108]. An electro-deposited PPY-CNT composite electrode presented rectangular CV curves at scan rates as high as 500 and 1000 mV/s [108].

In addition to the research on CPs, attempts have also been made to synthesize 3D electrodes with various transition metal oxides or sulphides using the template-free techniques. For example, a NiO-graphene hierarchical structure prepared by hydrothermal synthesis displayed discharge capacities of 1098 and 615 mA h g^{-1} at current densities of 100 mA g^{-1} and 4 A g^{-1} [109]. In another study, following the hydrothermal synthesis, a post freeze drying treatment was used to preserve the porous 3D architecture of the graphene network with a coating of MoS_2 or FeO_x [110]. These resulting large scale composites exhibited high capacities of up to 1200 mA h g^{-1} at a discharge rate of 0.5C. The combined hydrothermal and freeze drying method has also been used to produce 3D NiOH-graphene and SnO-graphene porous interconnected frameworks with high capacity and cycling stability [111].

The 3D electrode prepared by the template-free methods generally has a less ordered structure compared with those prepared by the template technique. However, both the

ion diffusion and electron transport lengths are minimized, and these binder-free electrodes satisfy the criteria of an ideal 3D electrode for electrochemical energy storage applications. All of the above temple-free methods used a starting solution or dispersion containing the redox active materials and discreet CNTs or graphene as the building block. These solution based processes do not require a pre-made template, and are less tedious and suitable for scale-up production.

2.7.4 Graphene foam as electrode support

Different forms of carbon including graphene, graphite, CNTs, and their monolith composites have been the main materials for capacitor electrodes. However, pure carbon is incapable of providing the desired energies in systems, which is due to a variety of reasons, including non-faradic storage mode, low capacity, p–p stacking in few layer graphene, large inaccessible surface area of graphene, and the intrinsic microstructure of carbon. To counter all the electrochemical limitations of carbon materials, it would be highly desirable to introduce electroactive materials into a 3D carbon network.

Apart from the main advantages of the 3D structures which have been discussed earlier, the open porosity feature of a GF scaffold can also help in stabilizing the surface morphology of the redox counterpart, as the pores can function as a host to the redox elements and accommodate the strains in the entire electrode structure during cycling.

2.8 Other 2D materials

After the ground-breaking isolation of a free standing graphene, and subsequent discoveries of its extraordinary properties, 2D structures stand out as a new class of

valuable materials and have promoted extensive studies worldwide. Other layer materials such as h-BN [109], MoS_2 [111], $NbSe_2$ [111], complex oxides [113], and transition metal carbides such as Ti_3AlC_2 [110], have also been successfully attempted for the production of 2D graphene analogues by adopting a similar cleavage technique. 2D silicene (a graphene analogue of Si) with both α and β phases was also prepared by an epitaxial growth of Si on Ag and Ir surfaces [112]. Theoretical studies and physical calculation predict the discovery of many other new 2D materials including SiC [112-118].

Due to the importance of SiC and its wide applications in thermal and electronic fields, 2D SiC could be a very promising material. In this section, first we review the general properties of SiC and following that we will discuss the theoretical studies about 2D SiC and the main challenge towards preparing 2D SiC.

2.8.1 SiC: 3D and 2D structures

2.8.1.1 General properties of SiC

SiC is a well-known semiconducting material with outstanding properties, e.g. large band gap (Table 2.1), high electric breakdown field [119], and excellent chemical stability and chemical resistance [120]. The high thermal conductivity along with low thermal expansion and high strength give SiC the exceptional thermal shock resistant qualities [117]. As a ceramic with low grain boundary impurities, SiC maintains its strength at very high temperatures, even approaching 1600°C with little losses [118]. Light emitting diodes (LEDs) [121], field effect transistors [122], solar cells [119], engineering ceramics [120], memories [121], and UV detectors [122], are typical examples of SiC-based devices [123-127].

SiC is composed of tetrahedral structure of C and Si atoms with strong bonds in the crystal lattice. Each SiC bilayer can be oriented into only three possible positions in the lattice in order to maintain the tetrahedral bonding. The binding between Si and C atoms in SiC is predominantly covalent, with only 12% being ionic. Hundreds polytypes of SiC have been identified according to different stacking arrangements of the Si and C atoms. The most common phases are the cubic 3C (β-SiC), hexagonal 2H, 4H, 6H, and 15R (α-SiC). Table 2.1 summarised the atomic parameters of typical SiC polytypes [128-132].

Table 2.1 Atomic parameters of different SiC allotropes

Material	**Phase ratio**	**Lattice constants**	**Band gap (eV)**	**Stacking**
3C-SiC	100% Cubic	*a*: 0.436	2.4	ABCABC
2H-SiC	100% hexagonal		3.2	AB
4H-SiC	Hexagonal/ cubic:1/1	*a*:308 *c*:0.1512	3.2	ABCB
6H-SiC	1/3Hexagonal 2/3cubic	*a*:0.308 *c*:0.105	3.0	ABCACB
15-R	2/5Hexagonal/3/5 cubic			ABCACBCAB ACABCB

In addition to bulk SiC, 1D SiC nanostructures such as nanowires [133], nanowhiskers [134], and multi-walled SiC nanotube with two interlayer spacing of 0.38 nm and 0.47 nm [129], have also been documented extensively. 1D nanostructures have been prepared by a variety of methods, including sol–gel, carbothermal reduction [135], CVD, laser ablation [136], arc-discharge [137], and metal cluster-catalysed processes [138]. Compared with the bulk SiC, 1D nanostructures have many advantages, such as they have much higher elasticity and strengths. Owing to their high Young's Modulus, they have been used as reinforcements in ceramic- and polymer-matrix composites [125,129].

2.8.1.2 3D SiC

Other widely investigated SiC structure is the 3D type. Among many cellular ceramic foams, 3D SiC and its composites have attracted much attention and both open and closed cell foams have been synthesised [139,140]. The morphological and microstructural features of a foam, including the cell types and dimensions, strut sizes and void configurations can change significantly, depending on the manufacturing procedures, and they can be tuned to suit different applications. For example, ordered hierarchical structures can be achieved via the template-assisted synthesis [141] whereas the sol-gel process suits large and scalable template-free industrial level manufacturing [142]. The porosity level of the foam is yet another key parameter that can be modified by varying the synthesis routes [140], *e.g*. the replica method produces foams with a cell size in a millimetre range; whereas the sol-gel method can result in nanometre sized pores [143]. By developing new synthesis methods and producing new structural features to vary the phase ratio, porosity, density, heterojunctions etc., it is expected that new properties and thus extended applications could be explored.

Today, ultralight and flexible materials demonstrate successful applications in many areas. Graphene foams with air-like density and ultra-flyweight aerogel (1 mg cm^{-3} density or lower) have been employed successfully for a wide range of applications [55,144], and most of these foams showed near-zero Poisson's ratio. Similarly, the development of lightweight, recoverable, strong SiC structures will therefore be very beneficial for a variety of purposes where weight, size, energy consumption and eventually cost are important.

2.8.2 Possibility of 2D SiC

SiC shares many structural similarities with graphite and BN: Firstly, all of them have both hexagonal and cubic structures, and their 3D structures consist of layer-stacking sequences [145]. Secondly, their 3D networks are mainly based on in-plane covalent bonds and finally, all of them have high chemical and thermal stability for advanced applications[146]. However, there is a key structural dissimilarity between SiC, graphite and BN. In the latter two, they have intrinsic sp^2 bond in their hexagonal structures, whilst in the former sp3 bonds exist in both the hexagonal and cubic crystals [147]. This difference could eventually define if a truly 2D graphene-like structure can be produced.

So far, several calculations, including the density-functional theory (DFT) framework combined with ab-initio studies, particle-swarm optimization (PSO) technique and other studies have suggested that single layer SiC is energetically stable and reachable [148-153]. Structurally, 2D SiC is expected to have a layer layout half way between those of hexagonal planner graphene and folded silicene (0.44 Å buckling) [154,155]. Thus, 2D SiC is expected to stabilise itself through slight folding, and will most

likely be layer as a honeycomb structure, in which the C and Si bond through sp^2 hybrid orbitals to form the SiC sheet [149].

On top of the high bonding strength of the SiC, there are more than 250 polytypes for SiC with completely varied structures and features. Although some 2D structures can be easily cleaved from their bulk, it would be difficult for SiC. Bare cleavage does not work for SiC, and post-etching process is needed [156,157]. Further, existing micro pipes in the SiC make the mechanical separation rather difficult, as they reinforce the adhesion force between SiC layers [149]. Thus, even though 2D SiC is theoretically predicted, its production faces many challenges[158].

2.9 summary

This chapter presented an overall review about the synthesis, properties and applications of graphene. Specifically, the discussion focused on the following areas; We reviewed the existing approach for graphene production. Both bottom-up approaches such as CVD method and Top-down techniques e.g. micromechanical cleavage were discussed in details. It was found that different methods result in different forms of graphene, namely single layer, few layer or graphene foam, with various level of quality.

1- In the properties part, we described some of the discovered properties of graphene with particular focus on reporting the most successful measurement techniques that achieved these properties.
2- The application of graphene in energy storage field was mainly discussed. It was found that graphene is an ideal template for producing highly efficient energy storage electrodes.

3- Finally we switched to other 2D materials with focus on SiC. Apparently, separating 2D SiC from its 3D bulk is a very challenging topic and not easy to proceed as rather than sp^2 hybridised sheet, SiC layers are sp^3 hybridised.

In this research, we are aiming to prepare some 2D and 3D graphene related materials with novel properties by adopting specific synthesis procedures. Chapter 5 will cover the application of the produced graphene composite in energy storage field, and chapter 6 and 7 are dedicated to the SiC project, in which we will present our approach towards producing some new SiC structures.

Chapter 3 : Experimental methodology and synthesis

3.1 Introduction

So far extensive research have been reported on graphene-based materials. Despite from the similar synthesis routes and measurements, different results and sometimes contradict conclusions have been reported, revealing the significant impacts of details of the experiments on the quality of the product and finally its performance. Indeed, it is not the materials or the general method themselves, but the quality of the materials and the accuracy of the measurement that make such big differences.

With the aim of making this work repeatable by other researchers, this chapter details the generic fabrication and measurement techniques used in this thesis. The first section shows the synthesis methods for GFs, conductive polymers (CPs), GF composites and SiC materials. We will describe in detail the preparation condition of the fabricated materials. In the characterization section, both the structural characterization and mechanical and electrochemical properties measurement will be

presented. Sample preparation procedures for various tests will be presented at the end of described techniques. All aqueous solutions were prepared using deionized water, unless otherwise specified.

3.2 Sample preparation

3.2.1 CVD synthesis of GF

GFs were prepared using the CVD method, using Ni foam (supplied by Inco. Ltd, 1.7 mm thickness and density value of 380 g m^{-2}) and pure Styrene (Sigma Aldrich >99%) as the carbon source. The Ni template (2 × 2 cm^2) was first annealed for 10 min at 1000 °C under a controlled H_2 (150 sccm) and Ar (350 sccm) atmosphere. H_2 was used to catalyse carbon deposition onto the Ni foam template and the main role of Ar was to provide an inert atmosphere for the reaction.

After annealing the Ni foam, the pure Styrene was syringe injected into the quartz reaction tube of 100 cm in diameter, at a rate of 0.254 ml/h for 1 h. At the end of the reaction, the furnace, H_2 and styrene were turned off, and the furnace was cooled naturally down to room temperature under a slow flow of Ar (10 sccm). Following the cooling step, the Ni substrate was thoroughly etched overnight in 3 M HCl (Fisher chemical, 37%) at 80 ºC, to obtain free-standing GFs.

For synthesizing GFs with higher density (ρ = 6 - 8 mg cm^{-3}), a Ni foam with higher density (1100 g m^{-2}, Inco. Ltd) was used for the CVD synthesis.

3.2.2 CVD synthesis of 2D graphene

2D graphene was synthesized using the CVD method on a Cu foil (99.8% pure, 0.025 mm thick, Alfa Aesar) substrate. Firstly, the Cu foil (4 cm^2) was loaded into the furnace and heated up to 1000 ºC under Ar (200 sccm) and H_2 (100 sccm). After annealing at 1000 ºC for 10 min, the Ar gas was turned off and Styrene was injected into the system with a flow rate of 6.61 ml/h, under continuous flow of H_2 (100 sccm). Following 40 min deposition, the styrene and the furnace were turned off, and the system was cooled under a slow flow of H_2 (50 sccm) and Ar (50 sccm). After etching the Cu away by 80 °C HCl (3 M), the resulting graphene was transferred onto a Si substrate for structural characterization. The synthesized graphene film was very thin, and as we deliberately eliminated the PMMA coating during the transfer stage to avoid any impurity[159,160] most of the graphene was wasted in the acid solution and only a small amount (*ca*. 30 - 40%) survived the etching and transferring processes.

3.2.3 Chemical and electrochemical synthesis of conductive polymer-GF composites

PPY-GF composites were prepared by both chemical and electrochemical deposition. For the PPY-GF preparation, GFs were first immersed in a 0.1 M Pyrrole (Alfa Aesar 98%) solution containing methanol (Fisher Chemical > 99.5%)/water (50:50 vol %), and then $FeCl_3$ (Sigma-Aldrich 97%) was added as an oxidant (The volume ratio of Pyrrole solution to $FeCl_3$ oxidant was 1 : 2). Subsequently, the resulting solution and the impregnated GFs were left for 15 h or 3 h for varied polymerization process. The resulting PPY-GFs were then taken out and thoroughly washed with deionised water. For comparison, both pure PPY films and PPY-GF composites were prepared electrochemically from the 0.1 M Pyrrole solution at different deposition times. For the

electrochemical synthesis of PPY-GF, Chronoamprometry technique (potential range 0 - 0.8 V) was used to deposit PPY films on the GF from 0.1 M Pyrrole/0.5 M KCl solution. PANI-GF electrodes were prepared electrochemically from 0.1 M aniline/0.5 M H_2SO_4 solution using the same Chronoamprometry technique.

3.2.4 3D SiC preparation

SiC foams were generated by a carbothermal reduction of SiO(0.3 g), (Aldrich-Sigma, UK) with the GF foam templates, at a temperature range of 1380 - 1550 °C , a dwell time of 3 h, and in an Ar (100 sccm) atmosphere. To achieve SiC foams with different densities, the GFs with different ρ values (3 - 7 mg cm^{-3}) were utilised.

To eliminate any unreacted SiO or other residuals, most of the SiC were etched in concentrated HF (58 -62%) for 3 h. During etching, the samples were stirred with a PTFE rod at hourly intervals to ensure even and thorough etching. Next, the samples were washed with 10% HCl to remove any fluorosilicate by-products. The samples were then washed several times with deionised water to remove any traces of acid, and finally dried in oven at 80 ºC to obtain the 3D SiC foams.

3.2.5 2D SiC preparation

2D SiC flakes with various thickness were separated from their 3D SiC paternal foam and 1D SiC nanowires, by a multi-step sonication process. Firstly, the SiC foams were sonicated in propanol for 10 min, then the upper solution which mainly contained 1D SiC nanowires was poured away and the rest of the solution was diluted further with propanol and sonicated again. This was repeated for 4-6 times for each sample, to obtain a dilute suspension. At the end of the sonication, the resulting 2D SiC flake-

containing solution was drop-casted onto a substrate (Si wafer or a glass slide), for later morphological and spectral characterization

3.3 Characterisation techniques

A wide range of characterisation techniques was used to study the structures of the produced materials. The morphology of the GFs, GF composites and SiC samples was investigated thoroughly by SEM, TEM (attached with an EDX) and μ-CT. Raman spectroscopy and XRD were also used for further structural characterisation. The electrochemical properties of the GF, PPY-GF, PPY, PANI and PANI-GF were studied using a three electrodes cell. The mechanical properties of the GF and SiC foams were investigated using in-situ compression tests. The next section describes sample preparation and machine specifications for each measurement.

3.3.1 Scanning electron microscopy (SEM) and energy dispersive X-ray spectroscopy (EDS)

The SEM is an instrument that creates a high magnification surface image by using electrons to form the image. A beam of electrons is produced at the top of the microscope by an electron gun[161]. Fig 3.1 displays an illustration of the SEM system. As shown, the electron beam travels through electromagnetic fields and lenses toward the sample and once it hits the sample, electrons and X-rays are ejected from the sample. The detector uses these secondary electrons, backscattered electrons, characteristics X-rays (emitted from beneath the sample surface) to produces final image [162].

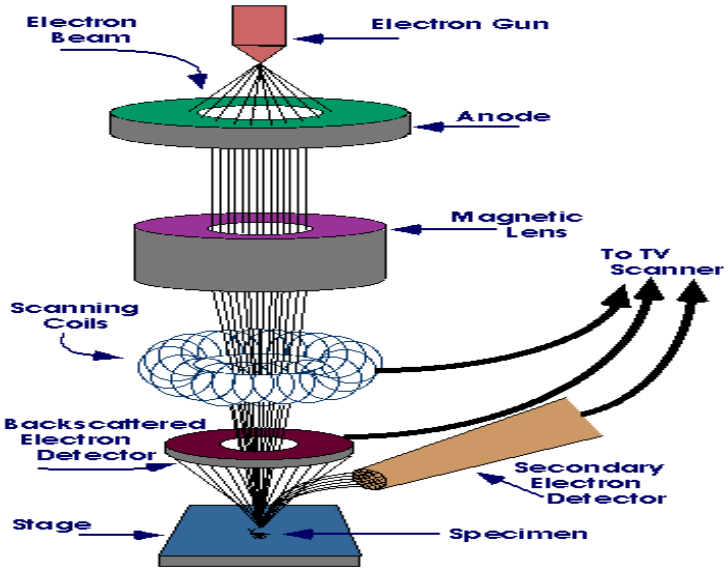

Fig 3.1 Schematic diagram of SEM [161].

To analyse the elemental composition of a material, it is always necessary to obtain an EDS spectrum of the sample. The EDS spectrum is obtained by analysing the X-ray photons produced from the electronic transition of the sample. In this project, SEM-EDS observations were performed using a Hitachi S3200N SEM-EDS machine. All samples were used directly for SEM observation without coating, as the samples are conductive or semi-conductive.

3.3.2 Micro–computed tomography (µ-CT)

Micro (µ)-CT scan is a non-destructive 3D imaging technique in which a focused X-ray source illuminates the sample mounted on a rotating stage. This technology is very useful for internal structure analysis and also for simulation studies [163]. Our µ-CT imaging analyses were recorded using an X-Tek Benchtop 160Xi CT machine. No sample preparations were needed for this test. The average area of characterised samples was 20 mm^2.

3.3.3 X-ray powder diffraction (XRD)

XRD is a powerful technique for phase identification of a crystalline material. It provides information on unit cell dimensions, crystal perfection, lattice spacing, *d*, grain size and texture. XRD is based on the constructive interference of monochromatic X-rays with a crystalline sample. These X-rays are generated by a cathode ray tube, filtered to produce monochromatic radiation, collimated to concentrate, and directed toward the sample. The interaction of the incident beam with the sample produces a constructive interference, and thus a diffracted beam when conditions satisfy Bragg's Law [164]:

$$n\lambda = 2d\ sin\theta \qquad 3.1$$

XRD patterns were recorded by a Bruker D8 Advance diffractometer working with a Cu-Kα radiation (λ = 0.154 nm) operated at 40 kV and 40 mA. Powdered samples were prepared by grinding the 3D samples into a fine powder. Approximately 1 cm^2 flat thin films were used for XRD analysis. The sample, was inserted into the diffractometer sample holder and scanned from10 - 80° 2θ with a step size of 0.02°, and 1 s step time.

3.3.4 Transmission electron microscopy (TEM) technique

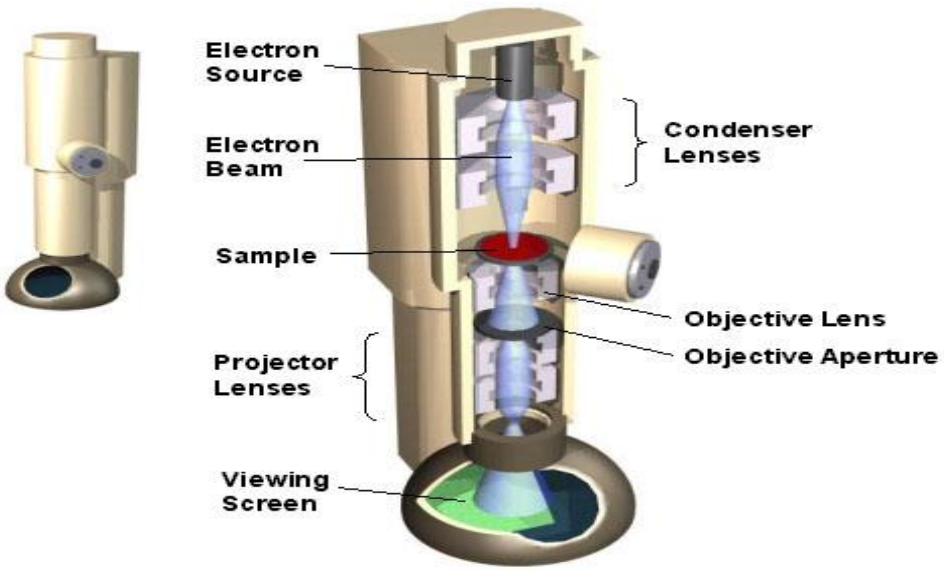

Fig 3.2 illustration of TEM system [165].

TEM is a very important microscopy technique that generates very high resolution images down to 0.2 nm scale. In contrast to the SEM in which electrons only hit the surface, the electron beam in TEM travels through the entire sample and thus can provide much more valuable information about the internal structure of the material. The crystal structure of samples can also be analysed via electron diffraction. Elemental mapping, STEM bright field (BF) and dark field (DF) imaging are all achievable with TEM. Fig 3.2 shows an illustration of a TEM system.

By using TEM microscopy, some researchers even observed individual adatoms (atoms that lie on a crystal surface) such as, hydrogen and carbon on graphene or the movement of the hydrocarbon chain, which is a significant development in this field [166].

In this research, the TEM investigation was carried out using a JEM 2100 TEM (STEM), operated at 200 kV. For the TEM specimen preparation, the samples were

ultrasonically dispersed in acetone (Fisher Chemical) for 30 min and then the suspension was dropped onto a holey carbon coated copper grid (300 Mesh, Agar).

3.3.5 Raman Spectroscopy

Raman scattering is a spectroscopic technique in which vibrational transitions occur during the scattering of monochromatic light (i.e. laser source) by molecules. Each molecule has a different set of vibrational energy levels, thus when a laser is focused on the molecule, the photon off the molecule can be scattered either elastically or inelastically. Fig 3.3 shows the energy level changes during a Raman scattering.

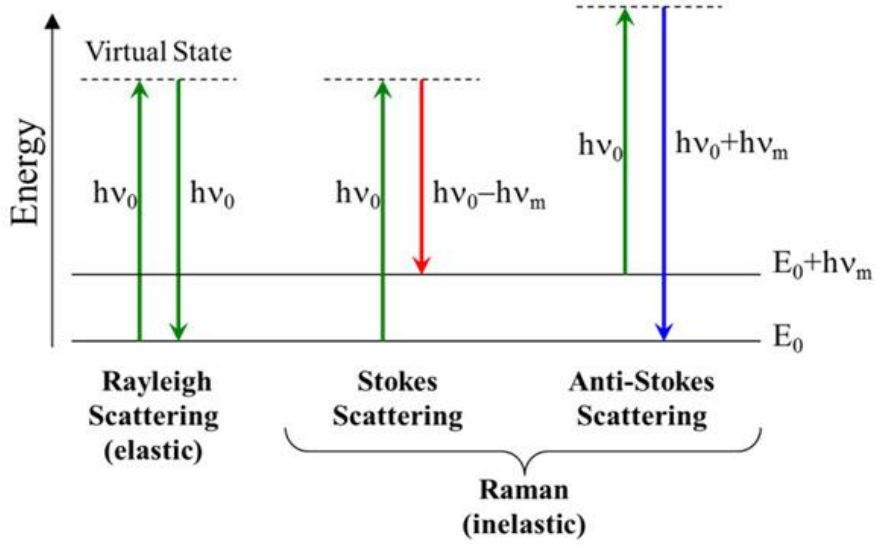

Fig 3.3 Energy transitions for elastic and inelastic Scattering [167].

The majority of the scattered light is of the same frequency as the excitation source, thus does not show any Raman effect (Rayleigh). A very small amount of the scattered light (only 1 in every 30 million photons) is inelastically scattered. Stokes and anti-

stokes scattering occur when the photon emitted have higher and lower energy and frequency than those of observed photons, as shown in Fig 3.3. Since the molecule prefers to be in the ground state rather than the excited state, the anti-Stokes scatter is unlikely at room temperature.

Apart from its wide application for materials characterisation, Raman spectroscopy has become an essential part of graphene characterisation, as it distinguishes single layer graphene from bilayer and few layer graphene.

In this thesis, the Raman spectra were recorded using a Renishaw inVia Raman microscope. The excitation laser beam at a wavelength of 532 nm was focused by a 50 × objective onto a small area of the sample. For 3D material measurements, the Raman samples were prepared by grinding their foams into fine powder. The 2D samples were prepared by dropping their dilute propanol suspension onto a glass slide or SiO_2/Si wafer.

3.3.6 Atomic force microscopy (AFM) technique

AFM is a type of scanning probe microscopy (SPM) that uses a cantilever with a very sharp tip to scan a sample surface, to reveal surface morphologies of a material, such as thin film thickness, height etc. Fig 3.4 shows a schematic of an AFM system. The most popular and primary AFM imaging modes are contact mode and tapping mode. In the contact mode, the tip touches the surface of the sample directly and thus there is a possibility of surface damage, but in the tapping mode the tip is only oscillated over the surface of the sample. Modern AFMs can now be used in air, liquid or vacuum to generate high-resolution topographic images of a surface at atomic resolution.

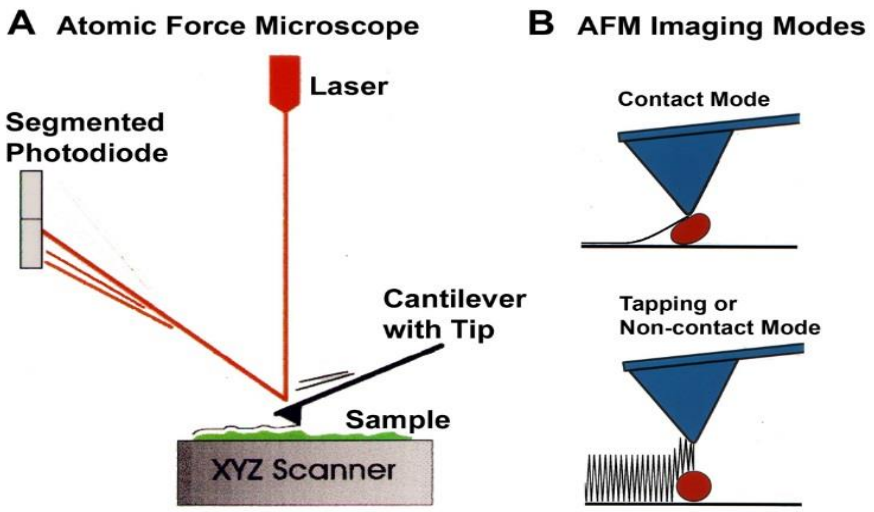

Fig 3.4 A schematic of an AFM [168] .

In this thesis, AFM images (tapping mode) were collected using a Bruker Innova machine. The AFM samples were prepared by dropping the disperse samples, SiC or graphene, on a SiO_2/Si wafer.

3.3.7 Thermogravimetric Analysis (TGA)

TGA is a thermal analytical technique that measures the weight of the sample at various temperatures during a defined heating process. In this research, TGA was performed using a TA SDT Q600 TGA-DSC instrument, at a ramping rate of 10 ºC/min under air environment. We also used TGA to investigate the weight ratio between GF and conductive polymer. By identifying the weight loss differences between PPY, GF and the composite, one can easily find the PPY content in the composite as PPY burns up completely at around 425 °C and the major weigh loss of graphene occurs after 600 °C.

3.4 Mechanical properties measurement

The mechanical properties of the GF foams and SiC foams were studied by conducting a compressive test under in-situ SEM imaging. This tests were carried out at Imperial College London, Department of Materials.

Characterised samples have an average size of 10 x 10 x 2 mm^3 (length, width, and thickness, respectively). Compression tests were carried out in-situ inside a HITACHI S-3400N SEM using a DEBEN microtest with a 300N single leadscrew tensile module. Tests were performed in position controlled mode at 0.001 - 0.6 mm/s to record the morphological changes and elastic recovery of the structures.

The effect of the pressing on the mechanical properties of the GF was also investigated by performing compression test. The test samples were prepared by placing the GF between two Ni foils, and the entire assembly was pressed under a pressure of 5 MPa. The size of the specimens were 5 x 2 mm^2, length x width respectively, and the average thickness was 1.7 mm. The length of the gauge was 2.3 mm. The rate of the extension was 0.1 mm/min. Fig 3.5 shows a photograph of the GF during test.

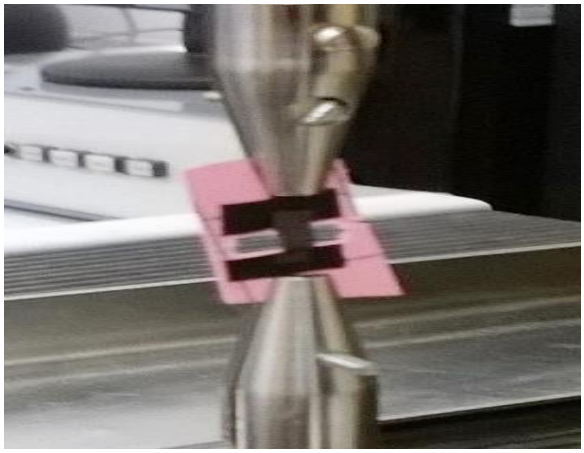

Fig 3.5 A photograph of the GF during mechanical test.

3.5 Electrical conductivity measurement

The resistivity, and therefore the conductivity of a sample can be determined by applying a voltage to the sample and subsequently measuring the resulting flow of current, then calculating the resistance and finally the resistivity using the length-area information. In this research, the electrical conductivity of the graphene foam was tested using the two-probe method which involves imbedding copper wires in the GFs and then securing them with silver paste. This enabled a strong electrical contact and therefore a small contact resistance between the GF and the wires. In this research, silver-loaded epoxy was used to secure samples to the copper laminate, as well as to provide a conductive contact between the wires and the GF specimens under analysis.

3.6 Electrochemical characterisations

The electrochemical properties of the GF foams, conductive polymer and conductive polymer-GF composites were investigated by using a variety of electrochemical techniques such as cyclic voltammetry, linear sweep voltammetry, A.C impedance,

Chronoamprometry, Chronopotentiometry and other tests. Electrochemical tests were carried out using a CHI 660C Electrochemical Workstation and a three electrode cell: Pt wire as the auxiliary electrode, Ag/Ag Cl as the reference electrode and gold (and glassy carbon) as the working electrode (2 mm diameter), in a 0.5 M KCl (Sigma-Aldrich 99-100 %) electrolyte. The Impedance measurements were recorded in a frequency range of 100 kHz - 0.1 Hz at OCP with a voltage amplitude of 0.005 V. Fig 3.6 shows a photograph of the electrochemical device used for the electrochemical characterisations.

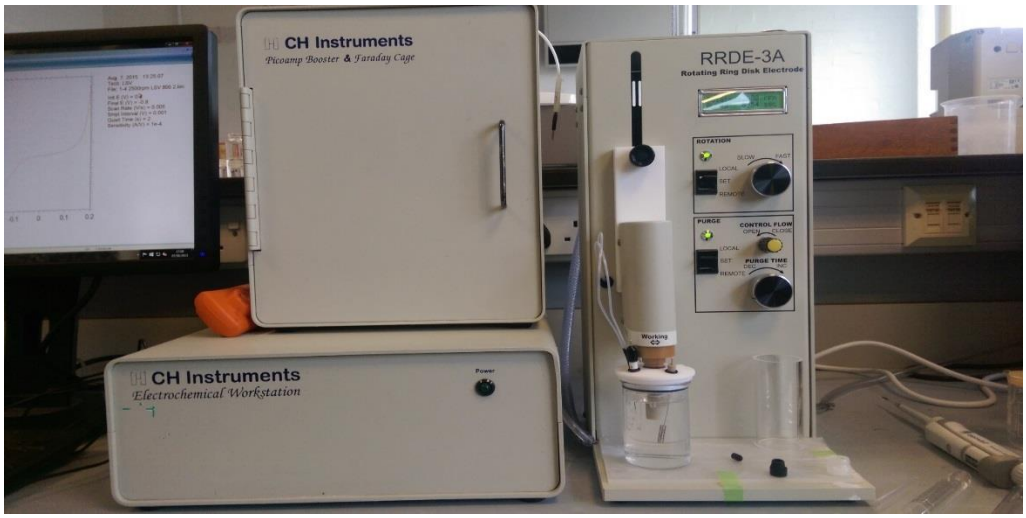

Fig 3.6 A photograph of the electrochemical device.

3.7 Electrode preparation

All electrodes were used directly as working electrodes without adding a binder or any carbon conductive, unless otherwise specified. The GF foams and 3D GF composites were mounted on the working electrode using a Teflon holder, and the assembly is

shown in Fig 3.7. The working electrode was cleaned by polishing with 1 μm alumina paste or diamond paste, before every assembling.

Fig 3.7 Mounting GF on a working electrode by using a Teflon holder.

Chapter 4 Graphene synthesis and characterization

4.1 Introduction

Large scale CVD synthesis of graphene on Ni and Cu templates has emerged as the most promising approach for the industrial use of graphene [32,169]. Both mono- and multilayer graphene can be produced via the CVD approach by using a Cu or Ni template. Apart from the template effect, the synthesis conditions and parameters such as carbon sources [170], H_2 flow rate[171], and the physical properties of the template such as the porosity level [172], as well as the cooling rate [23], affect significantly the general structure, thus applications, of the produced graphene.

Single layer 2D graphene shows excellent mechanical and thermal properties, and it has been used to reinforce materials for structural engineering applications [44]. However, being one atom thick with no band gap, graphene is not an ideal choice for some areas, unless it can be modified to meet the desired features.

One of the modified forms of graphene is the few layer GFs. In a GF, the 3D network makes its use much easier, since its few layer structure performs as a transit between the one atom thick 2D graphene sheet and the macroscopic world of materials in electronic devices. The first reported GF[63] was grown on Ni substrate by the CVD of methane in a hydrogen atmosphere. Before this, the CVD method has been well-established for the growth of single and few layer graphene on a polycrystalline Ni or Cu template.

Most of these researches reported wrinkles formation on the graphene surface, mainly due to the difference of thermal expansion coefficients between Ni and graphene

[32,173,174]. Fig 4.1 shows SEM images of graphene grown on a Cu (Fig 4a) and Ni (Fig 4b) substrate, respectively. The graphene wrinkles, graphene flakes and the Cu grain boundaries are visible.

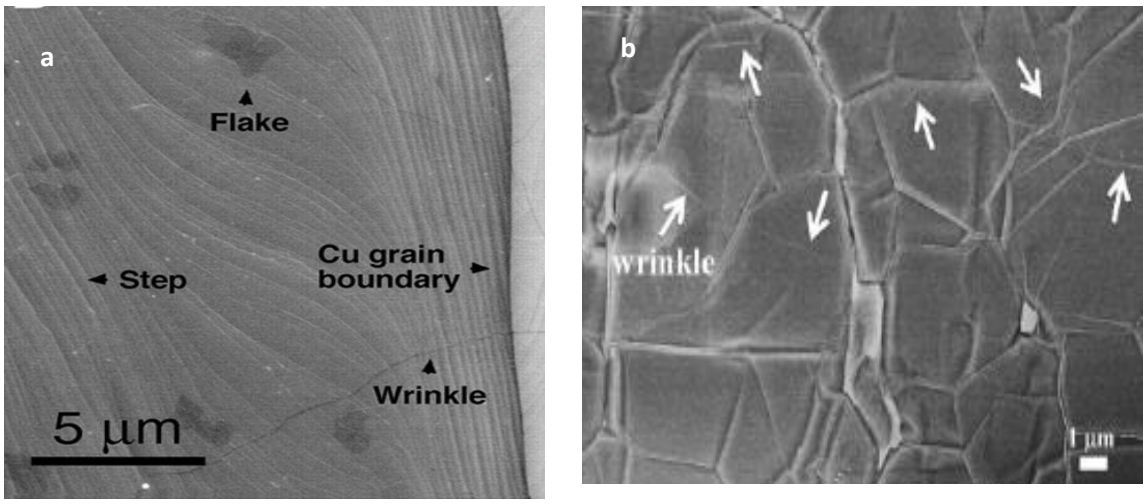

Fig 4.1 (a) High resolution SEM image [32] of graphene on Cu and (b) FESEM image of graphene on Ni substrate [173].

In this chapter we aim to synthesise both GF and graphene with minimum level of defects. The main focus will be on the 3D graphene foam, as the produced foam is the key structure for all presented materials in this thesis.

4.2 GF synthesis and characterisations

4.2.1 CVD-growth of GF

GFs were prepared using the CVD method, Ni foam as template and styrene as carbon source. The growth mechanism for graphene on Ni has been well-documented, and the key is Carbon segregation which occurs during the cooling step and is a non-equilibrium process [173-175]. It is believed that this type of non-equilibrium segregation

is the main reason behind the uncontrolled thickness of graphene and its non-homogenous growth[176,177].

Fig 4.2 illustrates the preparation procedure of GF. Firstly, the decomposed carbon atoms diffused into the Ni template which also act as the catalyst during the synthesis step. Secondly, when the Ni substrate reached the quenching stage, carbon atoms diffused out onto the surface of Ni, to form the graphene film. Thirdly, after dissolving the Ni substrate in hot HCl, a floating GF was obtained on the top surface of the etching solution.

In contrast to other similar works on graphene[33,178,179] and also GF[63], we did not use PMMA during the etching process as we found that PMMA residues cannot be completely removed afterward, thus we carried out direct etching to avoid the PMMA impurity .

Finally, after thorough washing with deionised water, the resulting GFs were then dried in an oven at 80 ºC, prior to be characterised.

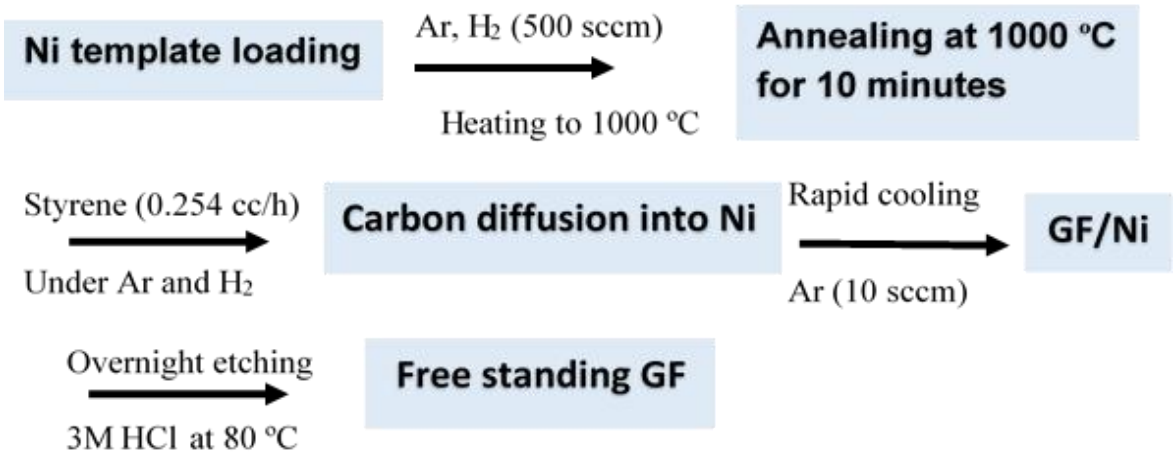

Fig 4.2 Schematic processes for the preparation of the GF.

4.2.2 Structural characterisation

Fig 4.3 shows µ-CT scan and SEM image of the Ni template and the GF product. Both foams look very similar. The fabricated GF had the same dimensions and shape as the Ni foams. Obviously, the GF, Fig 4.3b, copies and inherits the 3D structure and interconnectivity feature from the Ni foam, Fig 4.3 a.

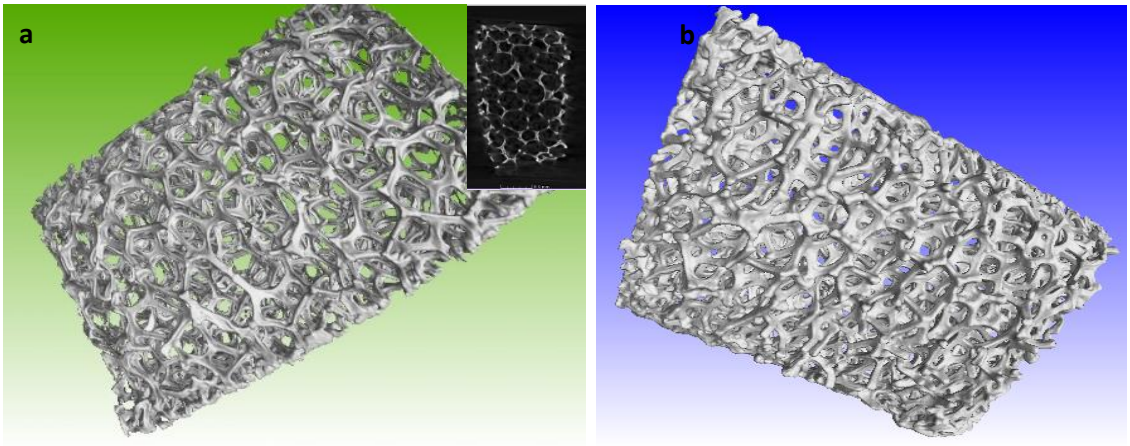

Fig 4.3. (a) µ-CT scan of Ni template, the inset shows Top volume of the CT scan of the Ni from and (b) SEM image of the GF.

Low magnification SEM images shown in Figs 4.4a-b illustrate the high porosity level of the GF foams. Fig 4.4a reveals a maximum size of *ca*. 200 µm for the macro pores. The high magnification image, Fig4.4d, shows some wrinkles and ripples on the graphene surface, which was expected from the polycrystalline Ni template.

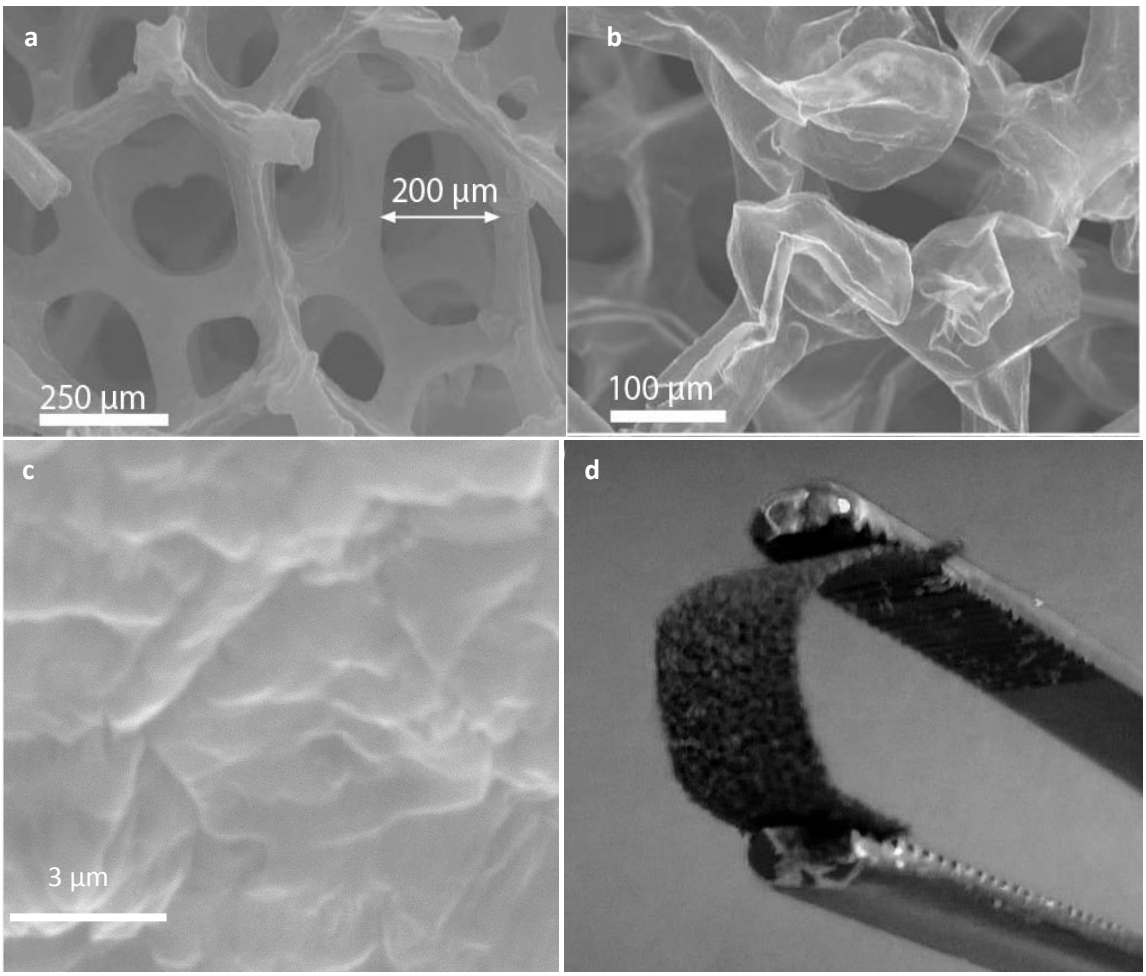

Fig 4.4 (a-c) SEM images of GF and (d) a photograph of a bended GF.

As shown in Fig 4.4d, the synthesised GFs are highly flexible and lightweight. Using the mass-dimension data, we obtained a density range of 3-5 mg cm^{-3} as the apparent density for the GFs.

EDS spectra of the GF, Fig 4.5a, shows only one carbon peak at 0.4 KeV and there is no observable signal for Ni. Fig 4.5b shows the XRD profile of the GF powder sample. The sharp peak at 26.512° represents the (002) plane of graphite, and the weak peak at *ca*. 55° belongs to the (004) plane.

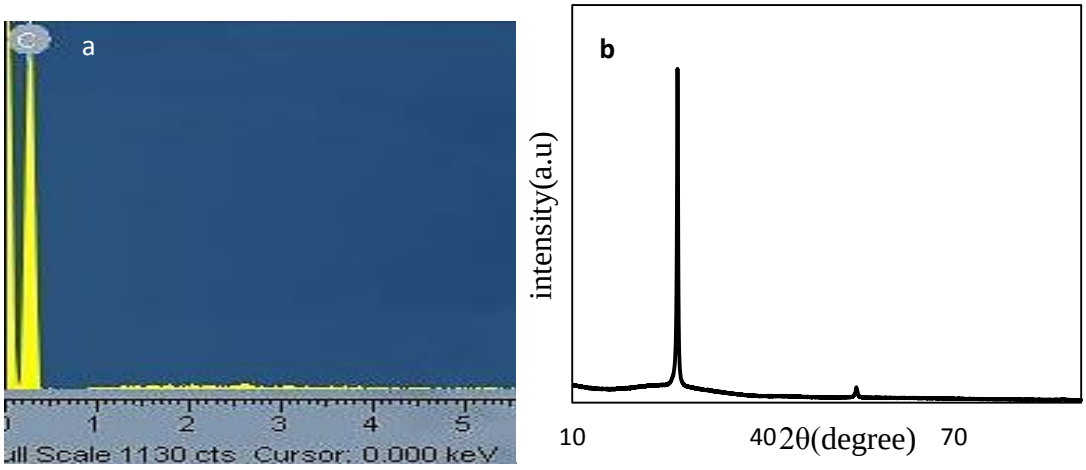

Fig 4.5 (a) EDS spectrum of the GF and (b) XRD pattern of the GF.

The thermal behaviour of the GF was studied by the TGA and the results are presented in Fig 4.6a. As shown, there are two weight loss regions: minor losses occurring before 600 °C, which is related to the removal of adsorbed water (at *ca.* 100 °C) and oxygen decomposition at higher temperatures (at *ca.* 200 ºC); and a major loss appearing in the temperature range of 600-750 °C, due to the complete oxidation of carbon.

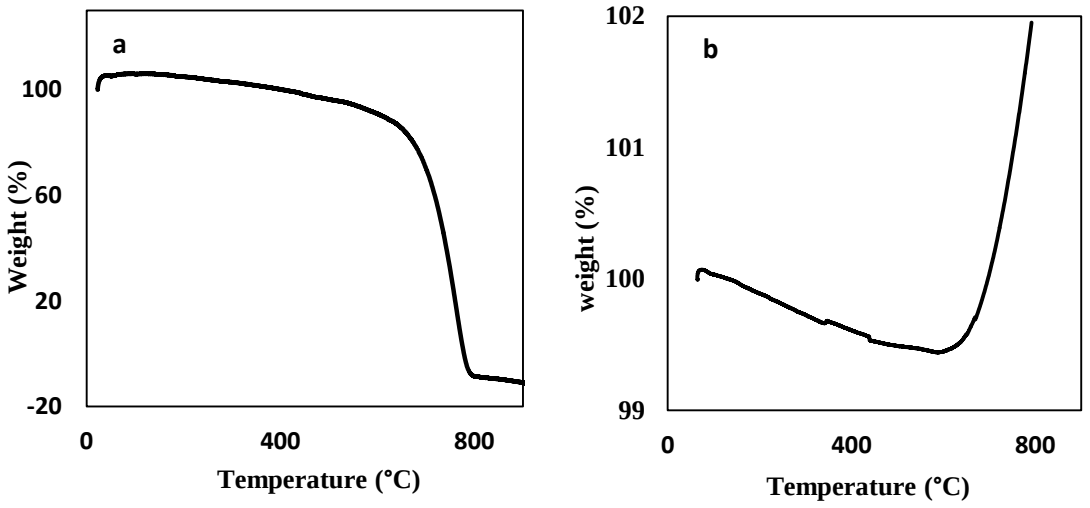

Fig 4.6 TGA profiles. (a) GF and (b) GF-Ni.

Comparing the TGA results of the GF (Fig 4.6a) with that of the GF-Ni (Fig 4.6b), we have found that the GF accounts for less than 1 wt. % of the GF-Ni composite, and that the 100% weight loss for the GF over 800 °C further confirms its purity.

The above EDS, XRD and TGA results have confirmed the complete removal of the Ni template during our etching process, and the successful production of pure 3D graphene foams.

Fig 4.7 shows the result of the Raman spectroscopy. The spectrum shows two intense peaks at 1574 cm^{-1} (G) and at 2720 cm^{-1} (2D) .The position and intensity of the Raman peaks give valuable information about the defect level, the number of graphene layers or the sp^3 hybrid phase [180].

The G peak is the E2g mode of graphite and is related to the in-plane stretch vibration of the C=C pair. The 2D mode is two phonon bonds, activated by double resonance at the zone boundary [180]. Ignorable effect of the D mode at ≈ 1300 cm^{-1} indicates a perfect crystal structure of the foam, and a carbon monolithic-like structure.

As shown, the intensity of the 2D peak is lower than that of the G peak, revealing the few layer feature of the GF[181]. In a single layer graphene, the intensity of the 2D peak (I_{2D}) is higher than that of I_G, and in a bilayer graphene, I_G and I_{2D} are almost equal.

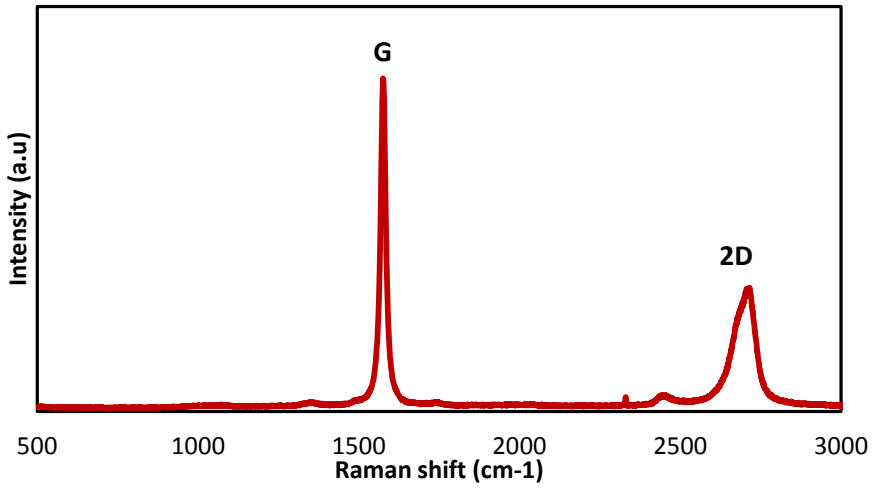

Fig 4.7 Raman spectrum of the GF.

To directly visualise the graphene flakes and to obtain a better understanding of the quality of the GFs, TEM measurement was carried out and the results are presented in Fig 4.8.

Fig 4.8a shows a large size graphene flake with folded areas. The average size of observed graphene flakes is about 4 µm. Fig 4.8b shows an HRTEM image of graphene flakes, exhibiting the layer numbers vary from 2-3 in some flakes to 9-15 in others. Obviously, the thickness of the graphene flakes is not homogenous. It is know that with the Ni-assisted CVD method, it is very challenging to control the numbers of the graphene layer[23,174,182,183].

The interlayer spacing was found to be 0.34 nm which is consistent with the d value calculated from the XRD data.

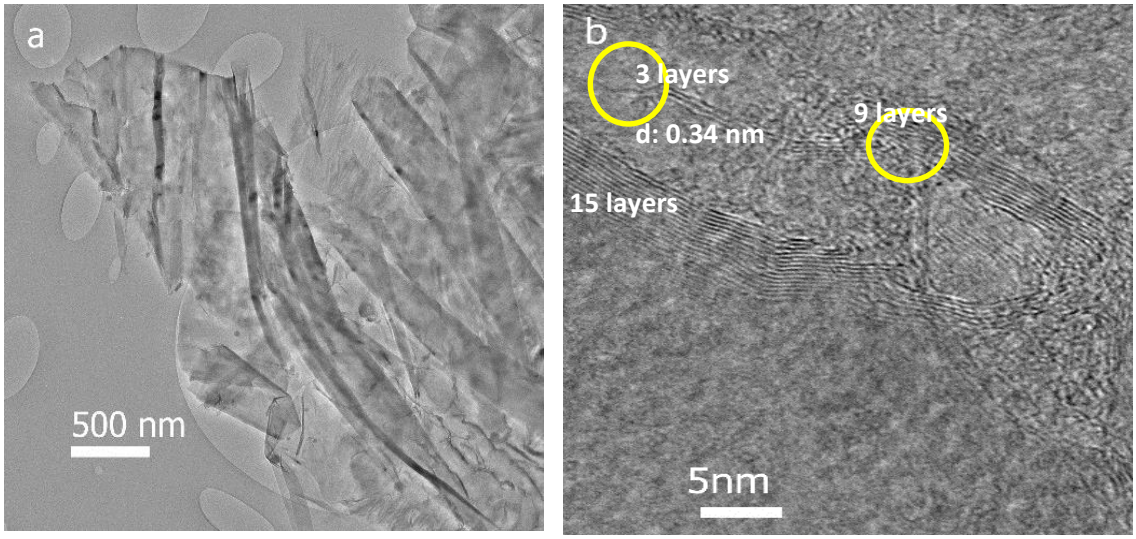

Fig 4.8 TEM images of the GF: (a) low resolution TEM image and (b) HRTEM of the produced graphene.

4.2.3 Electrical conductivity of the GF

The electrical conductivity of the GFs was tested using the two-probe method, which involves imbedding copper wires in the GFs and then securing them with silver paste. Fig 4.9 shows an image of the GF during electrical conductivity test. The measured resistance of the tested GF was 25 Ω.

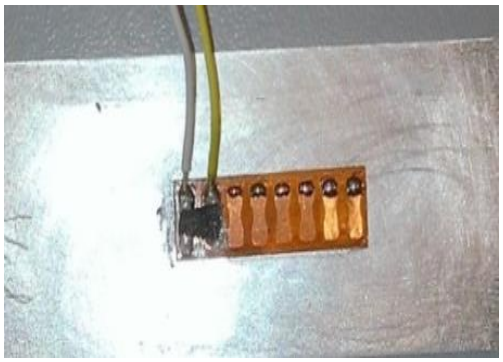

Fig 4.9 Electrical conductivity measurement of the GF.

Using the $\rho = \frac{RA}{l}$ equation, and the dimension data of the sample which were 9.8 x 3.2 x 1.7 mm^3, we obtained a value of 0.0139 Ω m as the resistivity of the GF. Further

based on $\sigma = \frac{1}{\rho}$, a value of 72.06 S/m (Siemens per metre) was obtained as the electrical conductivity (σ) of the GF. This is quite high when compared with other 3D carbon forms, such as the carbon aerogels (CNT aerogels) with similar or even higher densities [184-186], though it is 2-3 magnitude of orders lower than the electrical conductivity of a 2D graphene sheet or the ultrathin graphite foams reported by Ruoff's group [187].

The good electrical conductivity of the foam could be due to the reduced resistance at the junction between graphene sheets which allows for efficient charge transfer [187,188]. A better electrical conductivity can be achieved by increasing the density of the GF [184].

4.2.4 Electrochemical study of the GF

Electrochemical properties of the GF were investigated using a three-electrode cell. Fig 4.10 shows the CV results of the GF in 0.5 M KCl, at a scan rate of 0.1 Vs^{-1}. The electrode shows a rectangular shape which is a typical behaviour of double layer capacitors. However, the recorded currents do not show any improvement over reported performance of traditional carbon materials, as they are intrinsically capacitive materials and store charge via ion adsorption and the formation of double layer at the electrode–electrolyte interface[189]. Moreover, apart from those intrinsic parameters such as the π-π stacking which affects adversely the conductivity of the graphene-based materials, the fact that our GFs are extremely lightweight (ρ= 3-5 mg cm^3) and highly porous, further reduces the current values.

We believe that by introducing more mesopores (2-50 nm) and nano pores (1-2 nm) into the foam, and reducing the amount of macropores, a better specific capacitance can be achieved for the pristine graphene foam. It was discussed that a pore size

close to the size of the solvated ions, or slightly large are very beneficial for increasing the charge storage capacity. Some studies, argued that charge storage can also occur in pores smaller than 1 nm, however it is still a controversial debate as the mechanism of electrosorption is different in various pores [190-193] .

The suitability of the GF as electrode matrix was investigated by performing electrochemical tests, and Fig 4.10 shows a cyclic voltammetry (CV) curve of the GF. The stability of the GF materials was assessed by running the cyclic voltammetry test for a long time. As shown in the results, the foam electrode ideally and surprisingly kept its initial current values and electrochemical features after thousands of CV cycles.

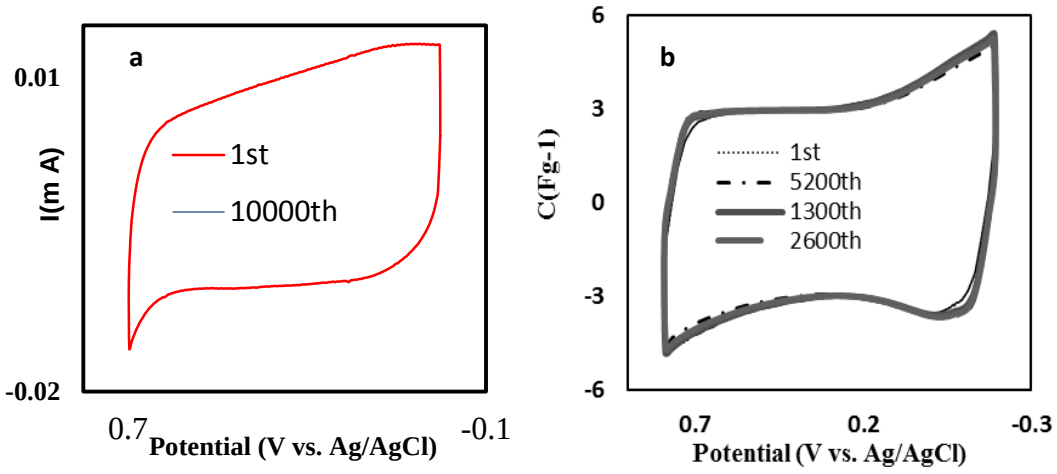

Fig 4.10 cyclic voltammetry of GF (a, b) at scan rate of 0.1 Vs^{-1}

The pure GF electrode does not show any capacity fading after 10,000 of charge-discharge, as the 1st and the 10,000th cycle overlaps with each other completely. From $C = \frac{I}{m\gamma}$ (4.1), where I is the current, *m* is the GF weight and *γ* is the potential scan rate, a value of 3 F g^{-1} was obtained for the 1st and the 10,000th cycle of charge-

-discharge. This 100% capacity retention and this superior consistency arise mainly from the excellent mechanical properties of the interconnected porous network of the synthesized GF. This feature, together with the open pore and mechanical excellency, enables the foam to be used as an ideal scaffold for producing 3D graphene-based electrochemical composites. The detailed mechanical property assessments of the GFs will be presented in chapter 7.

4.3 CVD synthesis of graphene on copper

Graphene were also synthesised by using the CVD method on a Cu foil substrate, based on the carbon atoms surface deposition mechanism [175].

For this synthesis, we first tried the same experimental parameters used for Ni-assisted synthesis of GF. We used the same styrene concentration and the same flow rates of H_2 (200 sccm) and Ar (300 sccm). We did not observe any graphene formation at that case and our characterisation tests such as Raman and SEM, did not detect any graphene islands. However, upon increasing the flow rate of H_2 to 300 (sccm), no change in the mix flow rate, but the flow rate of Ar decreased accordingly to maintain the total flow rate, graphene flakes were observed. This difference can be related to the different growth mechanism on Ni and Cu.

In contrast to the Ni which has high carbon solubility[31], Cu has limited carbon solubility . Here, however, the graphene growth is surface restricted and carbon atoms are directly deposited on the Cu surface, without segregation as did in Ni[175] . Thus H_2 plays important role here as catalyst[171]. H_2 has a catalytic effect on the graphene

growth on the Cu. It activates the surface of Cu for carbon bounding. It was shown that hydrogen pressure affects the size and shape of the graphene flake [171].

Fig 4.11shows an SEM image of the graphene, prior to the Cu template being etched away. The grain boundaries are clearly visible in some of these flakes. Fig 4.12b shows their Raman spectra.

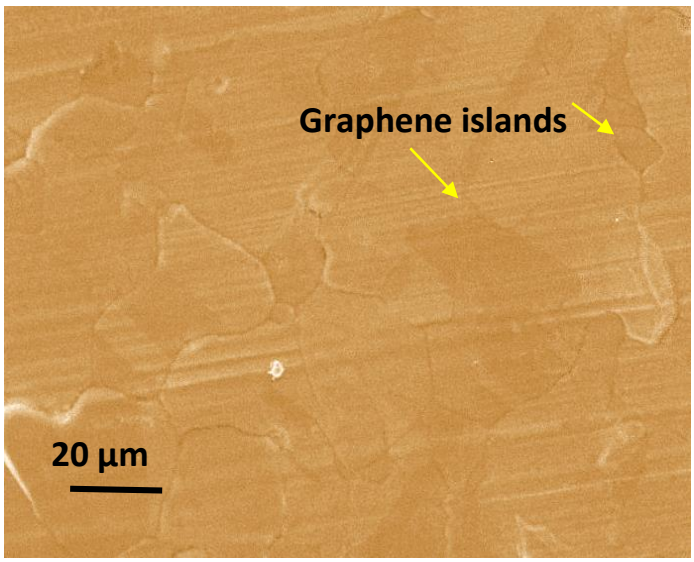

Fig 4.11 SEM image of the graphene grown on a Cu foil

Similar to the Raman spectrum of the 3D GF, the spectra show signals for the G and 2D peaks. Furthermore, the signal of D peak is very strong for the produced graphene on Cu, indicating a high level of defects in the sample. These defects could be due to the impurity and non-regular shape of graphene and also could be attributed to the edge structures of the sheet, as they are treated as defects by the Raman spectroscopy even if the structure is indeed perfect.

The effect of the H_2 flow rate on the grown graphene was also investigated. We noticed that increasing the rate of H_2 results in the more carbon coverage formation

on the Cu substrate, regardless of the numbers of layer as we did not investigate it thoroughly here.

This effect can be seen by comparing the Raman spectra shown in Fig 4.12. When, the flow rate of H2 was 300 (sccm), Fig 4.12a, the intensity of the D peak was comparable to that of the G peak and the 2D peak is slightly lower than G peak. But by further increasing the H2 flow rate (to 400 sccm), more graphene islands were detected and the intensity of D peak decreased and obviously G peak becomes more pronounced, all indicating the formation of more graphene layer[194].

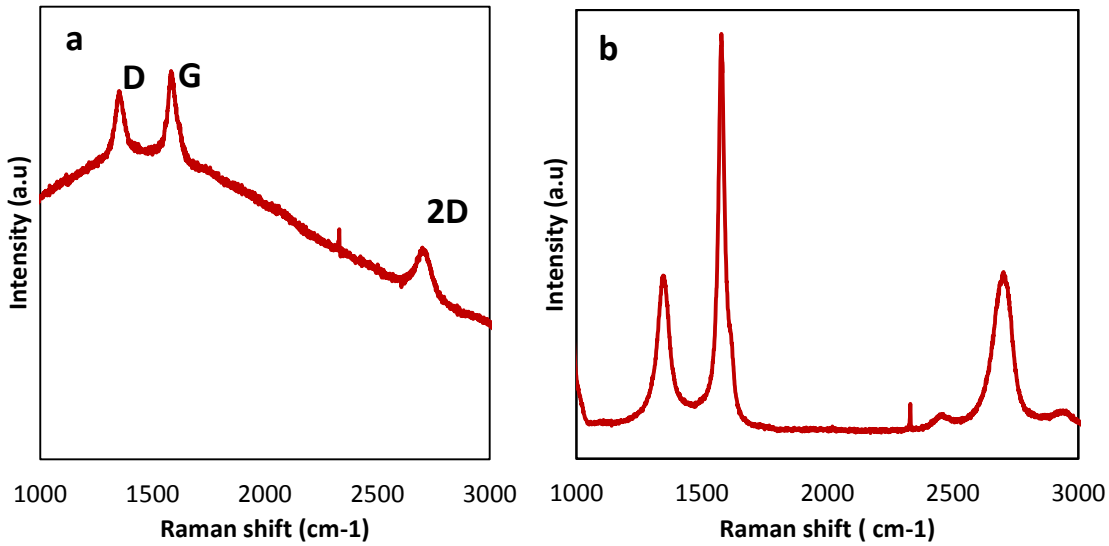

Fig 4.12 Raman spectra of graphene on Cu. (a) synthesised at a flow rat ratio of $\frac{Ar}{H_2} > 1$, and (b) at a ratio of $\frac{Ar}{H_2} < 1$.

Furthermore, the position of the peaks is different in the two graphs. The G peak upshifted from 1569 cm^{-1} in Fig 4.12a to 1579 cm^{-1} in Fig 4.12b. The 2D peak also upshifted. The position of the G and 2D peaks and their intensities depend significantly on the number of layers[195].

In this research, we observed a continuous change, upon modifying our synthesis procedures and thus the quality of the product. Generally, by increasing the number of graphene layer, both G and D peak upshifted and the intensity of D peak decreased significantly.

4.4 Summary

In this chapter, 3D GFs and 2D graphene flakes were synthesised and characterised. The results showed that the number of graphene layer is highly influenced by the synthesis conditions, such as the flow rates of H_2, the Styrene concentration, the deposition time and also the physical properties of the template. The synthesised GFs are 3D interconnected carbon monolithic-like networks, with a density range of 3 - 5 mg cm^{-3}, thickness of 1.7 mm, and various pore sizes. The 3D foam, consisting of few layer graphene, exhibited very high quality, defect free monolithic carbon network with high flexibility Electrochemical characterisation revealed a specific capacitance of *ca.* 3 F g^{-1}, and an impressive 100% capacity retention after 10,000 of CV cycles, for the GFs. These 3D GFs are an ideal matrix for designing new 3D electrodes for energy storage and conversion.

Chapter 5 : GF-Conducting polymers composites as electrode materials for supercapacitors

5.1 Introduction

Supercapacitors are considered as one of the most important EES systems, since they hold the hope of achieving battery-like specific energy along with capacitor-like specific power. Towards the ultimate goals of harnessing high capacity, high specific energy ($Whkg^{-1}$), high specific power (Wkg^{-1}) and good cycle life (>100,0000 cycles [196]) for the next generation of supercapacitors, numerous strategies [197-199] and a wide range of composite materials[191,198,200] have been investigated to date [176,178,179].

One of the most promising proposed structures is the 3D electrode architecture in which its electroactive materials do not suffer from the high trade-off between the power and the energy as they do in a traditional plane electrode. In a 3D design, the third dimension allows for storing more energy without the need for increasing the thickness of the electroactive materials, thus the specific power is less compromised [187,201-204]. This concept, 3D architecture, can be introduced to different materials and systems. One interesting approach is to produce 3D CNT-based composites [205,206], and graphene-based composites [80,207-209], partnered with conducting polymers [208,210-212] and transition metal oxides [213,214].

Conducting polymers (CPs) such as Polypyrrole (PPY) and Polyaniline (PANI) are promising pseudocapacitive electrode materials for supercapacitor applications. They

are easy to synthesis from both aqueous and non-aqueous solvent, inexpensive, environmentally friendly [215], and are highly conductive in doped states [216]. These features allow for fast doping/un-doping process [200]. However, CPs such as PPY, which is of special interest in this context, suffer from low mechanical stability and pulverization during the repeated charge-discharge process, and they lose more than 50% of their initial capacitance after only a few hundreds of charge-discharge cycles [217-220]. To counter this poor cycle life issue, the incorporation of CPs into a strong and conductive 3D matrix such as GF, to create a robust composite electrode appears to be the right way forward, and in fact this approach forms the driving force of our research.

This chapter will describe our attempts to create such composites by combining the CPs and GFs, in an effort to develop high performance EES devices. In the first part, the synthesis and structure of the composites will be fully characterised, and in the second part we will evaluate their electrochemical performance.

5.2. The synthesis of PPY-GF composites

The PPY films were synthesised both chemically and electrochemically on the GFs, through Pyrrole oxidation as illustrated in Fig 5.1. Table 5.1 summarises the synthesis conditions used to fabricate the composite materials. We produced different electrodes to investigate how changing the synthesis parameters would affect the structural and electrochemical performance of the electrode. However, since the electrochemical synthesise routes are not always economically feasible, the main focus will be on the chemically prepared electrodes.

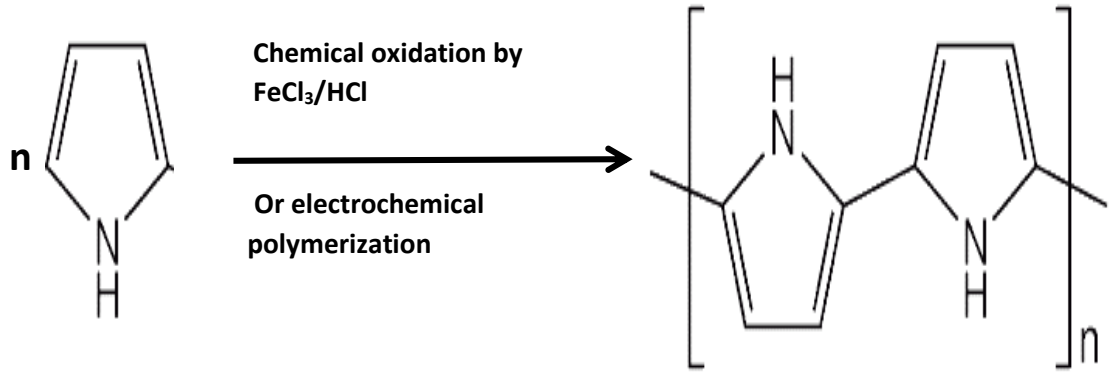

Fig 5.1 Schematic of Pyrrole polymerisation through monomer oxidation process.

For in-situ chemical polymerisation, two composites were prepared: PPY-GF1 and PPY-GF2. As shown in Table 5.1, both composites were prepared by the chemical polymerisation of 0.1 M Pyrrole with the oxidant $FeCl_3$. In PPY-GF1, we adopted a 15 h overnight process to ensure the completeness of the polymerisation. The polymerisation time in PPY-GF2 was 3 h. PPY-GF3 composite was prepared by an electrochemical technique and the deposition time was 200 s.

Table 5.1 Preparation conditions of various electrodes.

Electrode	Preparation method	Deposition time
PPY	Electrochemical	500 sec
PPY-GF1	Chemical	15 h
PPY-GF2	Chemical	3 h
PPY-GF3	Electrochemical	200 s
PANI-GF	Electrochemical	400 s

In the PPY-GF composites, the PPY films are bonded non-covalently and mainly through π-π stacking to the GF [221], although the formation of hydrogen bonds (between the existing hydrogen in pyrrole and oxygen groups in graphene, if there is any) is also likely to happen [222]. In the non-covalent bond, the graphene sheets were negatively charged and PPY films were positively charged (p-doped), hence the two components were attached physically and electronically together through the electrostatic interactions [223]. The adhesion of the PPY chains to the graphene nanosheets was found to be sufficiently strong to resist removal after a few times of rinsing with distilled water or even after sonication process.

Regarding the π-π stacking between graphene sheets, it is notable that whilst such stacking may affect adversely the capacity of the electrode by reducing the accessible surface area of the GF, π-π interactions between the PPY and GF are the key factor to maintain the connection and integrity of the 3D composite electrode.

5.2.1 Structural characterisations of PPY-GF1 composites

Weight ratio between PPY and GF in PPY-GF1 composite was calculated from the TGA analysis. The TGA profile of the PPY-GF1 composite against GF and PPY is shown in Fig 5.2. As it can be seen from the graph, the PPY loses its weight completely at about 450 °C, while there is a minimal weight loss for the GF at the same temperature. Accordingly, a 65% weight loss in the PPY-GF1 at 450 °C (this position is marked in Fig. 5.2) indicates a 35% PPY content in the composite.

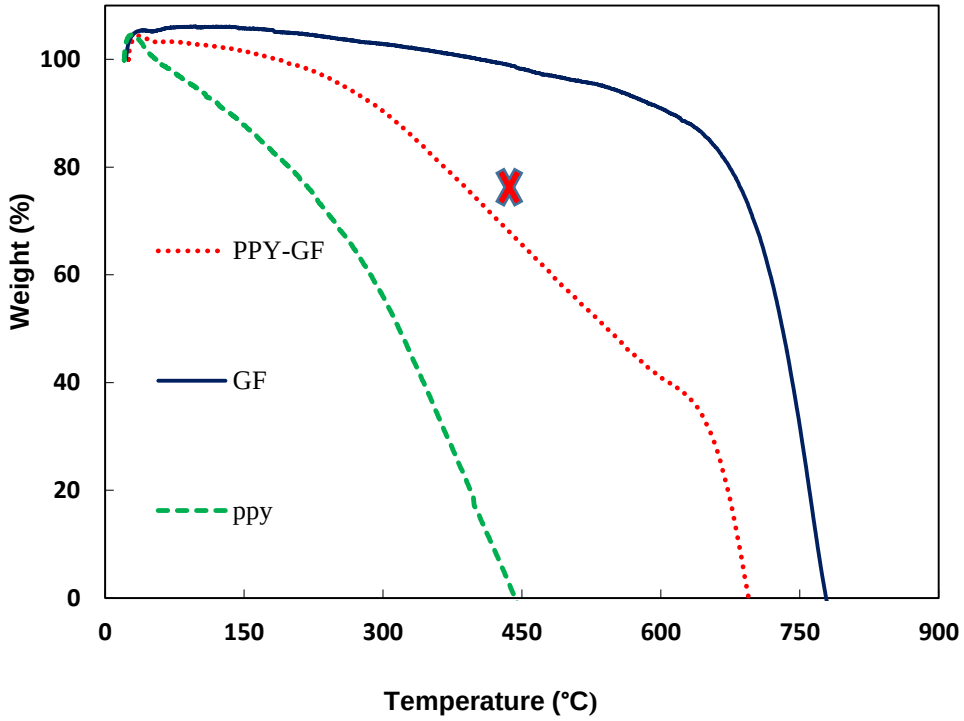

Fig 5.2 TGA profiles of PPY-GF1, GF and PPY.

Fig 5.3 shows SEM images of the GF, PPY and chemically polymerized PPY-GF1. The GF is highly flexible with an interconnected porous 3D network. The low magnification image shows an average value of 200 µm for macro pores. Fig 5.3b is an SEM image of the pure PPY in which polymer aggregation is very obvious. Low magnification SEM image of the composite, Fig 5.3.c, shows clearly the structural similarity between the GF and PPY-GF1 composite. In fact, the 3D composite mimics most of the structural features of the GF scaffold, the only main apparent difference is the thin film PPY coating which covers the surface of the GF almost uniformly, Fig 5.3.d.

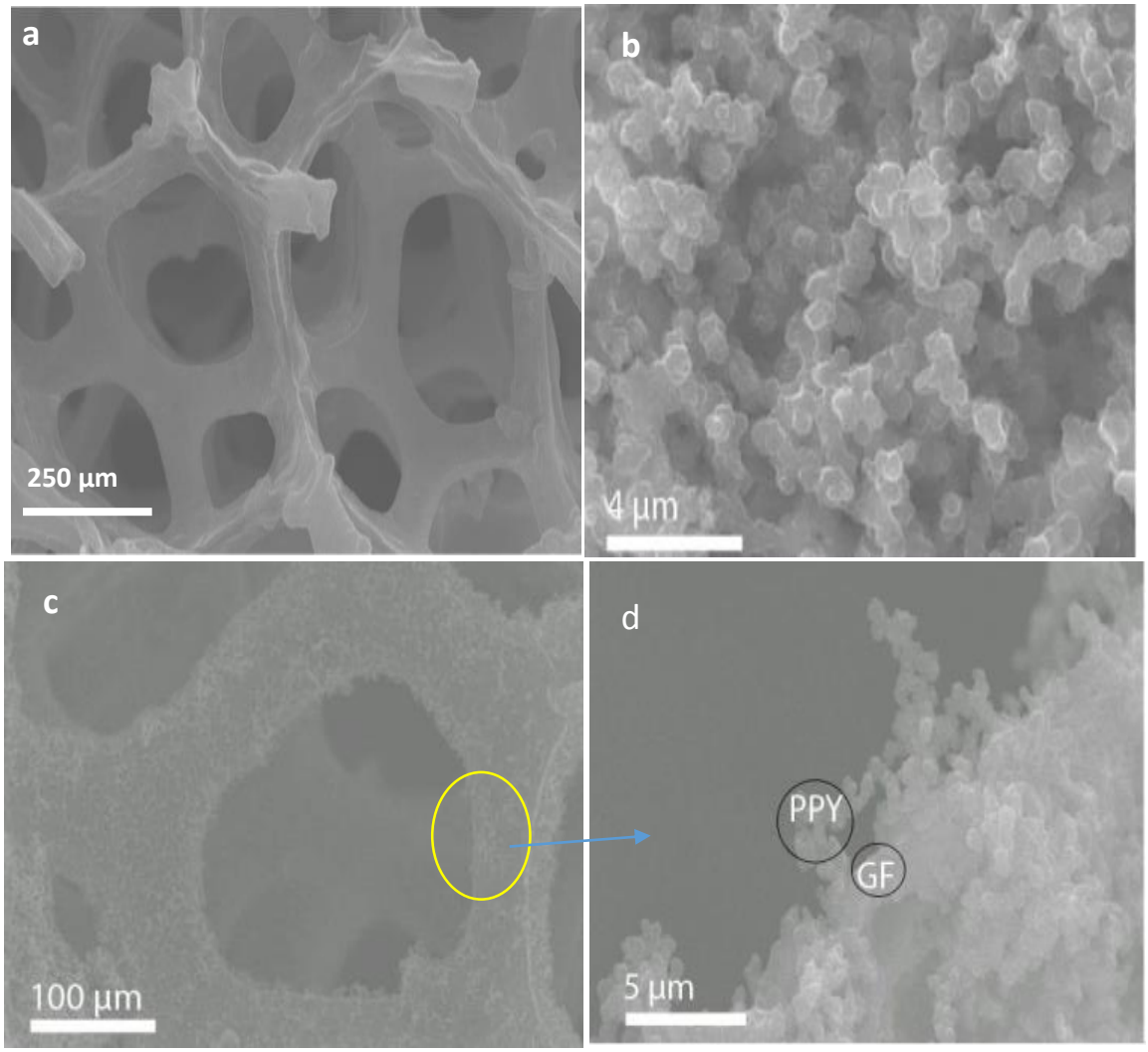

Fig 5.3 SEM images of GF, PPY and PPY-GF1. (a) GF, (b) PPY and (c-d) PPY-GF1.

Fig 5.4 shows TEM images of the PPY-GF1 composite. Fig 5.4a is a low magnification TEM image showing PPY-coated graphene sheets, and its high magnification image (Fig 5.4b) shows both the amorphous PPY and the graphene sheet. Graphene sheets are fully covered by the PPY, especially at the edges. This coexistence of the PPY films and the crystalline lattice of graphene sheets (with spacing value of 0.34 nm) is due to the successful assembly and good interactions between the PPY and GF [224].

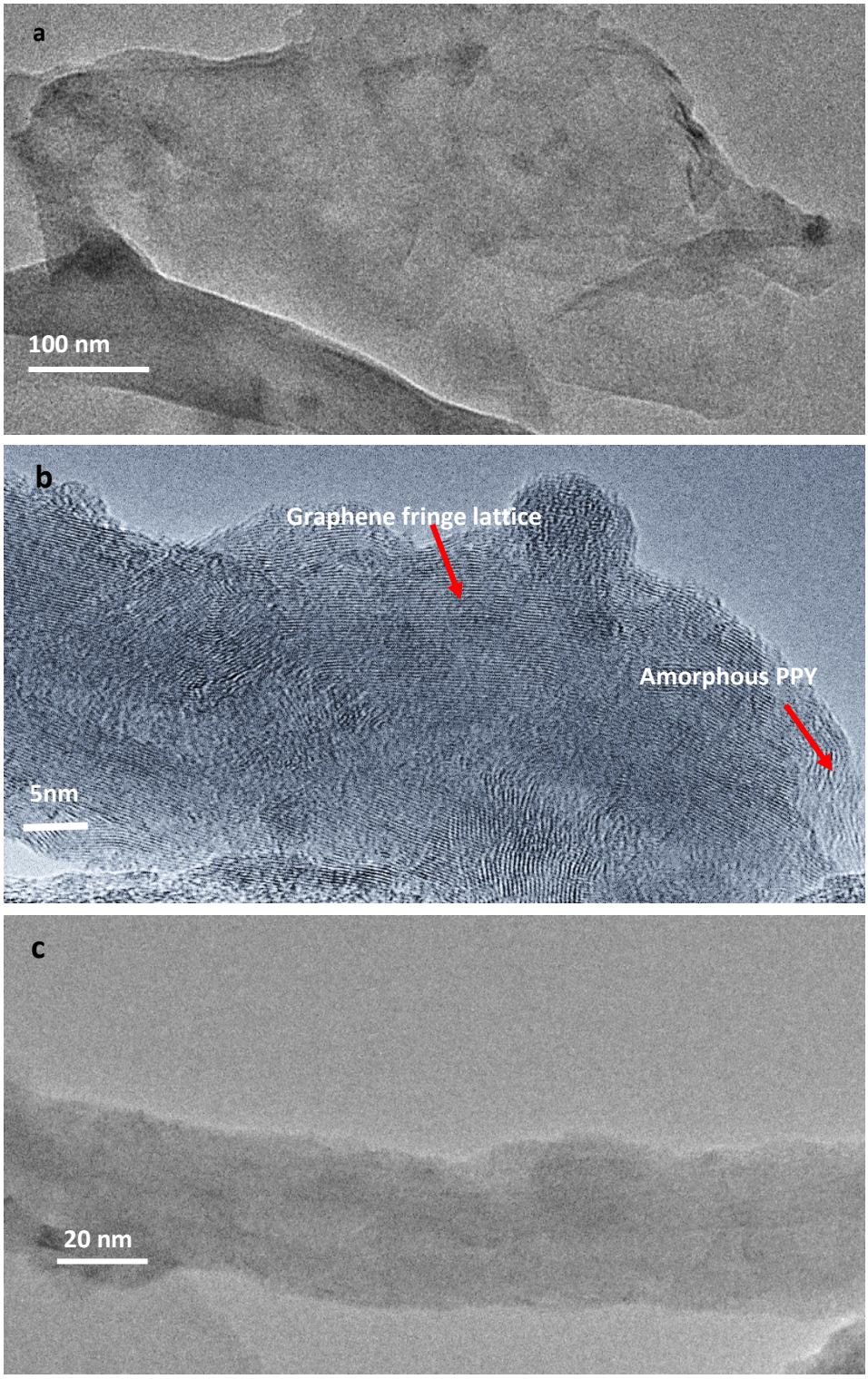

Fig 5.4 TEM images of the PPY-GF. (a)PPY-coated GF, (b) PPY-GF1 at high resolution, and (C) PPY-GF at low resolution.

As verified by the high resolution SEM image (Fig 5.3d) at microscopic level, the PPY chains are attached tightly to the GF and formed a full polymer coating rather than random deposition. At nano-scale, this type of interactions is also clear in Fig 5.4b. Such stable interface connections, via π-π interaction between aromatic ring and graphene sheets, and the micro-/nanostructure feature of the composite, play an important role in the electrochemical activity of the electrode [225].

Fig 5.5 displays the Raman spectra of the GF, PPY and PPY-GF1 composites. For the GF, two main peaks appeared at about 1572 cm^{-1} (G) and 2750 cm^{-1} (2D) [201].

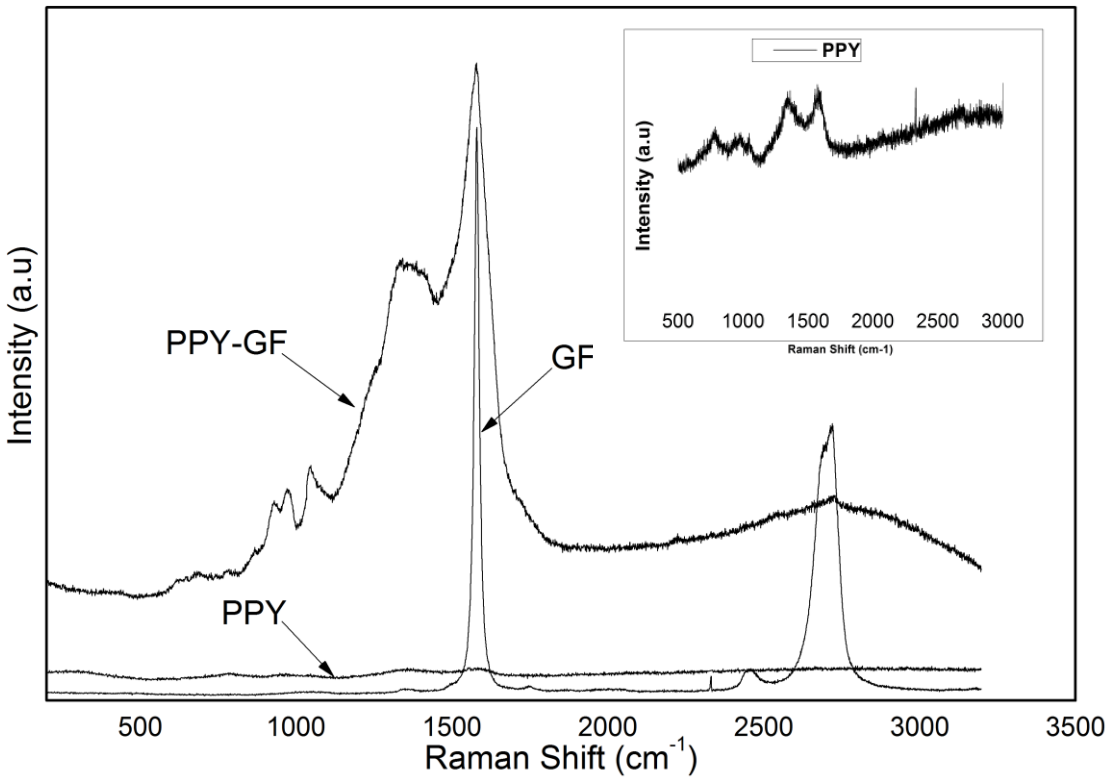

Fig 5.5 Raman spectra of the GF, PPY and PPY-GF1. The inset is an enlarged Raman spectrum of the PPY.

The Raman spectrum of the PPY-GF1 composite samples showed a combined feature of both GF and PPY. The PPY peaks appeared in the range of 800-1000 cm^{-1}, representing the N-H and C-H deformation of the Pyrrole ring [226]. The intense peak appeared at 1577cm^{-1} represents C=C stretching in the composites. As can be seen in the presented graph, the intensity and position of all 3 main peaks of graphene, D, G and 2D, are changed in the composite, and we believe that these change are not simply due to the PPY itself, rather it reflects impurity (charges) in the GF [227].

Noticeably, while the D peak was very weak in the GF spectrum, it is well pronounced in the composite due to the produced defects during the synthesis [228]. The G peak of GF upshifted in the composite and more interestingly the intensity of the 2D peak reduced dramatically in the composite. Obviously, these change are related directly to the PPY-GF formation. In fact, this Raman shifting and changes are consistent with earlier studies which found high dependency between these Raman bands and graphene doping. They observed similar upshifting for the G peak, and intensity reduction for the 2D peak in n-doped graphene [229]. As discussed earlier in the synthesis part, in the composite the PPY films are positively charged while graphene sheets are negatively charged, because aromatic molecules with electron-donating groups imposing n-doping (negatively charged) on graphene [227]. In agreement with other studies, the observed Raman band changes such as the reduced intensities of the 2D peak and the pronounced D peak in the composite are due to the increased charge concentration (n-doping) in graphene, via the successful PPY-GF interactions [227,230,231].

5.2.2 Electrochemical study of the PPY-GF1 composite

The electrochemical characterisation of the PPY-GF1 composite as a supercapacitor electrode was investigated by CV, Chronoamprometry, and Impedance spectroscopy using a three-electrode cell. For a better comparison, we also present the results of the GF and PPY here.

5.2.2.1 Cyclic voltammetry

Fig 5.6 shows the CV curves of the GF, PPY and PPY-GF1 at different scan rates in 0.5 M KCl electrolyte. Obviously, the electrodes exhibit different current values and CV shapes. In the CV plot of the GF (Fig 5.6a), a rectangular shape with small current values was recorded. The straight lines at both ends of the CV curve represent a fast charge-discharge process at the foam, and are indicative of the quick diffusion of the electrolyte ion into the GFs.

Using $C = \frac{I}{m\gamma}$ (5.1), where I is the current, m is the weight and γ is the potential scan rate, a value of 3 F g^{-1} as the specific capacitance and an areal capacitance of 4 mF cm^{-2} were obtained. As described earlier, these values stand in the middle of the reported values for carbon electrodes [232-234].

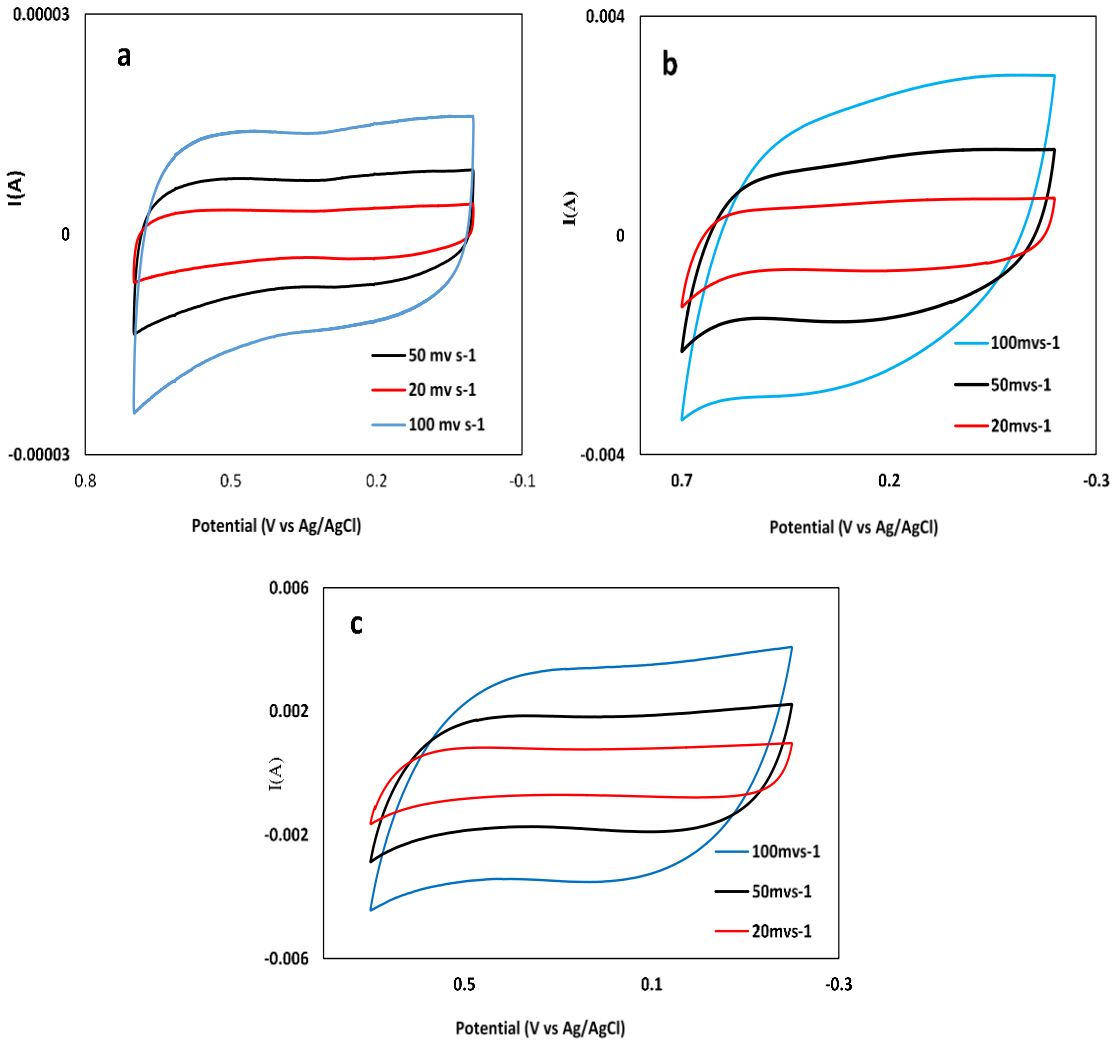

Fig 5.6 CV curves of different electrodes in 0.5 M KCl at different scan rates. (a) GF, (b) PPY, and (c) PPY-GF1.

The CV graphs of PPY and PPY-GF1 are shown in Fig 5.6b and Fig 5.6c respectively. Both the PPY and composite electrode show much higher current values than those of GF, as they store charges differently. Carbon materials, namely GF here, are double layer capacitance materials and they store charge via a reversible ion absorption at the electrode/electrolyte interface; whilst the PPY and PPY-GF1 composites are pseudocapacitive materials [235,236]. The energy stored in double layer capacitors is limited by the finite electrical charge separation at the interface of active electrode materials and the electrolyte. In

contrast, the process of energy storage in pseudocapacitive materials is beyond charge separation, and involves ion intercalation and redox reaction at the surface of the electroactive materials [225].

Compared with PPY (Fig 5.6b), the PPY-GF1 (Fig 5.6c) shows slightly higher current values, per the same foot area, though most of the current comes from the PPY. This difference could be attributed to the more efficient polymerisation process and an enhanced electron delocalisation along the PPY chains in the composite [225].

Similar to GF, the PPY-GF1 electrode also shows rectangular CV curves at various scan rates, Fig 5.6c, which indicates that these electrodes have good rate capability, and that even at high scan rates the electrolyte ions can still diffuse fast into the electrode [237]. Both rectangular feature of the CV and also its good rate performance is due to the GF scaffold [238]. As shown in Fig 5.6b, the CV curve of PPY at scan rate of 100 mV s^{-1} shows significant deviations from the rectangular shape, indicating a slow ion diffusion at high rates.

In fact, the template-assisted synthesis that we carried out, allows for transferring the main structural merits of the GF such as the pore distribution to the composite [239]. As the PPY-GF1 composites produced upon 3D conductive network, they benefit fundamentally from these inherited structural features. Ion diffusion occurs mainly through macropores in the composite, thus a much better rate performance than the pure PPY was obtained. This result further confirmed that the porous structure of the PPY-GF1 composite indeed played an important role in the rate performance in 3D composites, as discussed by El-kedy et.al [240].

5.2.2.2 Chronopotentiometry

The chronopotentiometry technique, also called galvanostatic charge-discharge, was used to study the change of the electrode potential as a function of time. In this research, the specific capacitances of the composite were calculated by using the charge-discharge results.

Fig 5.7 shows the charge-discharge curves of the GF (Fig 5.7a), PPY (Fig 5.7b) and PPY-GF1 (Fig 5.7c-e). The GF electrode shows a linear curve and very short charge-discharge time (Fig 5.7a), *ca*. 3 s, indicating a fast charge-discharge process. The PPY electrode shows a linear curve in a smaller potential range than the GF, and there is a significant ohmic drop at a larger potential window (Fig 5.7b).

The results for the PPY-GF1 electrodes are shown in Fig 5.7c-e. Compared with the PPY, the composite electrode shows a much smaller ohmic drop at the same potential windows and current density, indicating a facilitated charge transportation process in the latter electrode. Importantly, as shown in Fig 5.7e, even at a high current density of 5.2 A/g, a good linear relation between charge-discharge potentials and the time was recorded.

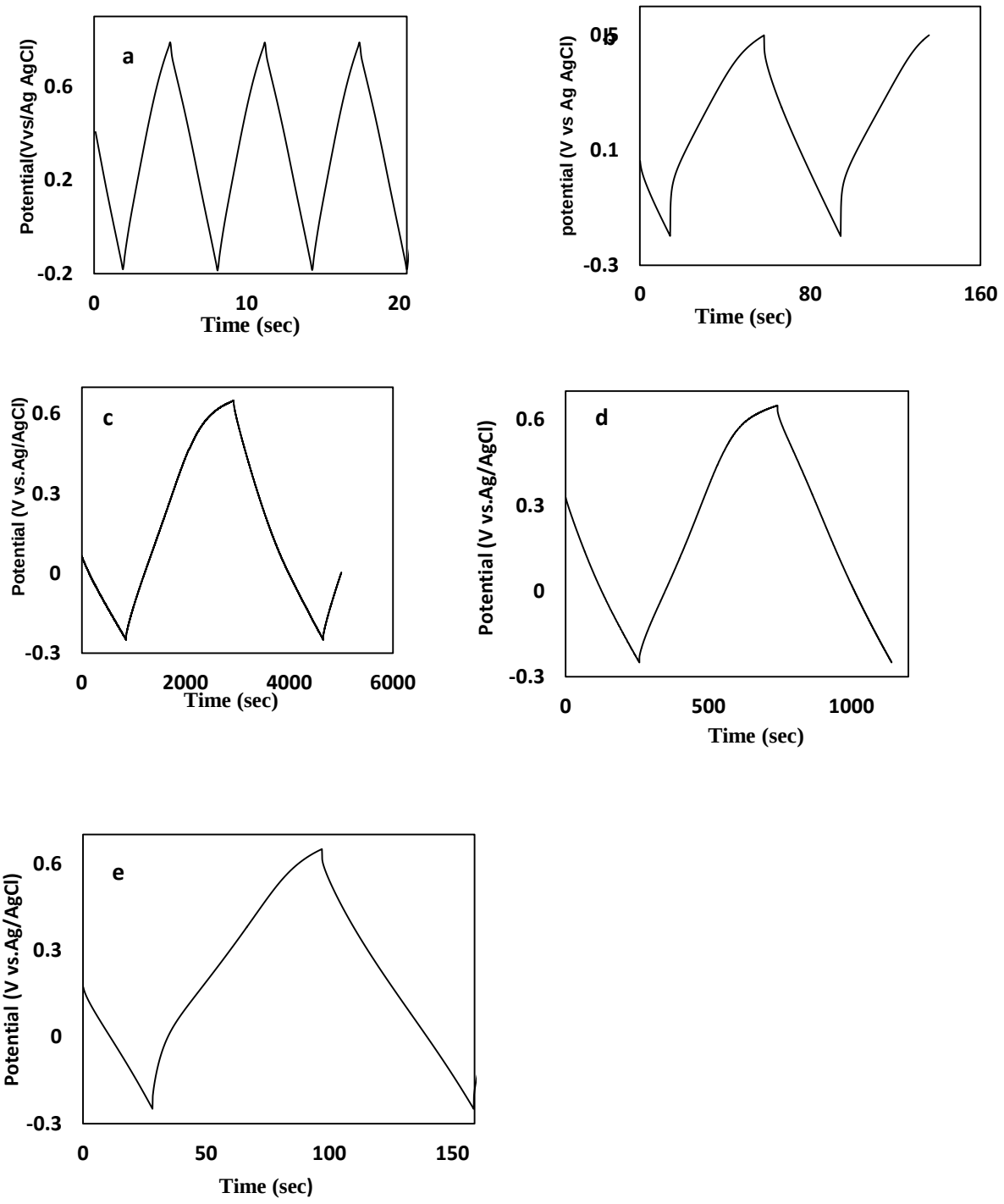

Fig 5.7 **Galvanostatic charge-discharge curves of the electrodes. (a) GF at 1 Ag^{-1}, (b) PPY at 1.5 Ag^{-1}, (c) PPY-GF1 at 0.33 Ag^{-1}, (d) PPY-GF at 1.1 Ag^{-1}, and (e) PPY-GF1 at 5.2 Ag^{-1}.**

Using equation 5.2 and the data for discharge and charge time (t_d and t_c), we found that all the electrode had very good columbic efficiency (ε_c). It is 100% for GF, and more than 95% for the composites.

$$\varepsilon_c = \frac{t_d}{t_c} \times 100 \quad (5.2)$$

The specific capacitance of the electrode was calculated by using the results of galvanostatic charge-discharge tests and the following equation:

$$C_m = \frac{I \times t}{V \times m} \quad (5.3)$$

where, C_m is the specific capacitance, I is the current, V the potential windows, and t is the discharge time.

Table 5.2 lists the specific discharge capacitances of the three electrodes: GF, PPY and PPY-GF1 obtained at different current densities. These values are amongst the highest reported capacities, against PPY-graphene [217,241,242], PPY-graphite [243,244], and PPY-CNT composite electrodes [245].

Table 5.2 Specific Capacitance of the electrodes at different current densities.

Electrode	Discharge capacitance (Fg^{-1})	Current density (Ag^{-1})
GF	3.5	1
PPY	414	1
PPY-GF1	660	0. 34
PPY-GF1	570	1.1

PPY-GF1	403	5.2

From Equation (5.3), maximum specific capacitance values of 660 Fg^{-1} at 0.34 Ag^{-1}, 570 Fg^{-1} at 1.1 Ag^{-1} and 403 Fg^{-1} at 5.2 Ag^{-1} were obtained for the PPY-GF electrode. At 1.1 Ag^{-1}, the specific capacitance of the composite reached 570 Fg^{-1}, which is much higher than the mathematical combination of the PPY and GF (0.65 C_{GF} + 0.35 C_{PPY} = 138 Fg^{-1}).

The enhanced capacity is believed to arise from three key factors: (1) the intrinsic interconnected 3D architecture of the GF and its open porosity feature [205], (2) The core-shell structure of the composite, as evidenced by TEM, and (3) PPY contribution to the charge storage and its high conductivity.

In an interconnected 3D network, the electrons do not need to travel a long distance to reach the current collector, rather they are connected to many individual pathways to the current collector and thus benefit from direct electron pathways. Furthermore, the core-shell structure of the composite and literally the porous PPY shell allows for much higher charge storage capacity due to the pseudocapacitive nature of CPs, and finally the open porosity feature of the electrode provides many effective routes for the charge transportation, and hence allows for more energy storage into these composite materials [246,247].

5.2.2.3 Impedance spectroscopy

The electrochemical kinetics of the electrode at high and low frequencies were investigated by conducting impedance spectroscopy measurements. The impedance behaviour at high frequencies gives a clear examination on ohmic resistance and knee frequency of the electrodes. Knee frequency indicates the

transfer between capacitive and diffusive behaviour [248]. In this research, the A.C impedance tests were performed at the frequency range of 100 kHz - 0.1 Hz with an AC signal of 5 mV, and the results are shown in Fig 5.8.

Starting with GF (Fig 5.8a-b), there is an equivalent series resistance which arises mainly from the contact resistance between the GF and the current collector, and it can be largely reduced by improving the electrical contact between the electrode and current collector. For example, in the case of the plane 2D electrode, where the electroactive materials mostly dropped on the working electrode, there is generally a better electrical contact between the two components [249]. However, as we aimed to investigating the properties of the free standing 3D electrodes, we purposely eliminated binder from the synthesis process. Further, in the cell, the whole components, including the two electrodes and the separator, are pressed together, thus the cell components can benefit from a good connectivity.

The Nyquist plot of the GF, Fig 5.8a-b, shows a vertical line at the high frequencies which corresponds to the “angel phase” of 90 degree, and it indicates an ideal capacitive behaviour. For the PPY electrode (Fig 5.8c), the straight line at about 45° corresponds to the Warburg impedance and it is related to the impedance to the diffusion of electrolyte into the pores of the electrode (during ion intercalation and de-intercalation).

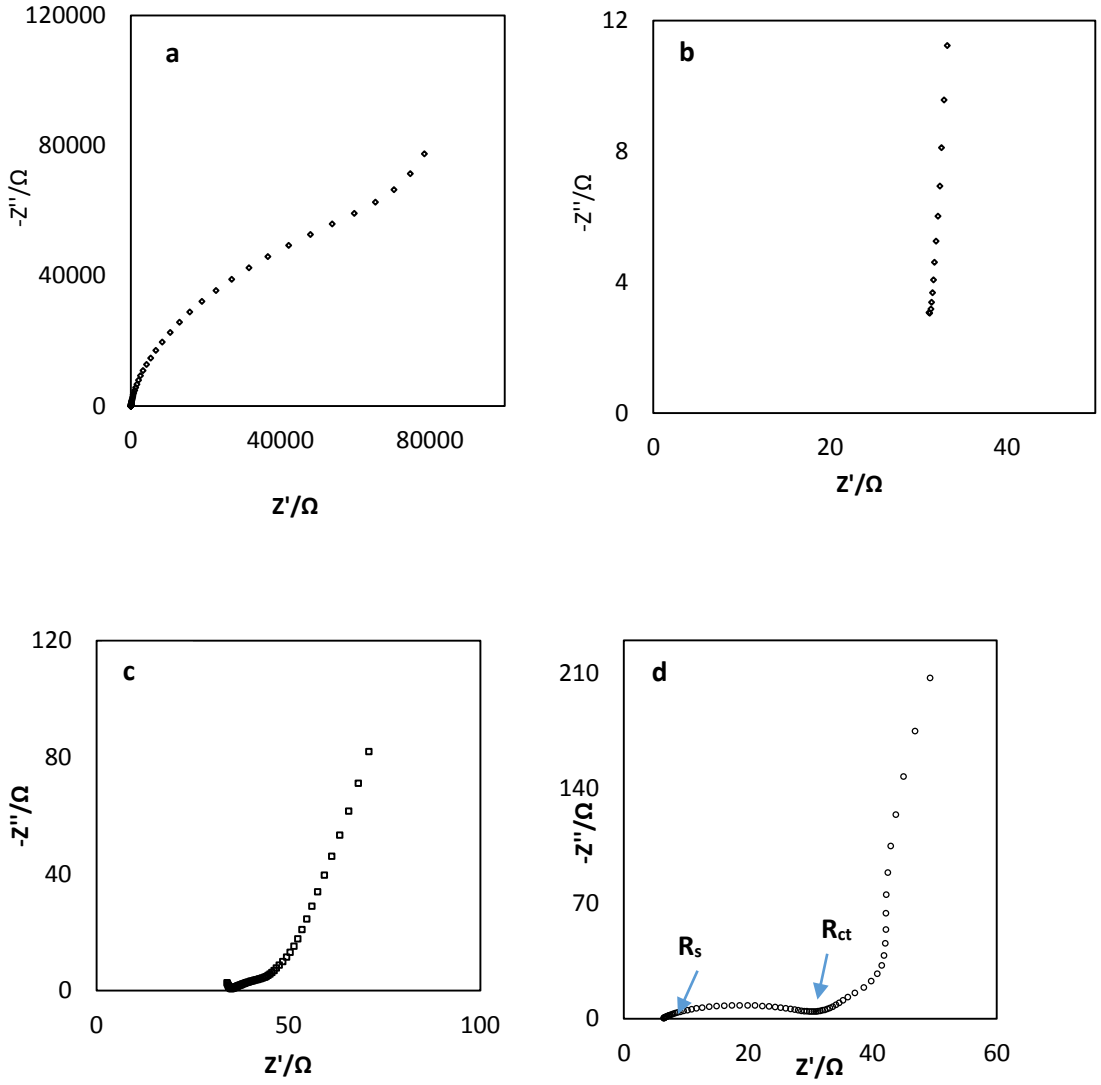

Fig 5.8 Nyquist plots of different electrodes in 0.5 M KCl: (a) GF, (b) magnified Nyquist plot of GF at high frequencies, (c) Nyquist plot of the PPY, and (d) Nyquist plot of the PPY-GF1.

For both PPY and PPY-GF1 electrodes, their impedances consist of three parts: (1) the equivalent series resistance, R_S (or uncompensated ohmic resistance) which is the intercept of the real impedance, and (2) the arc or semicircle part at medium frequencies which is related to the charge transfer process at

electrode/electrolyte interface, R_{ct}, and finally (3) the inclined line at low frequencies due to diffusion resistance [224,250].

At low frequencies, the impedance plot of the composite electrode exhibits mainly a high slope straight line, with phase degree of 85, indicating the lower internal resistance (compared with the PPY which has a phase of 45°) and the improved ion accessibility in the composite. The Warburg impedance results from the frequency dependent nature of the ion diffusion process in the materials [224,251].

5.2.2.4 Cycle life

The stability of the synthesised electrodes were assessed by running cyclic voltammetry and Chronopotentiometry tests for thousands of cycles and the results are presented in Fig 5.9. In the GF, Fig 5.9a, the 1st and 10,000th cycles are almost completely overlapped with each other, demonstrating no capacity fading after 10,000 times of charge-discharge. For the PPY, though this electrode shows a near-rectangular CV curve and good current densities at the first cycle, it cannot maintain these current values at the next cycles, gradually degraded in performance. From the 1st to the 1,000th cycle, a 30% current reduction was recorded, indicating a possible structural collapse during the repeated charge-discharge tests. For some of the tests with this electrode, PPY, we even recorded a very high capacitance lose and structure degradation after only few hundreds of CV cycles, indicating the incapability of the polymer to sustain reparative Cl^- intercalation and de-intercalation.

In contrast to the PPY, the composite electrode does not show any current reduction and capacity fading up to 6,000 charge-discharge cycles, as shown in Fig 5.9c. Even the shapes of the CV curves remain almost identical to the initial one. This 100%

capacity retention and superior consistency arises mainly from the excellent mechanical properties (both robust and flexible) of the GFs and its efficient ion and charge transportation pathways.

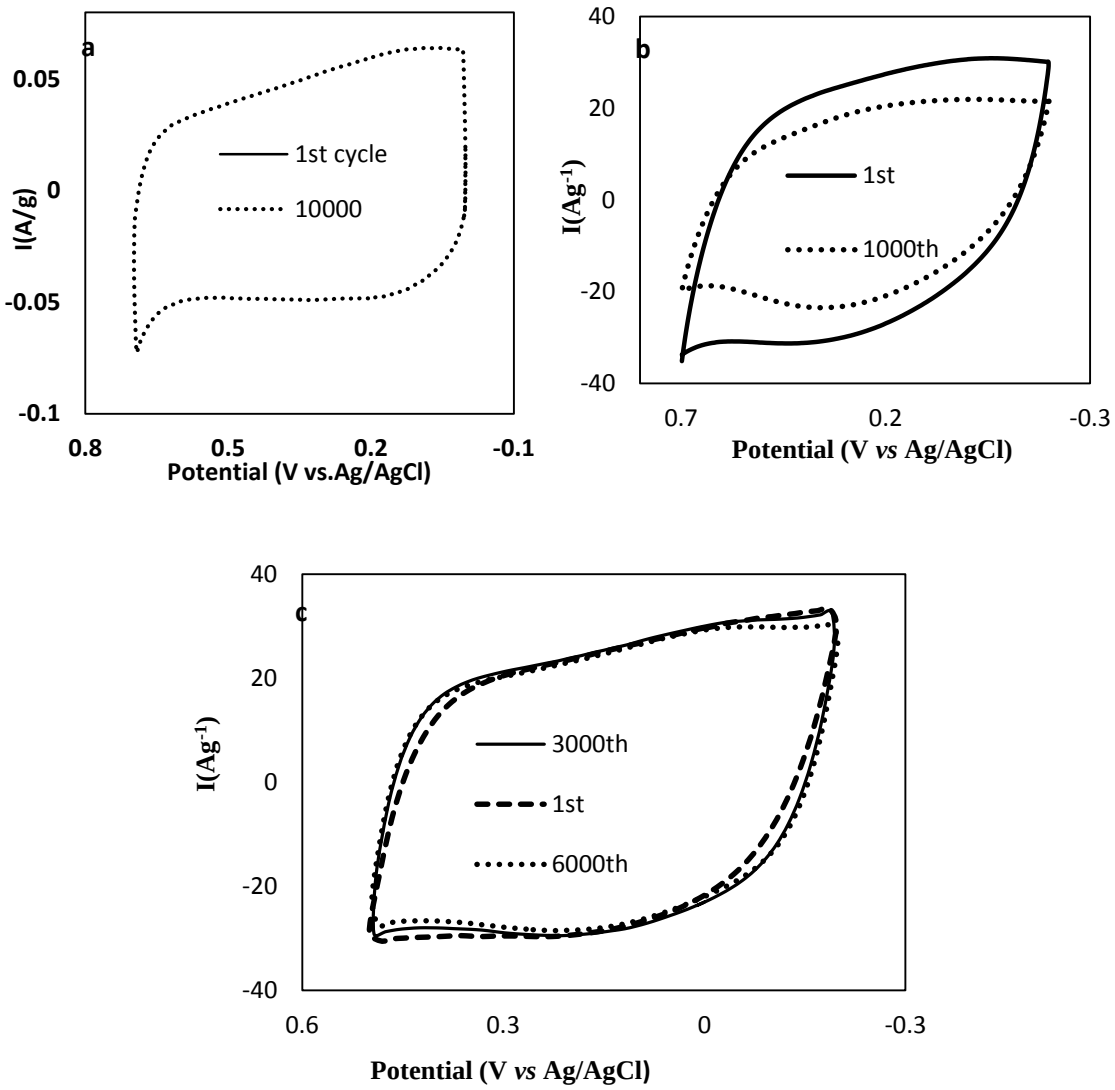

Fig 5.9 CV curves of the GF, PPY and PPY-GF1 after thousands of cycles in 0.5M KCl at a scan rate of 100 mV s^{-1}.

We further investigated the stability of the electrodes by performing galvanic charge-discharge tests and the results were consistence with the CV findings. Our results show that after few hundreds of charge-discharge cycles the polymer exhibited

significant ohmic drops and became resistive. Thus the poor mechanical integrity of the PPY makes it unsuitable for long term uses.

In order to gain a better insight into the electrode structure and its relation to the electrochemical performance, the electrode materials were further characterised again using SEM after completely being air-dried after the electrochemical tests (without rising them with water or cleaning them). Fig 5.10 shows SEM images of the GF after 10,000 and the PPY-GF1 after 6,000 cycles of CV test. As shown in Fig 5.10, the post-tested GF and PPY-GF1 retained the same interconnected 3D structure and good integrity, almost identical to those before going through any electrochemical characterisations.

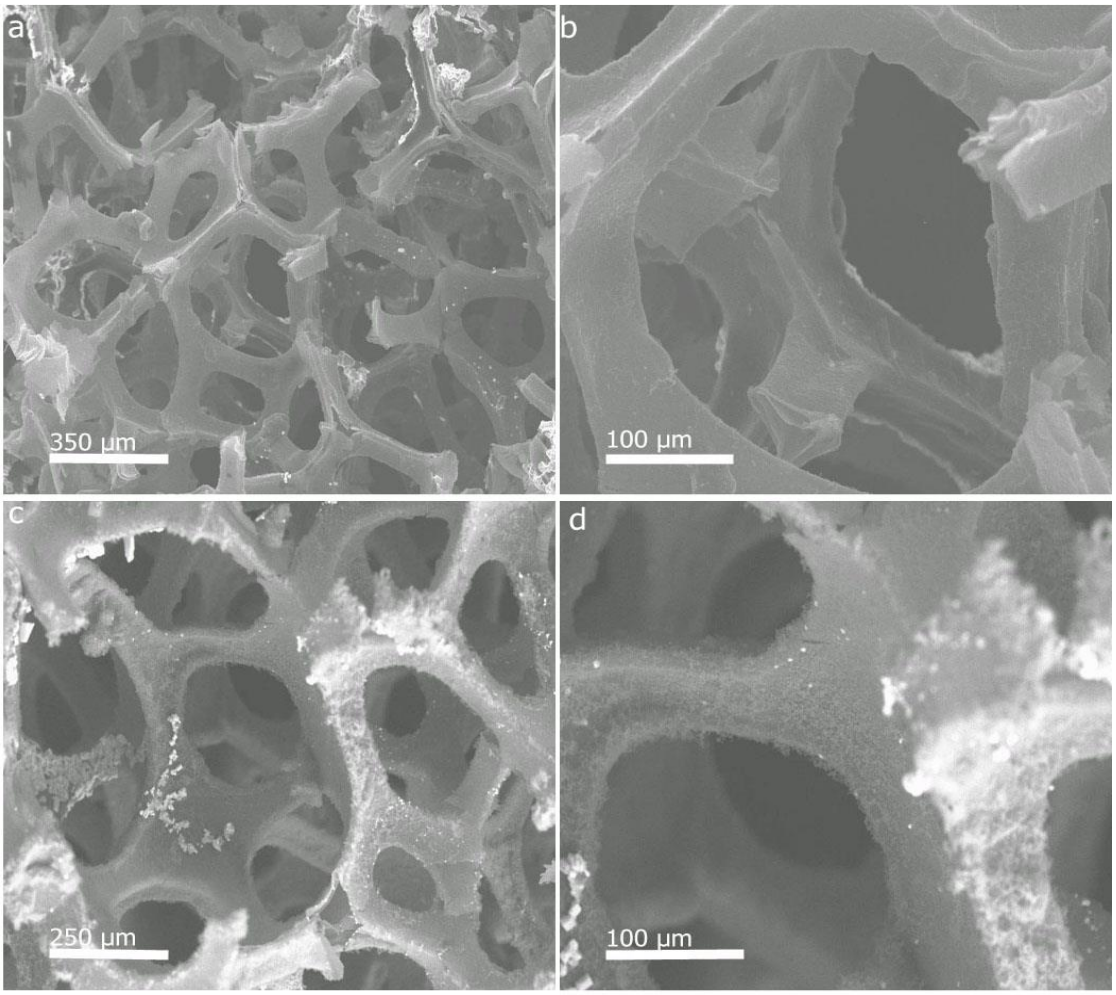

Fig 5.10 SEM images of the GF after 10000 cycles of CV test, and (c, d) SEM images of PPY-GF1 after 6000 cycles of CV test.

In the case of the composite electrode, Figs 5.10c-d, the PPY chains are still closely attached to the GF scaffold after all those cycles, revealing a strong interaction between the GF and the PPY. White spots on the image are electrolyte ions as evidenced by the EDS during the SEM. The above results indicate clearly the excellent mechanical integrity of the produced 3D materials. These results further verified the successful role of the GF as a holder and stabilizer for the PPY coating in the high performance electrode composites.

In fact, the density of the foam plays a fundamental role in the flexibility of the GFs. Our experiments showed that a foam with a high bulk density of 10 mg cm^{-3} had a lower cycle life, corresponding to a lower mechanical strength, than the GFs with a density value of 3 mg cm^{-3}. At lower density the foam benefits from more pores which absorbed the mechanical stresses caused during the ion intercalation-extraction process, hence contributing positively to the cycle stability of the electrode.

5.2.2.5 Electrolyte effect

The effect of electrolyte on the electrochemical activity of the PPY-GF electrode was assessed using the A.C impedance technique. Fig 5.11 shows the Nyquist plot of the PPY-GF1 in: (a) 0.5 M H_2SO_4 and (b) 0.5 M KCl, recorded in the same frequency range of 100 kHz to 0.1 Hz.

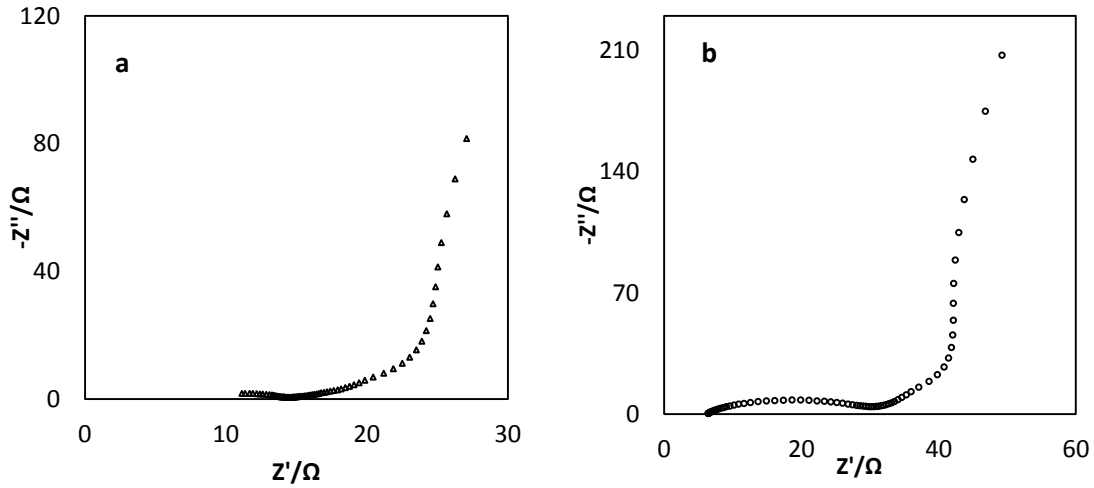

Fig 5.11 Nyquist plots of the PPY-GF1 electrode: (a) in 0.5 M H_2SO_4, and (b) in 0.5 M KCl.

Obviously, the impedance values in Fig 5.11a are lower than those in Fig 5.11b. The value of the Rct in the case of H_2SO_4 electrolyte is 8 Ω ohm, against 15 Ω in the KCl electrolyte. Further, the associated impedance with the onset of the capacitive behaviour of the electrode in H_2SO_4 electrolyte is much lower than that in KCl

electrolyte. This improved response is due to the better conductivity of the H_2SO_4 over the KCl.

In addition to the electrolyte type, the concentration of the electrolyte also plays an important role in the kinetic rate of the electrochemical process. Increasing the electrolyte concentration enhances the electrolyte accessibility and facilitates diffusion process. However one should avoid using high concentration electrolytes as mass transfer resistance is likely to happen at high concentrations of the electrolyte [252].

5.3 Structural and electrochemical characterisation of the PPY-GF2 composite: Effects of the time deposition

As shown in Table 5.1, PPY-GF2 was synthesised by chemical polymerisation of the pyrrole for 3 h (against PPY-GF1 for 15 h). The formed thickness of the PPY coating on the GF template was much thinner than that in the PPY-GF1 and in fact, no noticeable coating was observed. The TGA analysis however showed that the composite contained 18% PPY (35% in the PPY-GF1) revealing a successful graphene functionalization with the PPY. Fig 5.12 shows briefly the results associated with this type of electrode, including the morphology of the composite, and the CV curve and the Nyquist plot.

The SEM images of PPY-GF2 exhibit an interconnected porous 3D structure that is similar to the PPY-GF1. However as the PPY content in the former is low, PPY coatings are not observable with low magnification SEM image. Compared with pure GF (Fig 5.3a), the SEM results do not show big morphological difference, however their electrochemical performance (Fig 5.12b vs Fig 5.6a)

is quite different, as PPY-GF2 exhibits much higher electrochemical performance and specific capacitance than GF as it is pseudocapacitive materials.

Compared with PY-GF1, PPY-GF2 electrode exhibits lower specific capacitance, 170 F g^{-1}, as the latter possesses lower PPY content in the composite. However, as both electrodes were built on the strong GF backbone, the PPY-GF2 electrode also showed excellent cycle stability, Fig 5.12d, and no current loss was observed after 500 cycles of CV.

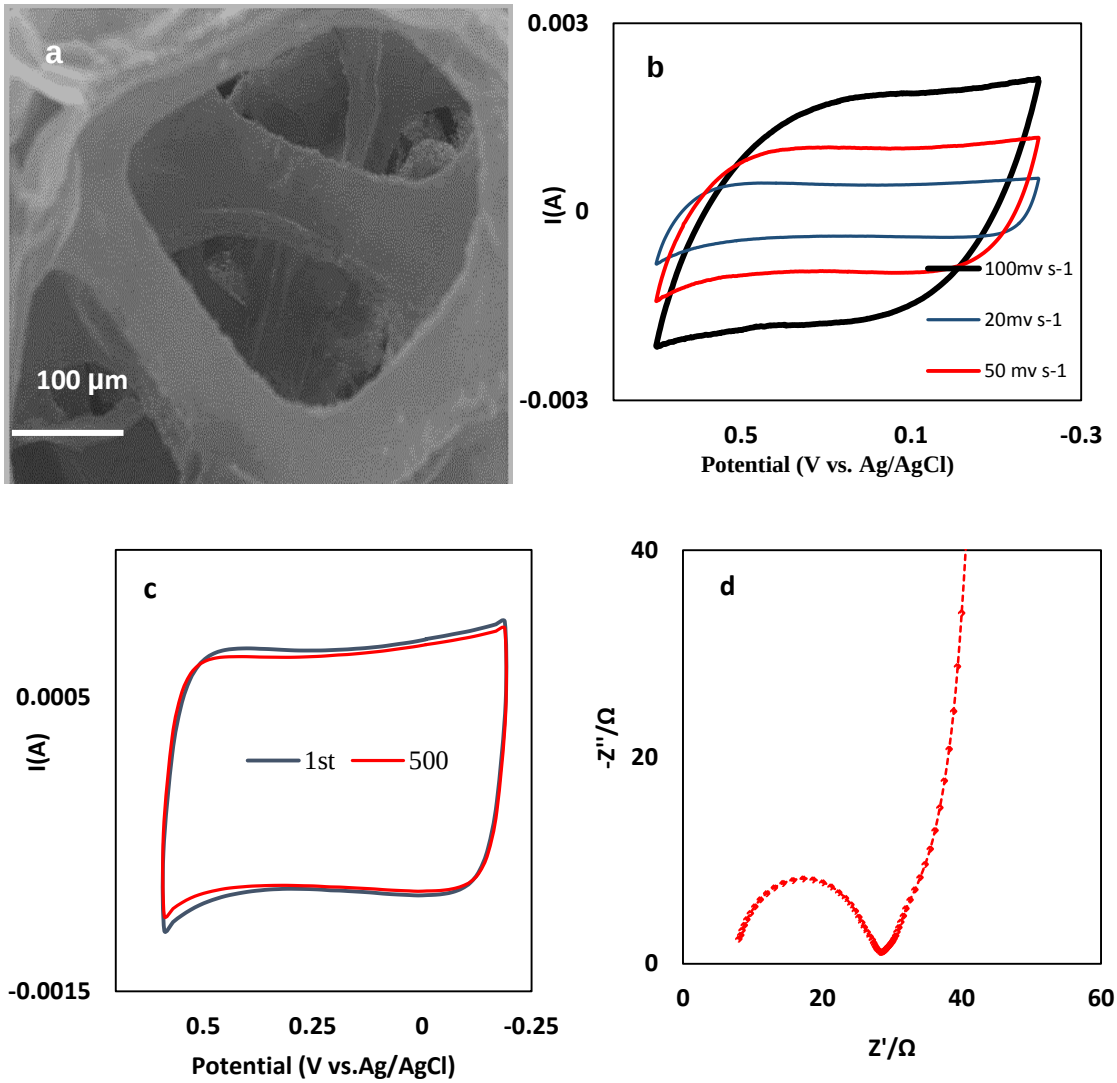

Fig 5.12 The morphology and electrochemistry characterisation of the PPY-GF2 electrode; (a) SEM image, (b) the CV curve, (c) the Nyquist plot at OCP, and (d) CV curves showing the cycle stability at a scan rate of 50 mVs^{-1}.

The Nyquist plot of the electrode, Fig 5.12d, shows a highly sloped straight line at low frequency, and an arc-shaped impedance at high frequency, which is the typical behaviour of pseudocapacitive materials. Phase degree of this electrode is 80° at low frequencies, revealing a capacitive behaviour at that region.

It is worth noting that as both CV results and Impedance showed, PPY-GF2 exhibits more capacitive behaviour than PPY-GF1. It showed lower specific capacitance and faster ion diffusion process. This behaviour is due to the different GF/PPY weight ratio in the two electrodes and thus different contribution of each storage mode.

5.3.4 Effects of the synthesis method

To further investigate the effects of the synthesis method, the electrochemically deposited composites, PPY-GF3, were assessed and benchmarked against the chemically deposited samples. The PPY content in PPY-GF3 is *ca.* 30% after 200 s deposition, similar to PPY-GF1. The electrochemical results are shown in Fig 5.13.

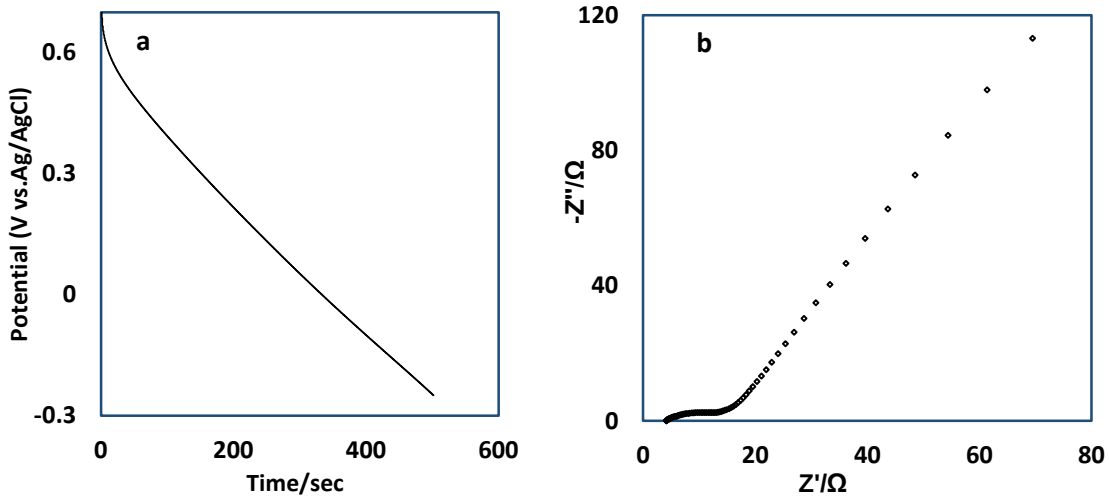

Fig 5.13 (a) Galvanostatic charge-discharge curve of PPY-GF3 at 1 Ag^{-1}, (b) the Nyquist plot at OCP of PPY-GF3.

Based on the galvanostatic discharge curve presented in Fig 5.13a and equation (5.3), a value of 560 Fg^{-1} (at 1 Ag^{-1}) was obtained as the specific

capacitance of the PPY-GF3. This is a very good performance, comparable with 570 Fg^{-1} obtained for PPY-GF1. From the Nyquist plot in Fig 5.13b, we obtained a value of 3 Ω as the series resistance of the electrode, which is even lower than that of PPY-GF1 electrode, meaning that this electrode is as efficient as the chemically prepared electrodes because it benefits from the same ideal 3D architecture discussed earlier.

The above electrochemical data and findings show clearly that both chemical and electrochemical synthesis can be used for preparing 3D PPY-GF composite, and the synthesis method itself does not affect the performance of the electrode.

5.4 3D PANI-GF electrode: Effect of the electrode materials

To demonstrate the applicability of the present approach for other materials, we further prepared 3D PANI-GF composite electrodes, by adopting the same strategy. Aniline polymerisation and measurement were performed in H_2SO_4 electrolyte as it is known that PANI is electrochemically active in acidic medium [253]. The PANI-GF electrodes were prepared electrochemically from 0.1 M aniline/0.5 MH_2SO_4 solution using the Chronoamprometry technique.

The CV results of the PANI-GF electrode is presented in Fig 5.14a. As shown, this electrode exhibit much higher current values than those of GF and thus higher specific capacitance, revealing the successful interaction between PANI and GF. Fig 5.14b shows the Nyquist curve of the electrode. The plot consists of three parts: series resistance of about 12 Ω, charge transfer resistance of 20 Ω, and diffusion resistance

at low frequencies. At low frequency the phase degree of the electrode reaches to 55 degree.

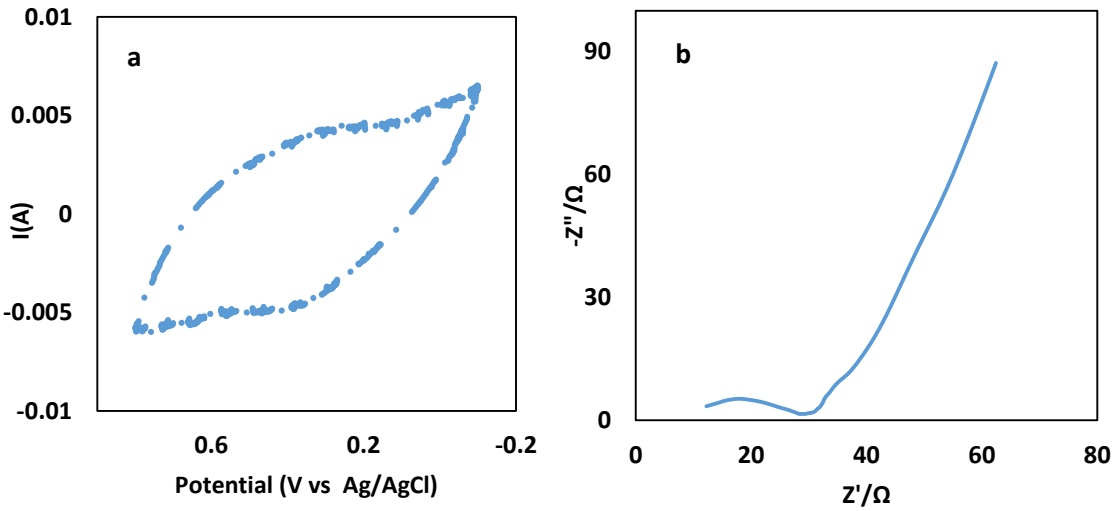

Fig 5.14 (a) CV curve of PANI-GF at scan rate of 100 m V s^{-1}, and (b) Nyquist plot of PANI-GF in 0.5 M H_2SO_4 and frequency range of 100 K Hz- 100 m Hz.

This good performance of the electrode is due to the pseudocapacitive nature of the PANI and more importantly the efficient 3D structure of the composite which allows for highly efficient charge storage process. During charge-discharge cycles, sulphate ions intercalate and de-intercalate repeatedly from the PANI chains. Fig 5.15 shows a schematic of the associated reactions.

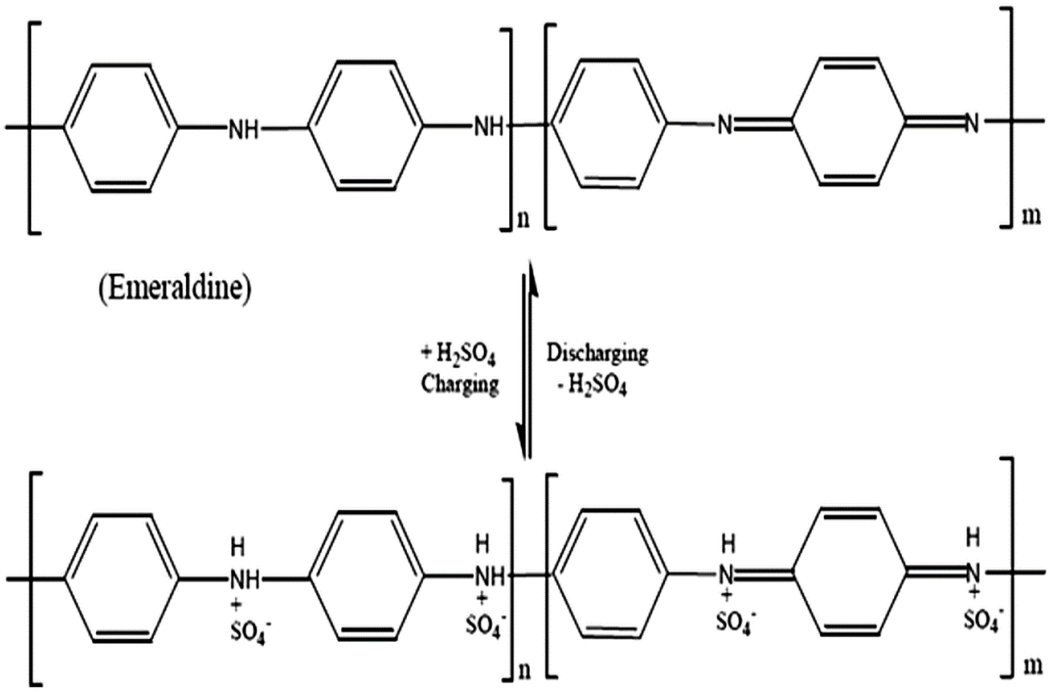

Fig 5.15 Schematic of the charge-discharge process in PANI [254].

The stability of the electrode was investigated by performing galvanostatic charge-discharge and CV tests for a long time. Both tests confirmed the good stability of the synthesised PANI-GF electrodes, after thousands of charge-discharge cycles.

5.5 Summary

Highly flexible, binder-free, and hierarchically regulated GF-based 3D electrode structures with excellent cycle life and enhanced pseudocapacitive performance were reported in this chapter. The synthesised 3D GF-CPs composites are free standing and thus were used directly as working electrode without using any binder or carbon additives.

The unique features of the PPY-GF composites such as 3D GF scaffold and high conductivity of p-doped PPY, afforded the PPY-GF electrodes with enhanced

pseudocapacitive properties. The PPY-GF composite exhibited a remarkably high capacity of 660 Fg^{-1} with excellent capacity retention of 100% after 6,000 cycles, against a *ca*. 30% initial capacity loss after only 1,000 cycles for the pure PPY. Compared with many recent reports on PPY-carbon composite electrodes, this result displays one of the highest capacitance values. The significantly improved properties are related mainly to the high flexibility, low density, hierarchical structure of the GFs, the redox properties of the PPY, and finally the well-connected 3D core-shell structure of the PPY-GF electrodes.

We have found out that the density of the GF plays important role in the cycle life of the electrodes. At a higher density (e.g. 10 mg cm^{-3}), the foams possesses a lower porosity level and becomes more rigid with less flexibility, thus failing to survive the repeated charge-discharge cycle which accompanied constant dimensional (volume) changes.

We improved the stability of the composites significantly by using lightweight GFs as scaffold. In the case of PPY, most of the materials dropped into the electrolyte or around the working electrode during the test, while no structural change was noticed for the PPY-GF electrodes due to the good interface connection between the PPY and graphene. In fact, the excellent cycle life of the composites further confirmed the good interaction between the PPY and GF.

Another key parameter which affects positively the stability of the electrode and also its high capacitance is the binder free feature of the synthesised electrodes. Eliminating binder from the electrodes can effectively assist in reducing mechanical stresses of the electroactive materials during ion intercalation and de-intercalation and can also help in reducing the electrical resistance of the electrode.

The effects of synthesis conditions such preparation method and deposition time were also investigated. Similar to the PPY-GF, the fabricated PANI-GF was free-standing 3D electrode AND thus used directly as working electrode. The result were further emphasised that the GF played a more important role than the polymer (PPY or PANI) for the improved performance.

Indeed, polymer deposition on the 3D GF substrate resulted in a more uniform coating of the PPY on the GF (rather than highly agglomerated structure) which affects positively the electrode's conductivity and its electrochemical capacitance.

Finally, given the binder-free, lack of necessity for additional current collector, as well as the versatile shape configuration, this 3D electrode architecture is very promising for flexible and lightweight energy storage application.

Chapter 6 : From graphene to silicon carbide

6.1 Introduction

Owing to the unique properties of silicon carbide (SiC) material such as its wide-band gap (2.4-3.26 eV)[255], high hardness, high thermal conductivity and excellent resistance to erosion and corrosion, SiC has always been the material of choice for a wide range of applications [256,120]. Its capability of being doped both n- and p-type results in the intensive development for its use in high power, high frequencies and high temperature electronic devices [123-126,257].

Comparing graphene with graphite, we can now easily ascribe its advantages over graphite, in terms of mechanic, electronic and thermal properties, to the lower dimensional system, the free π electron and high quality structure of the graphene [258]. Not only graphene, but all other new 2D materials show excellent properties over their 3D analogues. Thus, it is expected that by playing with the dimensionality and shifting from highly stacked 3D SiC to ultra-thin few layers SiC, and then optimistically to single layer SiC could lead us to new SiC structures with amazing and unexplored mechanical, electrical and optical properties. This chapter describes a successful approach for the simultaneous production of 1D, 2D and 3D SiC structures and their characterisations.

6.2 The synthesis of the SiC foam

In this research the SiC foams were fabricated by a carbothermal reduction of SiO with graphene foam (GF), as shown in Fig 6.1. All SiC foams were prepared at 1550 °C, unless otherwise specified. The heating rate from room temperature to 1000 °C was 10 °C/min, and that from 1000 °C to 1500 °C was 4.5 °C/min.

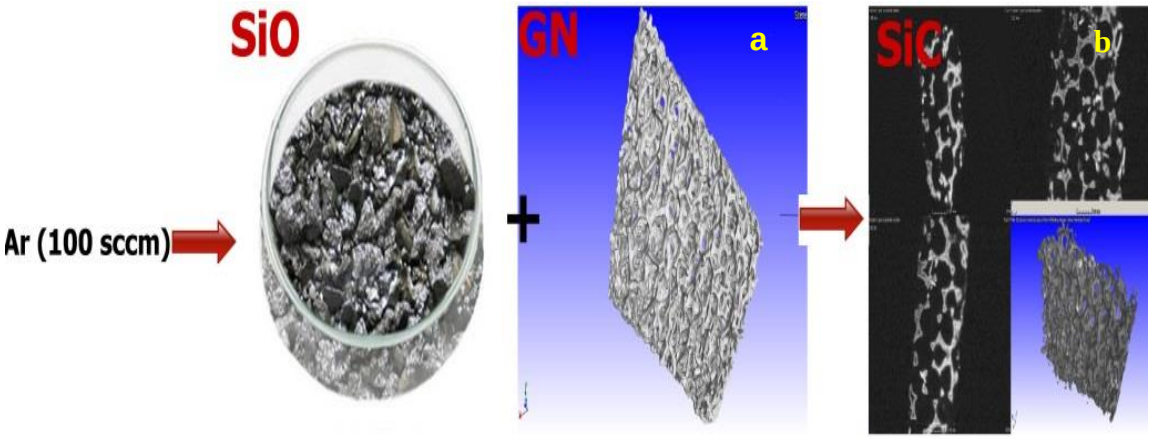

Fig 6.1 Schematic for the preparation of the SiC. (a) SEM image of GF and (b) micro-ct image of 3D SiC.

The above schematic depicts the template growth for the SiC fabrication. As shown, the 3D versatile-shaped GF was converted to a SiC foam without any change in dimensions. Thus, macroscopically the produced SiC foam retained the same shape and appearance of the GF. Most of the produced foams have an average length of 15 mm, width of 15 mm and thickness value of 2 mm, which are identical to the original GF template.

We produced SiC foam with density range of 10 -20 mg cm^{-3} by using GF templates with ρ range of 3-10 mg cm^{-3}. By using GF with different shapes and porosity levels, one can precisely engineer the shape and dimensions of the SiC foam. Apart from the

main mentioned dimensions, we also created cylinder, rectangle, and various irregular shapes of SiC foam with volume varying from 50-450 mm^3.

During the synthesis, as shown in Fig 6.1, firstly, the SiO vapour formed at high temperature travelled downstream to reach the GF, and then reacted with active carbon atoms, to form SiC nucleus. Those nuclei resulted in the formation of different SiC structures. Depending on the reactivity of C atoms on the GF surface, which depends on defects such as holes, edges and the fractured C=C bonds [259], or other imperfection sites, SiC may grow on-site the GF template surface, or it may grow out of the surface along the energetically preferred crystal growth direction [260].

6.3 Structural characterisation of the SiC foam

Fig 6.2a shows an SEM image of the SiC foam prepared at 1380 °C. Apparently, the as-produced foam has the same dimensions as the GF template. However, it does not have the smooth or soft structure as does the GF, rather it exhibits a rough and hard structure.

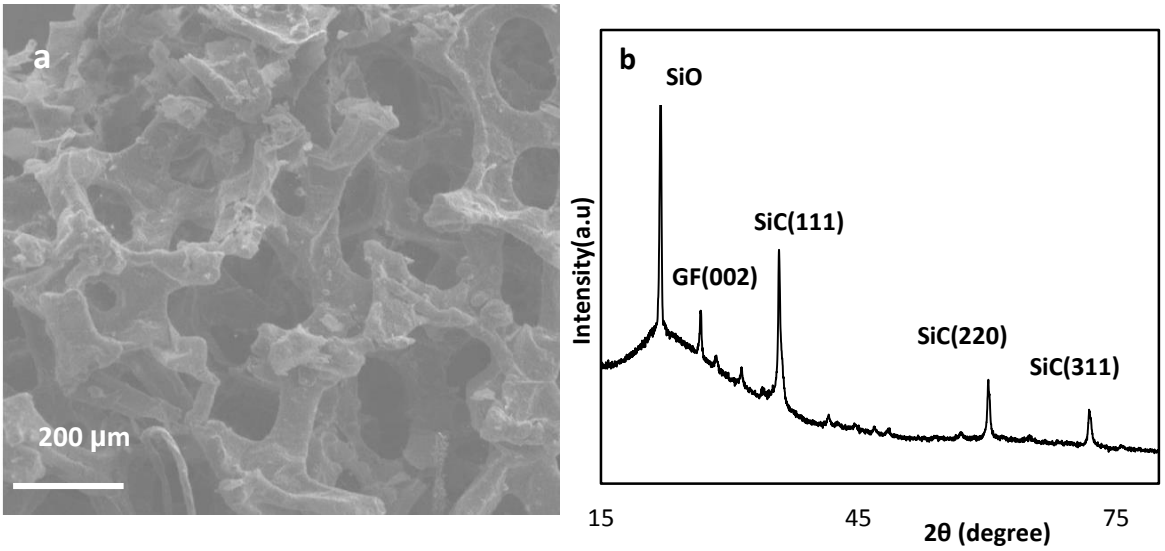

Fig 6.2 SEM image and XRD profile of SiC sample prepared at 1380 °C.

The structural feature of the synthesised SiC was characterised by XRD technique and the results are presented in Fig 6.2b. As verified in the XRD pattern, in addition to the SiC, the resulting foam contains residues of graphene and SiO too. The non-reacted SiO materials give the foam a rough, dull and non-uniform appearance.

Fig 6.3 shows TEM images of SiC samples prepared at 1380 °C. Under TEM, we observed flake-like structures, 1D SiC nanowires and some irregular shapes. The EDS analysis of all samples showed a high content of oxygen in most samples. Fig 6.3a shows an amorphous SiO shell around the crystallised SiC structures. These results show that even though at this low temperature, SiC was formed, as shown in both the XRD and TEM results. It is not pure and in order to improve the quality of the product, we either need to etch the produced SiC with HF or modify the synthesis parameters such as the temperature or reaction time.

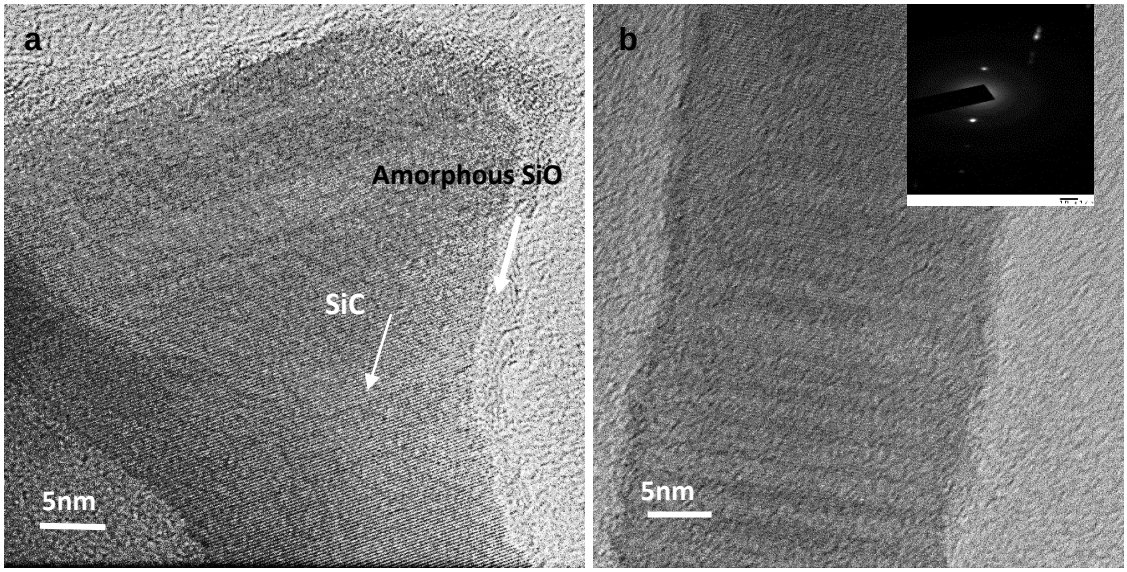

Fig 6.3 TEM images of SiC samples prepared at 1380 °C. HRTEM of (a) SiC flakes and (b) SiC nanowires.

Upon the removal of free carbon through burning at 680-700 °C, the SiO_x (x = 1 or 2) residue and other possible residue can be removed by HF etching, to obtain pure 3D SiC materials. Fig 6.4 shows XRD profile of a SiC foam before (a) and after (b) HF etching. This sample was prepared at 1400 °C. The SiO peak at about 21 degrees has weakened and broadened considerably after the HF etching. As pointed out earlier, HF etching is very useful for removing SiOx residues, but it is not efficient for carbon removal. The latter should be eliminated via the oxidation process first at 600-700 °C, prior to HF etching.

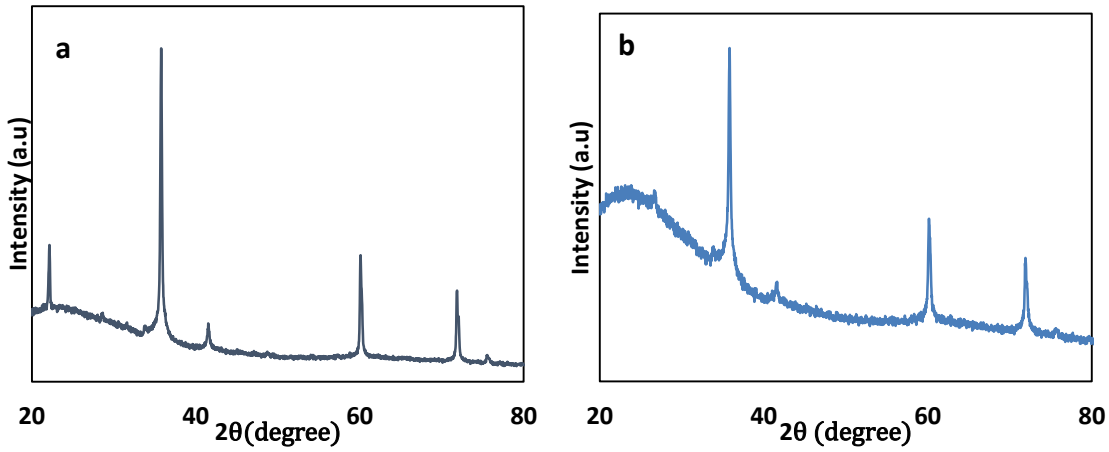

Fig 6.4 XRD profiles of a characterised SiC sample before (a) and after (b) etching.

The above structural results from SiC foams prepared at about 1400 °C suggested that these temperature are not high enough for a complete carbothermal reaction between SiO and GF. After these initial results, the growth temperature was then increased to 1550 °C, to yield better quality SiC product. All the following results correspond to samples prepared at 1550 °C.

Fig 6.5 shows the SEM micrographs, µ-CT image, and XRD pattern of the resulting SiC foam. Fig 6.5a is an SEM image of the GF template demonstrating clearly the interconnected network feature of the GF. As shown in Fig 6.5b-d, the synthesised SiC foam mimics the same 3D structures from the carbon source, remained the key features of a highly porous interconnected network.

High magnification SEM images presented in Figs 6.5 d-e show that there are many nanowires growing from the internal wall and truss surfaces, with lengths varying from a few hundred nanometres to millimetres. The nanowires appear to be highly flexible, exhibiting various diameters. We observed that as the content of nanowire increased, the entire foam become more flexible due to the high flexibility feature of the

nanowires. Fig 6.5d reveals that the SiC nanowires grow from random facets of the 3D scaffold, indicating that the defect sites in the GF template may be the main starting point for the nanowire growth [261].

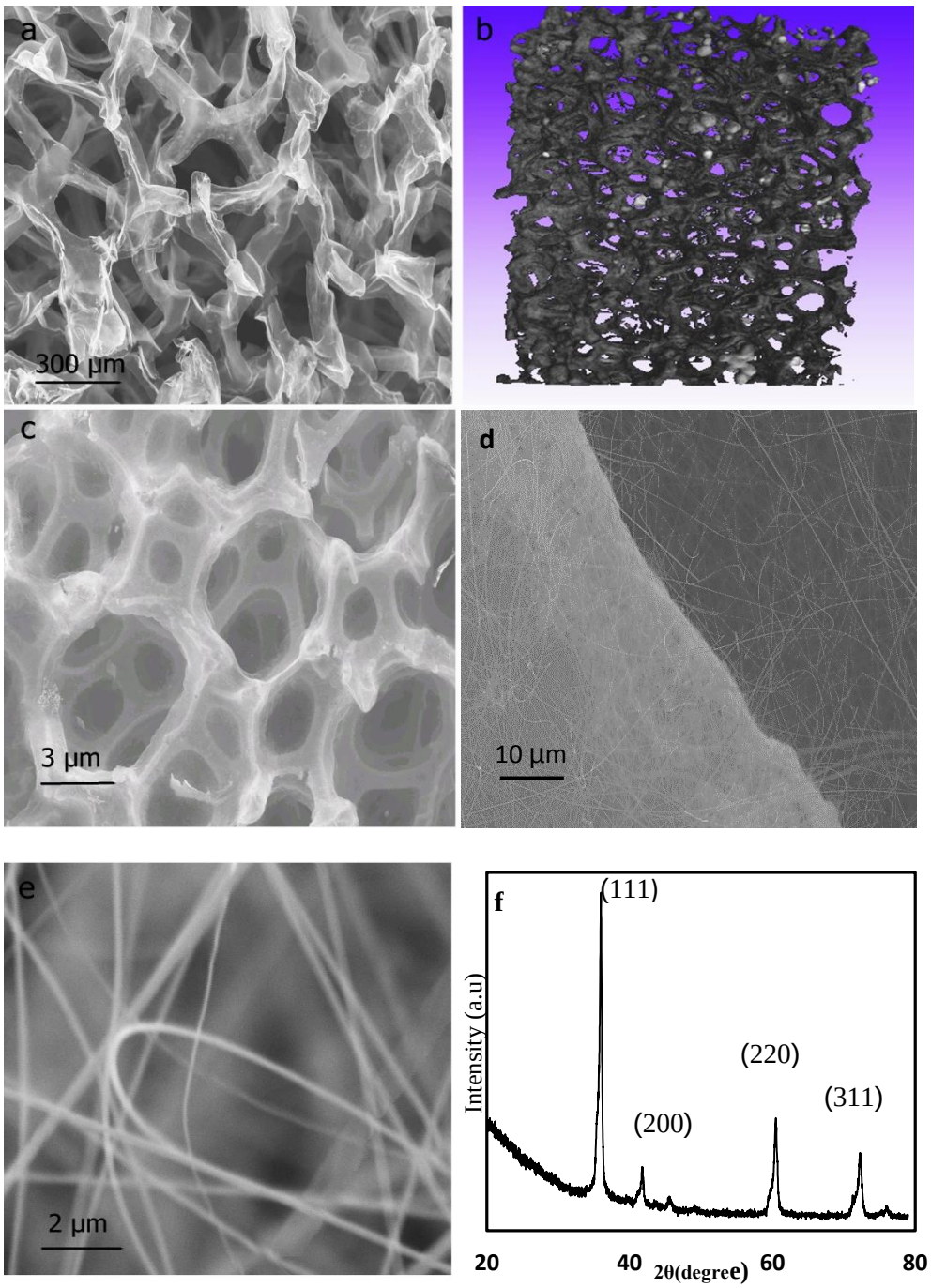

Fig 6.5 Morphological and structural characterisations of the foam. (a) SEM image of the GF, (b) Micro-CT image of the SiC foam, (c) SEM image of the SiC foam, (d, e) High magnification SEM images of the SiC foam, and (f) XRD profile of the SiC foam.

The composition of the entire 3D SiC foams was characterised by EDX during SEM observation.. As shown in Fig 6.6, only C and Si were detected, confirming the dominant SiC nature of the foam. Some other foams showed a little amount (4-10%) of oxygen too, which could be either related to the unreacted SiO or oxidises sites in the sample, presumably exists on the surface.

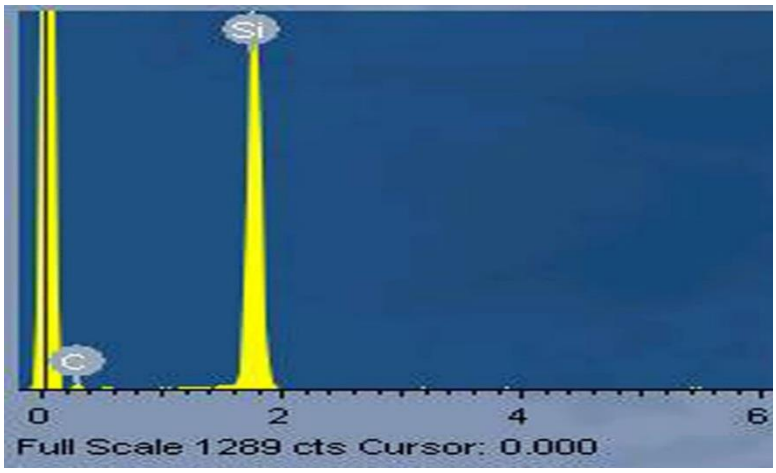

Fig.6.6 EDS spectrum of the 3D SiC foam.

We further used X-ray diffraction to analyse the crystalline structures of the foam. As shown in Fig 6.5f, there is no detectable peak for the GF at 26 and 54 degrees or for the SiO_x (x = 1 or 2) at about 22 degrees, and all peaks are corresponding to SiC, confirming the successful carbothermal conversion from the GF to SiC at 1550 °C. The main SiC peaks in the XRD pattern can easily be indexed to the cubic structure of the SiC (JCPDS Card No. 29-1129). The weak peak at 33.6, 38.2 and 49.7 degrees correspond to α-SiC (JCPDS card No. 29-1126) [262].

Fig 6.7 shows the Raman spectrum of the 3D SiC. The spectrum showed an intense peak at about 791 cm^{-1}, which belongs to a transverse optical (TO) mode of the E1 phonon. Two other peaks at about 763 and 945 cm^{-1} are attributed to the TO and LO (longitudinal optical) modes of E1 and A1 phonons respectively which are consistent

with the standard Raman shifts of SiC [263]. Further, the face that there are 3 active Raman bands, instead of 2, reveals that the sample is not pure cubic phase, rather it is a mixture of both hexagonal and cubic phases because only α-SiC shows two TO modes [264].

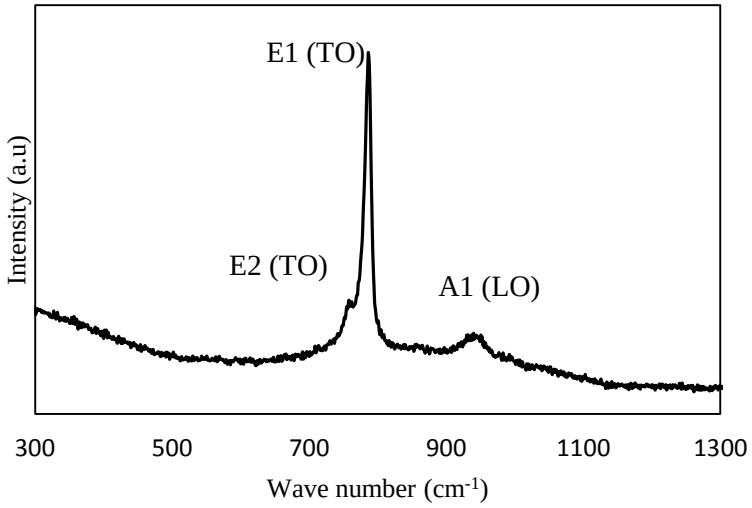

Fig.6.7 Raman spectrum of the 3D SiC foam.

The thermal behaviour of the SiC foam was investigated using a TGA technique, and the related graph is shown in Fig 6.8a. First, there is a weight loss at T < 200 °C, due to the absorbed water evaporation. After that, there is almost no weight change until 900 ºC from which the weight increases sharply, due to the passive oxidation of SiC and the formation of SiO_2 which was verified by the XRD measurement (Fig. 6.8b) of the white residuals after the TGA. The relatively flattened profile up to 800 °C in Fig 6.8a also provides evidence that the SiC foam obtained under this set of parameters was of high quality, with little or no GF residues, otherwise weight loss should be detected.

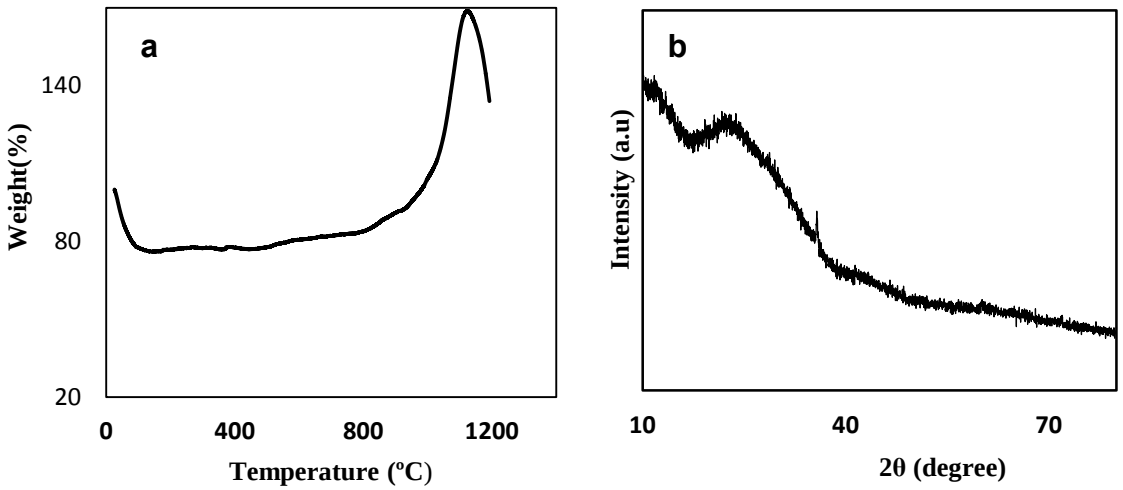

Fig 6.8 Thermal properties of the SiC foam. (a) TGA profile of the SiC sample in air and (b) XRD profile of the sample after TGA experiment.

To gain more insight into the nanostructures of the produced SiC, the foams were further characterised by TEM, and the images are shown in Fig 6.9. The findings consistently show that the SiC foam consists mainly of 2D SiC nanoflakes and 1D SiC nanowires.

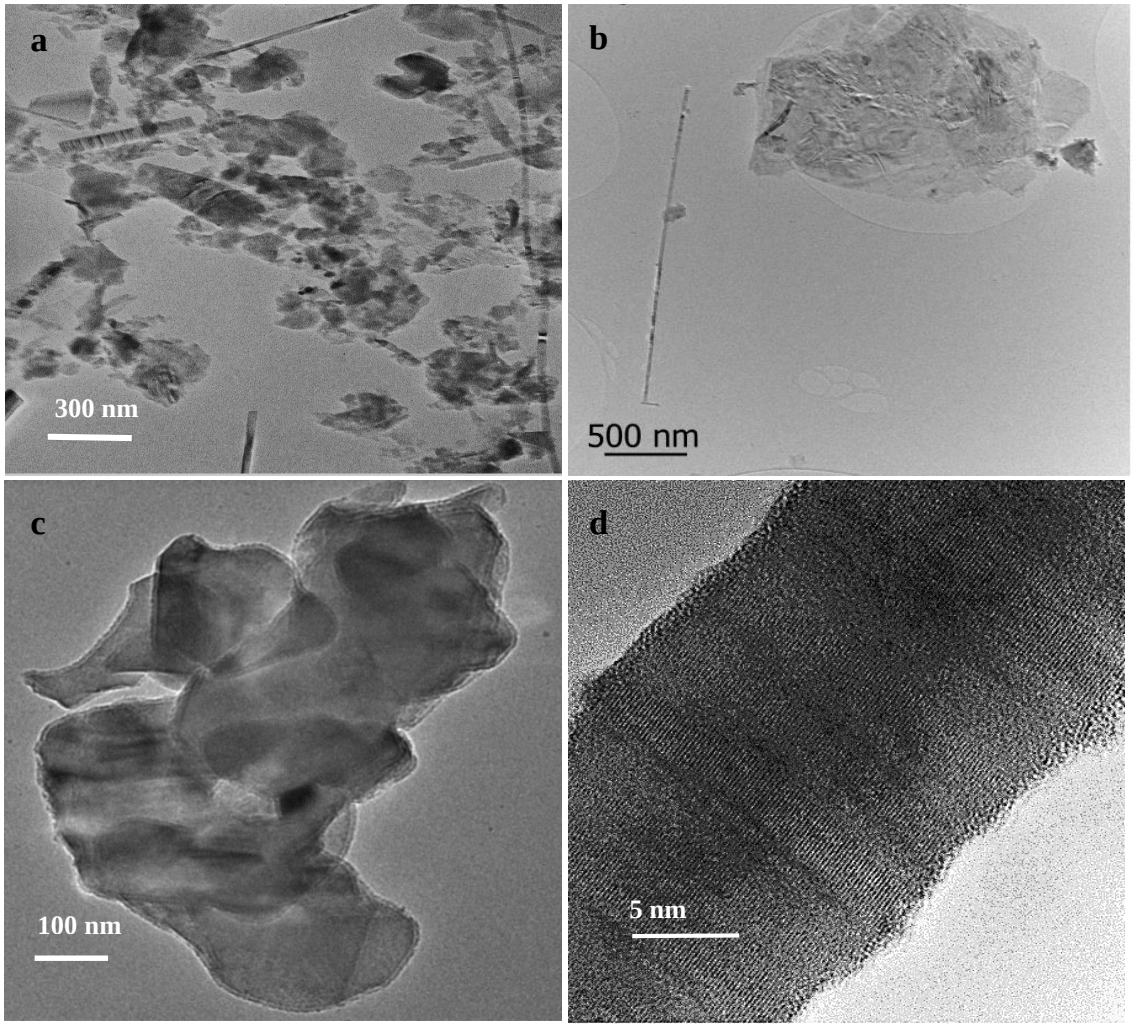

Fig 6.9 TEM images of the SiC. (a, b) Low magnification TEM images showing the 2D SiC sheets and 1D SiC nanowires (c) TEM image of 2D SiC flakes and (d) HRTEM image of a SiC nanowire.

The nanoflakes shown in Fig 6.9a-c are a class of completely novel structures, and they are the key backbone components in the 3D foams. These 2D structures will be discussed in detail in the next part. Fig 6.9d shows a high resolution TEM image of a 1D nanowire with a diameter value of 25 nm. It is a well-crystallised cubic structure, with regular interlayer spacing of 0.252 nm which corresponds to the visible lattice fringes of the (111) plane.

Fig 6.10 shows SEM and TEM images of two SiC nanowires. In Fig 6.10, an high resolution SEM image shows clearly the different diameter varying from 20 nm to 100

nm. Fig 6.10b shows an HRTEM of a periodically twinned SiC nanowire. Obviously the twin boundaries defects, gives zig-zag type appearance to the SiC nanowire. Therefore, not only the diameter and the size of the SiC nanowires vary, but also the defect level varies significantly from one nanowire to another.

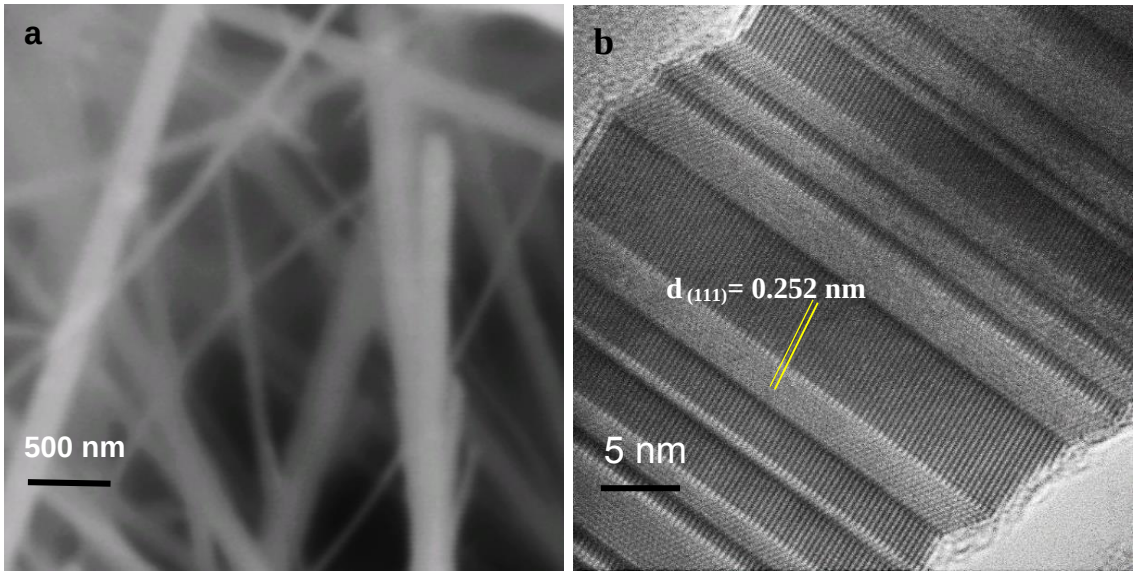

Fig 6.10 High resolution SEM and TEM images. (a) SEM image of SiC nanowires and (b) HRTEM image showing mainly twinned nanostructure of an individual SiC nanowire.

The introduction of stacking faults (SFs) into the system can be explained in terms of both the growth kinetic and thermodynamic. It was discussed that the stacking fault density increased with increases in the reaction rate (due to parameters such as increased heating rate). A relatively slow reaction allows atoms to diffuse a long distance to form an equilibrium, defect less structure[265].

From the thermodynamic point of view, the low energy required for the SF formation is another important factor that energetically favours the nanowire growth, as the entire system becomes more stable when defects such as twins or SFs presented in the system [266,267].

6.4 Growth mechanism of SiC

As described in the previous part, the as-produced 3D SiC foam consists of two main structures: 1D SiC nanowires with various structural features and SiC flakes. The polytype of these nanostructures and also their physical apparent [268], straight or curved [269], and dimensions [130], depends directly on the growth mechanism. Here we believe that the solid-vapour mechanism controls the SiC growth.

Chemically, the conversion from GF to SiC foam follows the following reactions:

$$SiO + 2GF \rightarrow SiC + CO \quad (6.1)$$

$$SiO + 3CO \rightarrow SiC + 2CO_2 \quad (6.2)$$

Since the synthesis is a catalyst free process, and the precursors are not mixed, rather they are physically separated, thus vapour-liquid-solid (VLS) mechanism is not an option here. It is more likely that the SiC growth occurs dominantly via the solid-vapour (V-S) mechanism, although vapour-vapour reaction is also likely to occur between vapour phases [259,270,271].

By adopting the catalyst-free synthesis procedure, we avoided the catalyst contamination in the final product [272]. In fact, since the process is catalyst-free, the reactivity of carbon atoms in the GF and literally the defect sites of the GF such as the edges play a critical role in the formation of the SiC nanostructures [273]. The resulting SiC flakes and nanowires, as well as their structural features, are a direct result of the lowest activation energy along the growth direction, thus achieving the preference of specific structures over the other at specific temperatures or positions of the foam.

The conversion from the graphene foam to SiC foam, and from graphene flake to SiC flakes, looks similar to the reported direct conversion from CNT to SiC nanowires and nanorodes [273-276], known as CNT-confined reactions. These earlier studies reported the production of SiC nanowires and other semiconductor (such as gallium nitride [277]) with diameters similar to or larger than the CNT template, by adopting the carbothermal reduction technique. In this thesis, we believe that the graphene flakes in the GF template are the main reason behind the formation of the SiC flakes. Although we do not have enough data to draw a full conclusion, it is likely that during the carbothermal reduction graphene flakes converted directly to the SiC flakes, because of the dimensional similarities between both flakes.

6.5 Structural characterisations of the 2D SiC

As earlier TEM images showed, the as-synthesised 3D SiC was built upon two components: 1D nanowires and 2D flakes. Thus, it is highly beneficial to develop a technique to separate them and then carry out further investigation to understand them.

To achieve 2D SiC nanoflakes, a precisely controlled sonication is a key step. After separating SiC nanoflakes from the nanowires, the new SiC nanoflakes were carefully characterized by a variety of techniques. Fig 6.11 shows the morphological features of the 2D SiC from microscopy observations, after the SiC suspension being dropped onto a glass slide or a Si wafer. Although the optical microscopy and low magnification SEM images (Fig 6.11a) show the irregular platelets lying almost flat on the substrate, higher magnification images (Fig. 6.11c) and TEM observations reveal small folding in

most of the SiC flakes. Upon breaking off the 3D SiC foam, the newly separated SiC sheets are likely to stabilise themselves inevitably and relax via slight folding at the edges. This folding phenomenon has been reported for many thin films and it can be a spontaneous behaviour due to the separation from the substrate, or it may be a response to a particular stimuli [278]. A study on hexagonal nanoribbons proposed that this type of curvature could minimize the edge asymmetry and the structural stress along the edge [158].

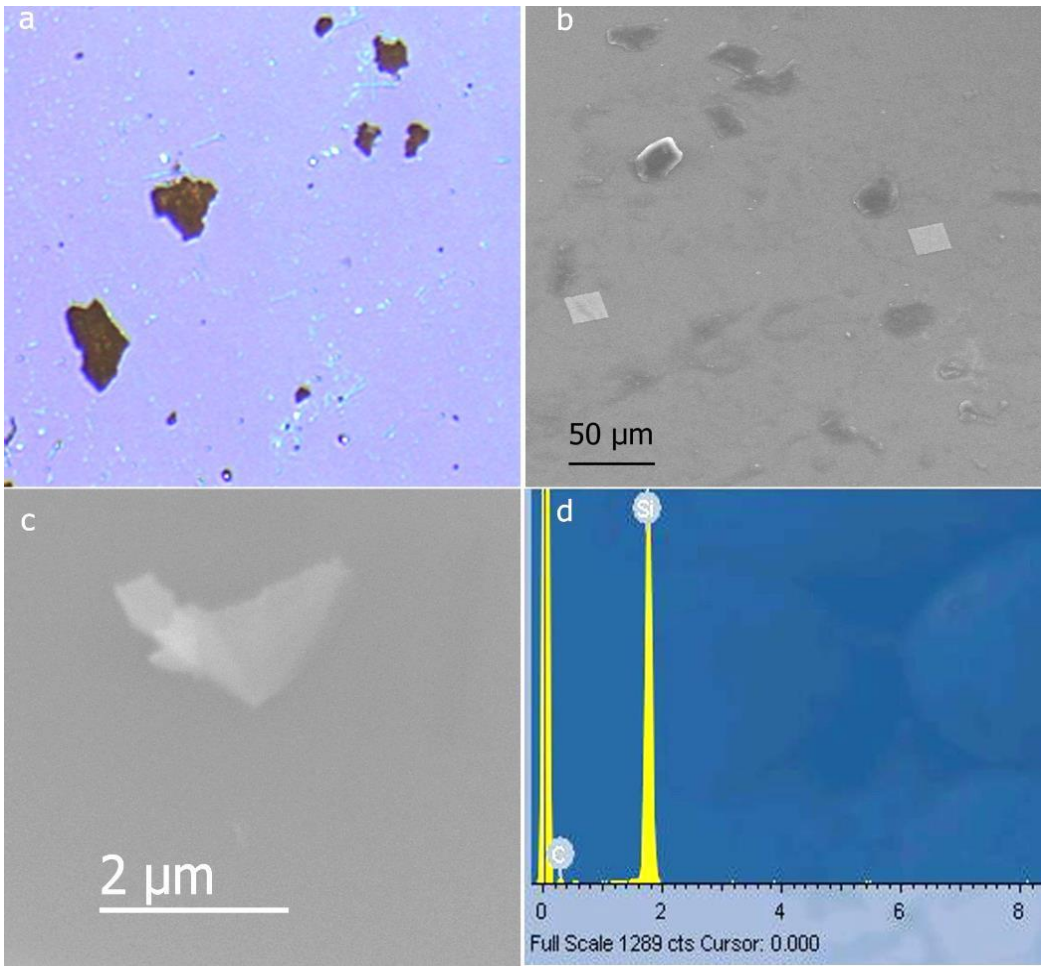

Fig 6.11 Morphological and compositional results of the 2D SiC flakes. (a) Optical microscopy image, (b) and (c) SEM images, and (d) EDS result.

Further high magnification image analyses (Fig 6.11c) reveal an average size of 2-5 μm for the flakes. EDS analyses of individual flakes show that they contain dominantly Si and C, with a C/Si atomic ratio slightly higher than 1. Earlier studies have showed that a higher C/Si atomic ratio makes 2D SiC energetically more stable [279].

To verify the detailed structural characteristics of the SiC flakes, we carried out TEM and nano beam diffraction (NBD) investigation on individual SiC flakes, and the results are displayed in Fig 6.12.

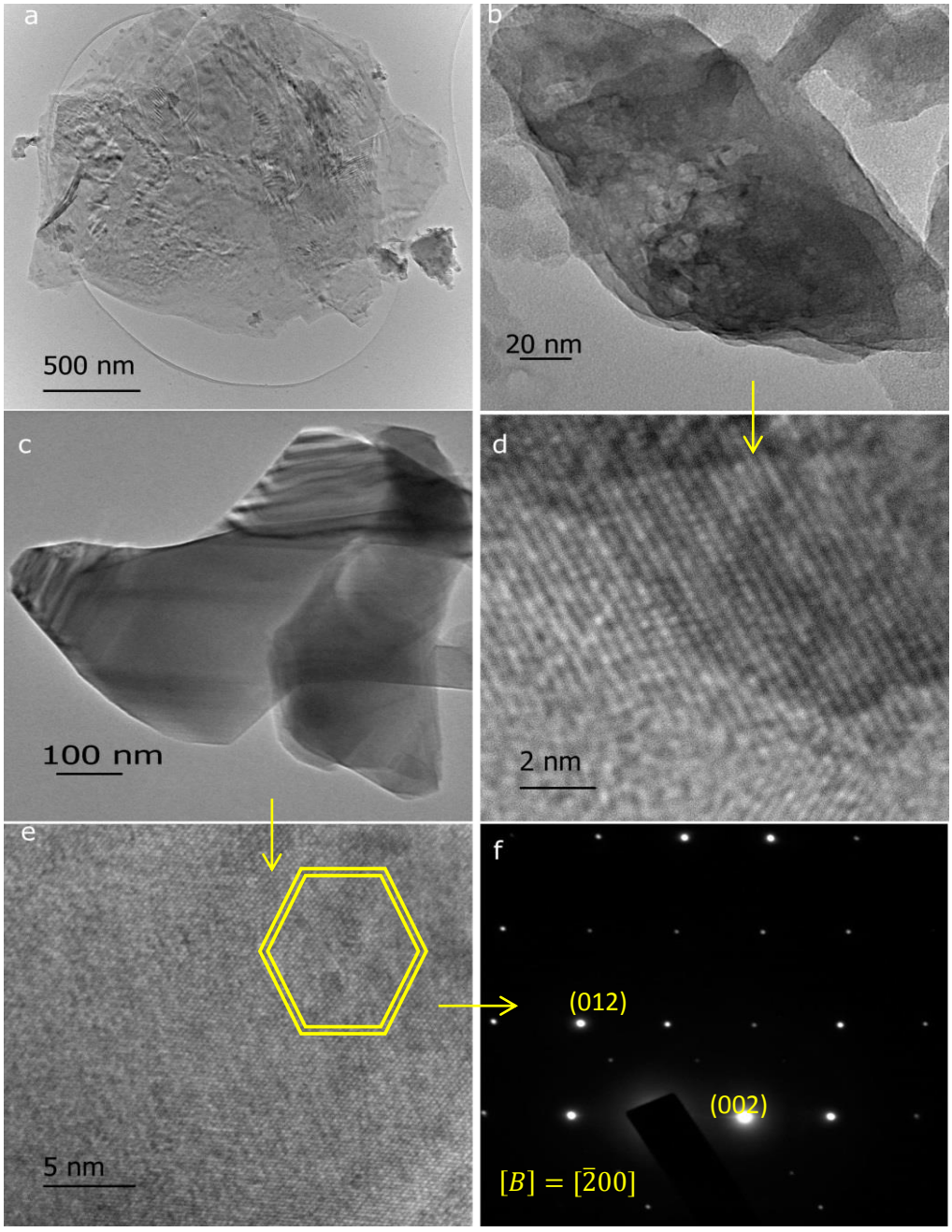

Fig 6.12 TEM images of the 2D SiC: (a-c) low resolution TEM images of SiC flakes, (d, e) TEM images, and (f) NBD pattern of the SiC.

At low magnification, Fig 6.12a, the SiC flakes appear to be flat, very thin and up to a few µm in size. Other SiC flakes shown in Figs. 6.12b and c exhibit smaller sizes and sometime curled in places, and their corresponding TEM images (Figs. 6.12d and e

respectively) show clear and sharp lattice fringes that reveal the well-crystallised structural feature. Using TEM information and NBD of different flakes, we have found that the as-synthesised 2D flakes have a hexagonal structure, dominantly 2H-SiC (Wurtzite). The flake in Fig 6.12c shows two regular interlayer spacing of 0.18 and 0.25 nm, which belong to the (012) and (002) planes of Wurtzite SiC. These clearly observable and indexed planes are consistent with the XRD analysis of the entire SiC foam. It is worth noting that Wurtzite structure is the only SiC polytype that shows an interlayer distance of 0.18 nm.

All observed planes showed a slightly larger (by about 0.003 nm) interlayer distance along the related zone axis than those we would have observed for a standard SiC Wurtzite crystal. The increase could be due to the existing defects in SiC sheets, the curved features, and also different thicknesses of the flakes.

Further elemental characterisations of the SiC sheets were carried out using a line-scanning technique during TEM observations, and the results are shown in Fig 6.13. Fig 6.13a presents a mixed scan of the three elements, Si, C and O, and Figs 6.13b-d correspond to the individual elements. It is obvious that both C and Si have high and stable density in the images over the selected areas of the sample, confirming the uniform composition of the nanoflakes.

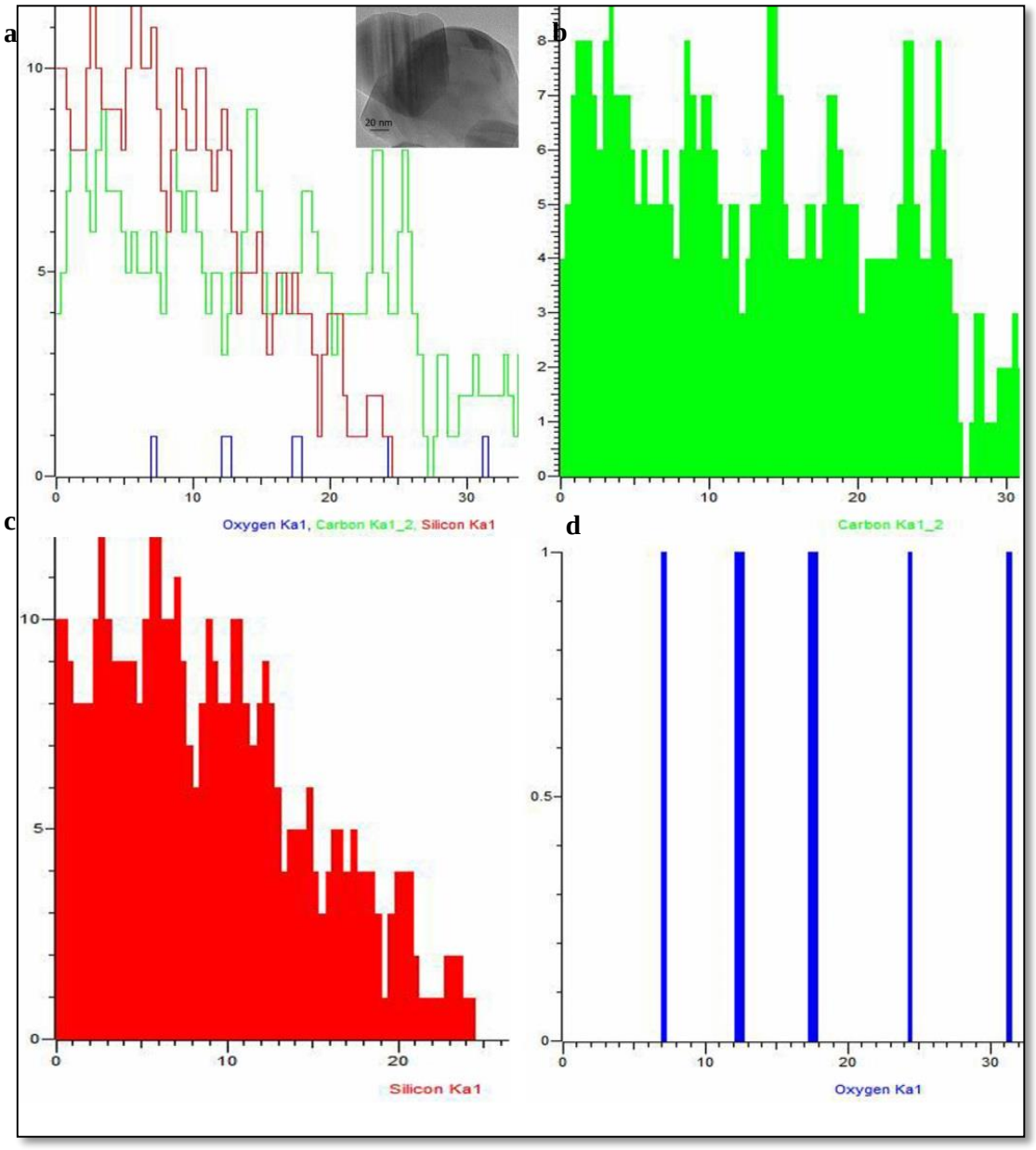

Fig 6.13 Line elemental scan of the 2D SiC. (a) Mixed scan of Si, C and O. The inset in (a) shows a TEM image of the scanned SiC sheets. (b) Individual line scanning of C, (c) individual line scanning of (Si), and (d) individual line scanning of O.

Raman characterisation results of the purified SiC flakes are displayed in Fig 6.14. Raman image of the characterised flake is shown in Fig 6.14a and the related spectrum is displayed in Fig 6.14b. The sample showed three Raman peaks at 763, 789, and 945 cm^{-1} which are well indexed to the SiC peaks and are attributed to the two TO modes of E2 and E1 phonons and one LO phonon peaks, respectively.

Further, the small shoulder at about 763 cm^{-1} is the TO mode of the SiC lattice and being considered as the characteristic Raman shift for the hexagonal structure [276,280,281].

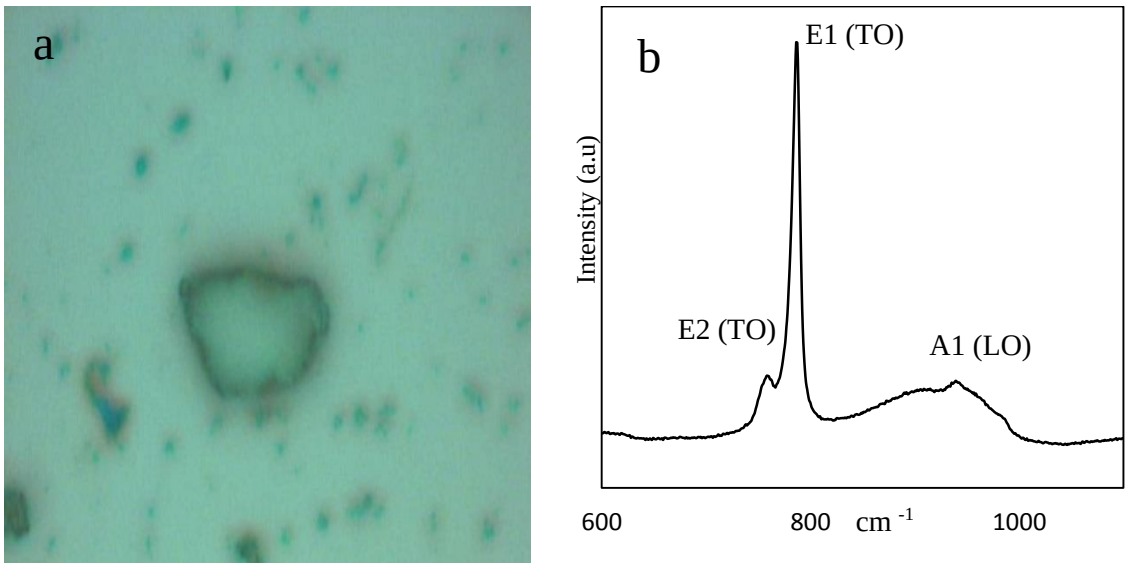

Fig 6.14 Raman results of the 2D SiC. (a) Spectroscopic Raman mapping of SiC flake taken at 10 x 50 objectives, (b) Raman spectrum of the flake shown in (a).

Comparing the active modes in 3D SiC and 2D flake, we have found that the TO mode at about 763 cm^{-1} is more active in the flake than in the 3D SiC, which we believe is due to the higher hexagonally percentage of the ultrathin SiC flakes. The 3D SiC foam, consists of cubic 1D SiC nanowires and hexagonal SiC flakes. Thus the reported Raman spectrum in Fig 6.7, represent the active modes of the entire 3D foam containing both the 1D SiC and SiC. However, in the present spectrum from purified flakes (without nanowires), we indeed noticed a slightly stronger signal for the E2 (TO) mode. Therefore, we believe that the hexagonal SiC is the main constituents of the flakes.

Further, both TO and LO modes shift towards lower frequencies in the SiC flakes. The shift is caused by a lattice disorder near the dislocation core and the formed defects

[282]. These Raman results are the most convincing evidence for the hexagonal structure of the resulting flakes. By comparing with spectra of other SiC polytypes, it is possible to use this to identify the key features of the SiC. As shown in Fig 6.15, the Raman spectrum of cubic SiC has two active modes, rather than 3, and it does not show the E2 (TO) mode [264,283,284].

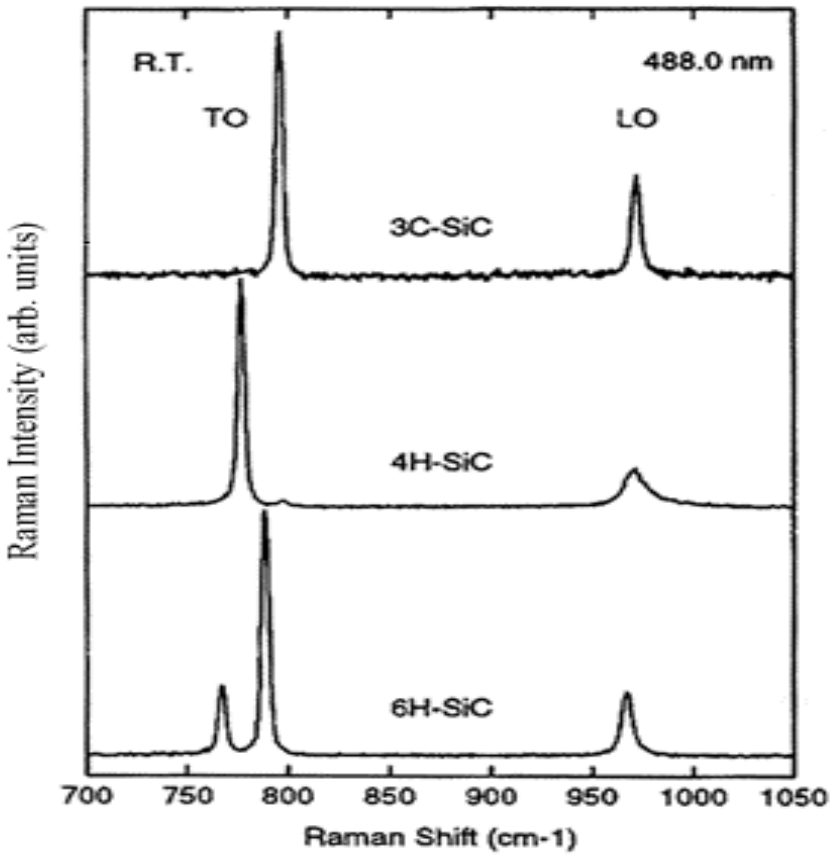

Fig 6.15 Raman spectra of 3 polytypes of SiC [264].

In the 4H-SiC, the intense peak appears at about 761 cm^{-1} and belongs to the E2 phonon, which is very weak in our case. Finally, since 6H-SiC grows only at very high temperature (> 1600 ºC) and our TEM results revealed Wurtzite structure for the flakes, we can rule out the likelihood of growing 6H-SiC in this research. Thus, we believe that these spectra further confirm the 2H-SiC structure of the purified ultrathin SiC flakes.

Fig 6.16 presents the results of the AFM measurement. Fig 6.16a shows the two main structures of the SiC foam, the 1D SiC nanowires and the 2D SiC nanoflakes. Obviously, the nanowire in the right hand side is on the top of the flake, and the left nanowire is underneath the flake. The dimensions of the two nanowires and the flake can be extracted from Fig 6.16b. The intense peaks in this graph are due to the coexistence of both nanowires and the flake at those positions, and it reflects the flexible nature of the flakes. As shown in Fig 6.16b, this SiC flake has an average size of 2 μm and a thickness value of 3 nm. Meanwhile, the 1D nanowires have an average diameter of 20-100 nm, obtained from the two intense peaks in the line scan profile in Fig 6.16b.

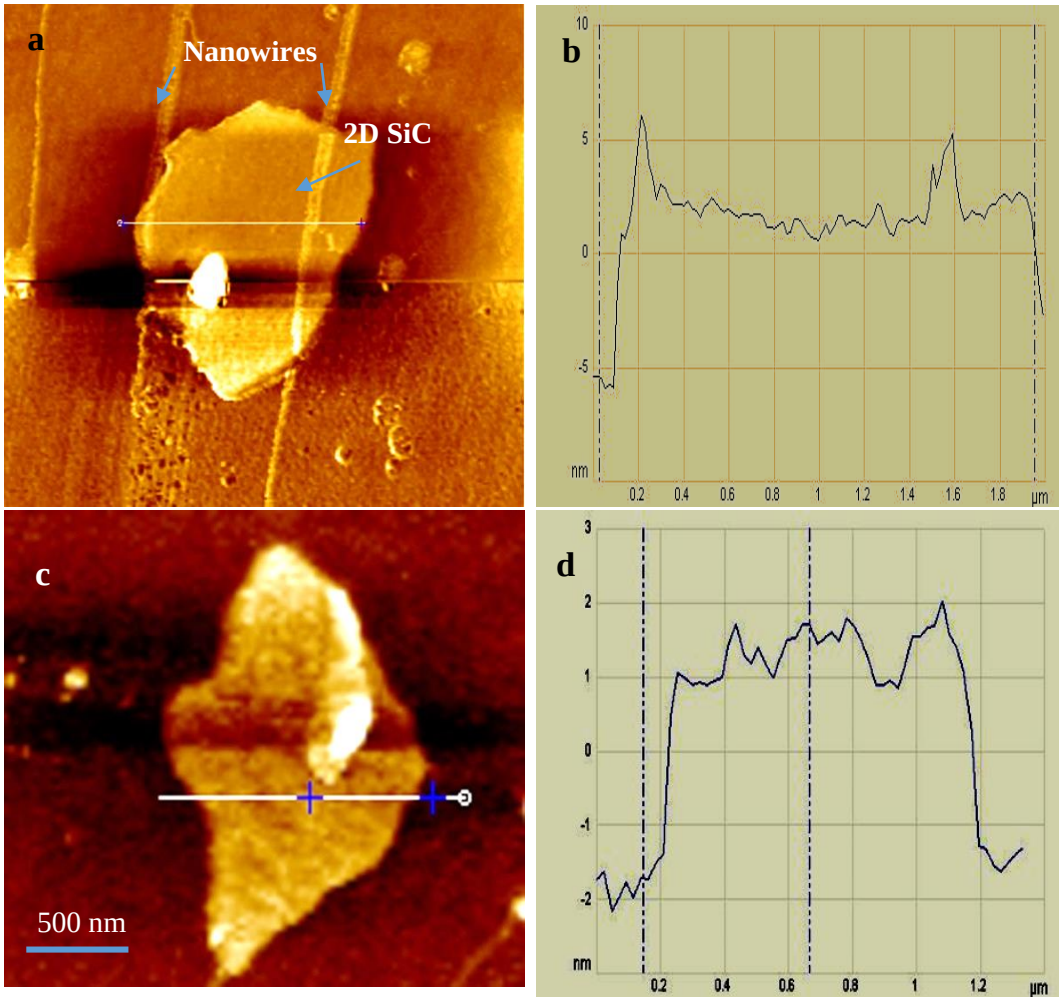

Fig 6.16 AFM results of the SiC sample. (a) AFM image of the tested SiC sample showing a large SiC flake and some SiC nanowires across the horizontal scan line, (b) the height-length profile of the SiC structures shown in (a), (c) AFM image of a single SiC flake, and (d) the height-length profile of the flake shown in(c).

Figs 6.16c-d show the AFM results of a pure SiC flake. The results not only reveal the average size of 1-2 μm for a 2D flake after the sonication treatment (subject to possible break down), but also further confirm the ultrathin feature of the SiC sheets, with only an average thickness of 2-3 nm. Given that the SiC possesses an interlayer distance of *ca.* 0.25 nm, it is not difficult to estimate that the SiC flakes consist of 7-10 atomic layers.

Indeed, the size of the SiC flakes and their thickness are affected significantly by the dimensions of the carbon template, and the ultrathin 2D SiC flakes were grown as a direct result of the few layer structure of the GF template. The TEM results revealed varied thickness and size for the SiC flakes, with slightly increased interlayer distance, which we believe is a result of various numbers of the graphene layer in the curved foam and the level of defects in the graphene flakes.

In addition to the effect of GF size and structure [280], the experimental conditions can favour the growth of specific SiC polytypes. For example, there might be a possible structure transformation from 2H-SiC to 3C-SiC and then to 6H-SiC, or even a direct transformation from 2H to 6H, at higher temperatures [285,286]. Such changes will not only alter the crystal structures, the interlayer distance, and the physical appearance of the products, *e.g*. colour and flexibility, but also will affect the electronic and physical properties of the 2D-SiC. In this work we only investigated the effects of the synthesis temperature briefly, and we noticed that it was very difficult to find large SiC flakes at high temperatures (>1550 ºC), instead SiC nanowires were the dominant products. Based on our observation, 2D SiC flakes were mostly stable in the temperature range of 1380 -1500 ºC. At high temperatures such as 1575 °C, 1D SiC nanowires was the pronounced structural phase.

6.6 Summary

Novel 3D SiC structures have been generated by a carbothermal reduction of SiO with GF. They consist of hollow truss structures made from layered SiC layer which breaks into flakes, and long 1D SiC nanowires growing from the trusses, edges and defect

sites. The nanowires appear to be highly flexible, exhibiting various diameters and lengths.

Our SEM and TEM analyses revealed the average size of 2 μm with an average interlayer distance of 0.255 nm for the SiC nanoflakes. Using AFM characterization, we have confirmed that the thickness of the nanoflakes was 2-3 nm on average, corresponding to *ca*. 7-10 atomic SiC layers.

This novel type of semiconducting nanoflakes not only significantly enriches the family of 2D structures, but also expects to exhibit many new electronic and optical properties, which will open up fresh opportunities for vast interesting applications in advanced nano device design and constructions.

Chapter 7 : Mechanical properties of the light-weight graphene foam and SiC foam

7.1 Introduction:

Conventionally, the concept of lightweight refers to structures with density (ρ) range of 0.3 -5 g cm^{-3}. The new generation of lightweight materials however, is three orders of magnitude lighter in density than the conventional ones. Graphene foam (GF) [55], CNT-graphene aerogels [287] ,silica aerogel (ρ > 1.5 mg cm^{-3}), metallic foam (ρ > 10 mg cm^{-3}) [288], nano-fibrous aerogels (NFAs) (5.3 <ρ<9.6 mg cm^{-3}) [289], boron nitride (BN) foam (ρ: 1.6 mg cm^{-3}) [290], Fe_2O_3/C [291], Co/C [291], Ni/C [291] with ρ < 5 mg cm^{-3} and other similar foams[292,293], all can be classified as modern lightweight or ultralight foams with extremely low densities.

Although most of the lightweight foams followed the general law for conventional materials and their compressive modulus tend to decrease dramatically with decreasing the density, *i.e.* $\frac{E}{E_S} \propto \left(\frac{\rho}{\rho_S}\right)^{n=2\ or\ 3}$ $Eq.7.1$ or $\frac{\sigma}{\sigma_S} \propto \left(\frac{\rho}{\rho_S}\right)^{n=2\ or\ 3}$ $Eq.7.2$, where E is the Young's modulus σ is the yield strength and n is the scale power, some new ultralight metamaterials such as hexanediol diacrylate (HDDA) polymers showed a nearly linear density-strength dependence rather than the quadratic or cubic relationship for conventional lightweight materials [293-295], which is very interesting and promising as the failure modes in these metamaterials are stretch dominated[286].

Other studies on lightweight ceramics reported a scaling of $E \sim \rho^{1.6}$ for the hollow-tube alumina micro-lattice [292], which is a significant response that non-exist in conventional brittle ceramics.

As shown in earlier chapters, we produced two types of lightweight foam: GF and 3D SiC by using CVD and carbothermal techniques respectively. Both the GF and SiC foam showed good flexibility and more importantly the GF and GF-based composites showed excellent capacity retention after thousands of charge-discharge cycle which we believe is a direct result of the mechanical properties of the foam. This chapter will investigate the mechanical properties of both the GF and SiC foams, and provide evidence to support our previous analysis for the excellent capacity retention performance of the GFs.

7.2 In-situ compression of the GF

The mechanical properties of the GFs were studied mainly by conducting compressive test under in-situ SEM imaging. Fig 7.1 shows the SEM images of GF_a (sample a, ρ: 3-5 mg cm^{-3}) during the compression test. Fig 7.1a, is an in-situ SEM image of the GF before the compression test and during the preparation stage.

The 3D well-connected network is visible in this image. Fig 7.1b is a low magnification SEM image of the GF under maximum load of 1.12 N. Under maximum compression, the foam becomes highly compressed and its thickness reduces to *ca*. 0.4 mm from 1.6 mm, (a) to (b) in the figure. As shown in the picture, despite the high strains of the compression, the foam kept its original shape, even under high loads.

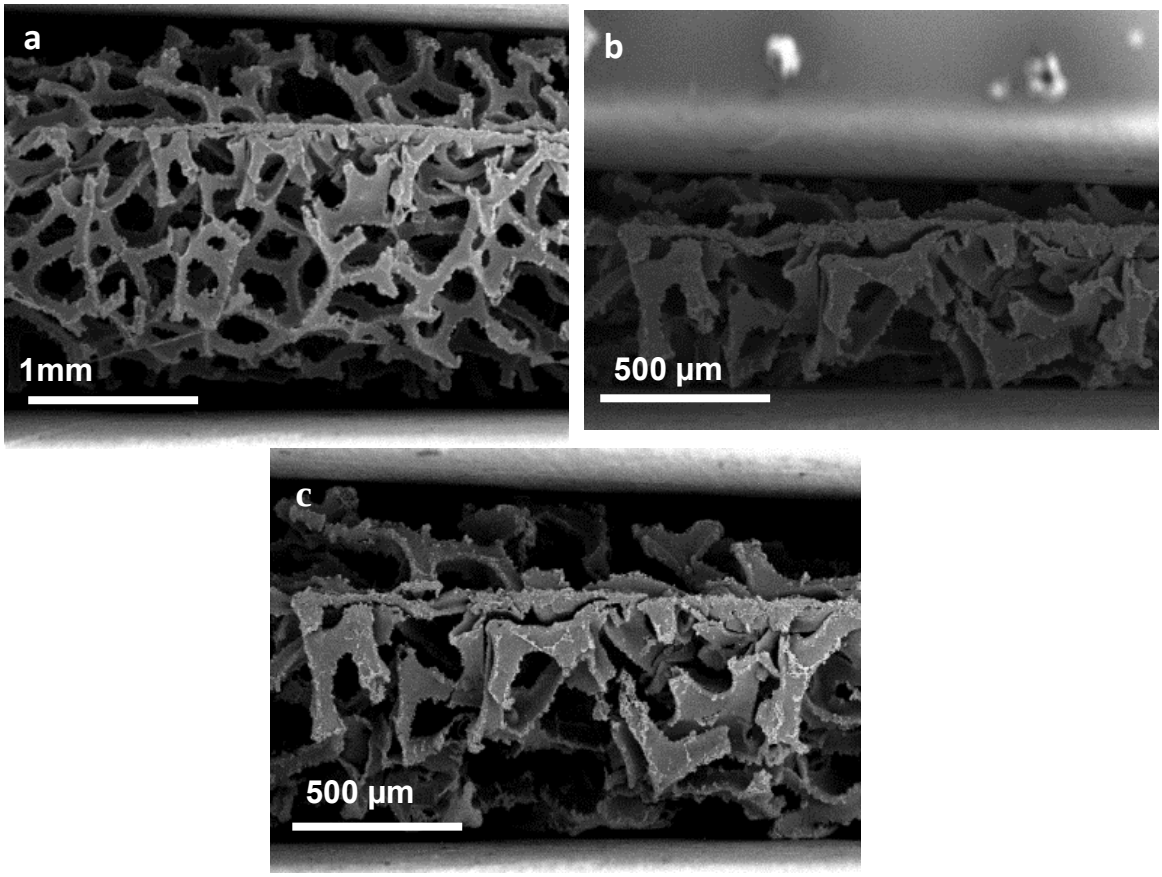

Fig 7.1In-situ SEM images of the GFa during compression test. (a) before compression, (b) under maximum load, and (c) unloading stage.

Upon unloading, Fig 7.1c, the thickness of the GF increases again and recovers significantly. Fig 7.2 shows high magnification SEM images of the foam before the compression test and under 0.88 N load or *ca*. 60% strain. Ideally, except for a very small crush around the junction, there was no significant structural damage occurred subject to 60% strain and the foam showed very good stress tolerance. However, depending on the local microstructure such as orientations and the initial defects of the GF, some its parts might be stronger than other parts.

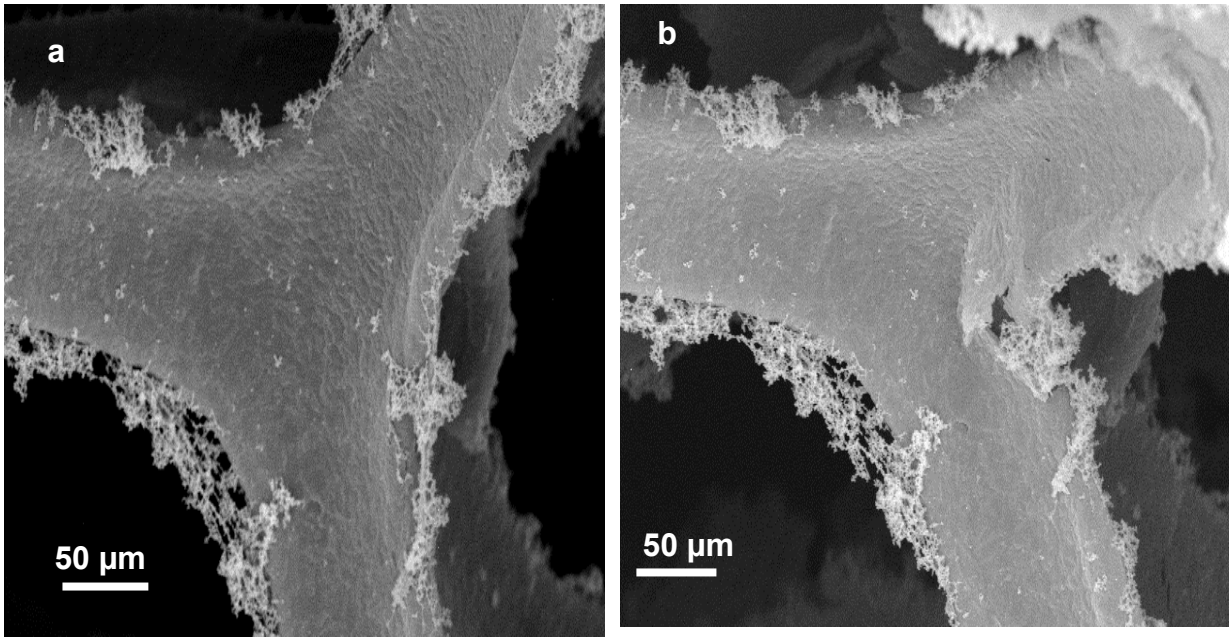

Fig 7.2 High magnification SEM image of GF_a before the compression test (a), and under 0.88 N load (b).

The effect of density on the mechanical property of this type of open-celled GFs was also studied. Fig 7.3 shows SEM images of GF_b (ρ: 6 -8 mg cm^{-3}) at different stages of compression tests. Generally, this foam showed very similar behaviour to GF_a.

As shown in Fig 7.3, the formed cracks during the initial compression steps remain almost local until the end of the test, and there is no sudden structure collapse. This slow structure loss could be attributed to the interconnected feature of the foam, and the strong in-plane covalent bonds which contribute positively to the foam stability and protect it from sudden collapse.

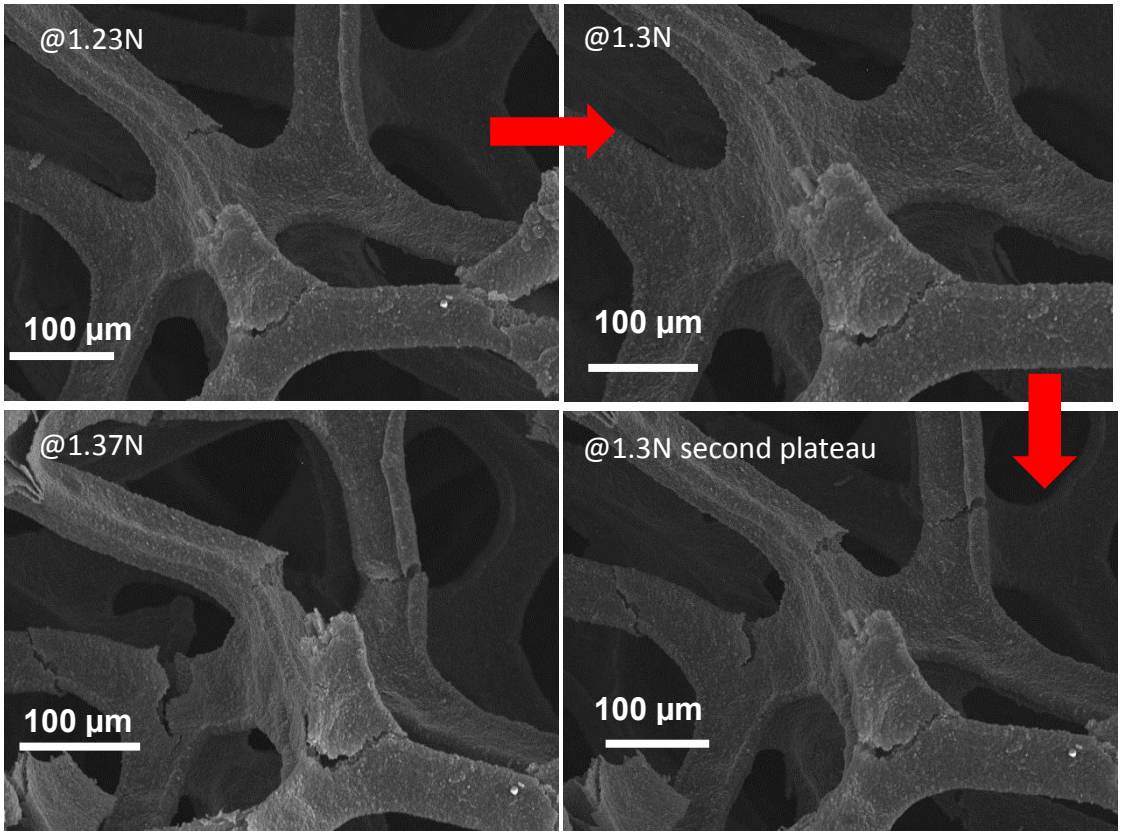

Fig 7.3 In-situ SEM images of the GF_b under compression cycles.

Fig 7.4 shows high magnification SEM images of the foam under high compression loads. Again, although there are significant crack propagations, there is no catastrophic failure. Instead, the damage stays local and spreads slowly rather than a quick propagation.

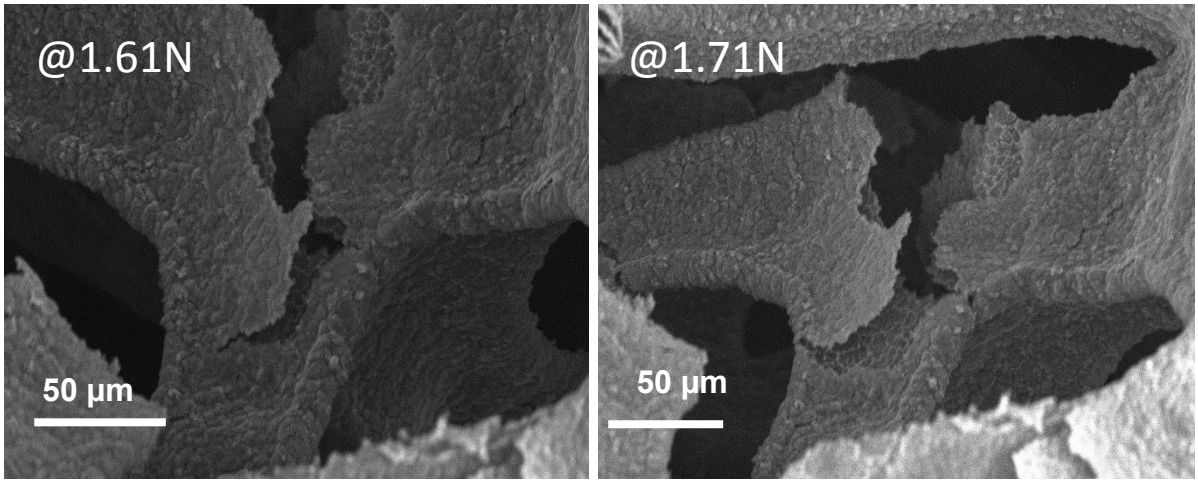

Fig 7.4 In-situ SEM images of the GF_b under compression tests.

Fig 7.5 shows the compressive strain-stress curves of GF_a (ρ: 3-5 mg cm^{-3}) and GF_b (ρ: 6-8 mg cm^{-3}). Compared with GF_a, GF_b, with a higher density value, shows slightly higher stress values at all strain levels. The increased compressive stress in GF_b is related to its increased wall thickness. However, both curves follow a similar trend which is a typical strain-stress response for open-cell foams: an elastic region at small strains, followed by a plateau region, and finished with a densification.

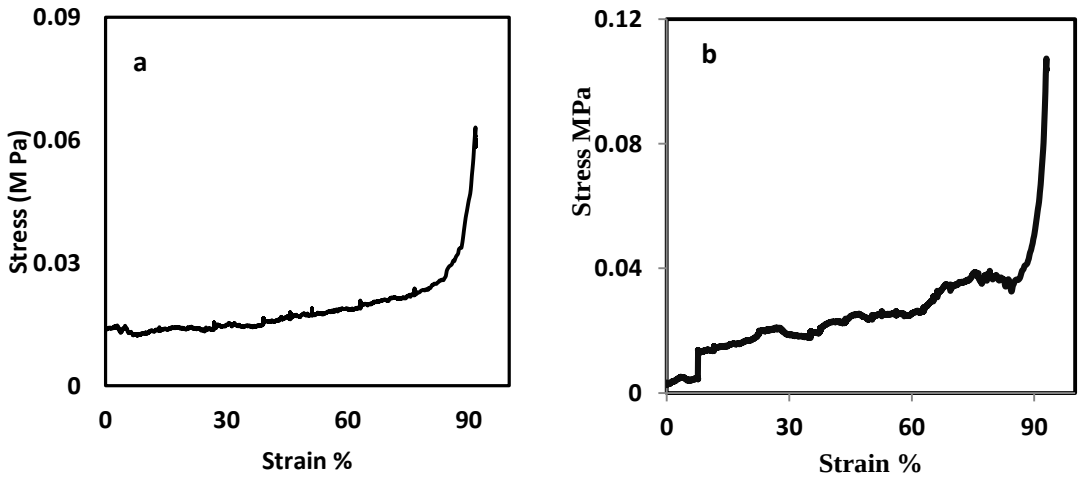

Fig 7.5 Stress-strain curves of the GFs. (a) GF_a (ρ: 3-5 mg cm^{-3}), (b) GF_b (ρ: 8 mg cm^{-3})

The elastic stage (or the so-called Hookean region) is due to the bending of the foam cell walls prior to the occurrence of any damage or crushing. The plateau region is a result of the brittle failure of the cell walls. When almost all the cells get crushed under compression, the opposing cell walls touch each other in compaction, leading to the final densification region. Benchmarked against the best existing ultralight foams ($\rho <$ 10 mg cm $^{-3}$), we note that our foams possess one of the highest compression strengths in the literature[144,296]. Further, both foams showed very long plateaus, indicating their good applicability as an energy absorber.

7.3 Effect of the pre-pressing on the mechanical properties of the GF

The effects of the pre-pressing on the mechanical properties of the GF were investigated by conducting tensile experiments, on an assembled tensile testing machine.

As shown in Fig 7.6, the pressed GF absorbs much higher loads at all strains. The maximum absorbed load of the pressed GF is 0.04 N, while it is only 0.006N in the non-pressed foam, indicating a 6-7 times increase in the mechanical properties of the foam through pressing.

Moreover, pre-pressed GF shows a much more homogenous response than non-pressed foam. The thick line in Fig 7.6a shows clearly that this is due to the lack of uniformity in the foam at different testing points.

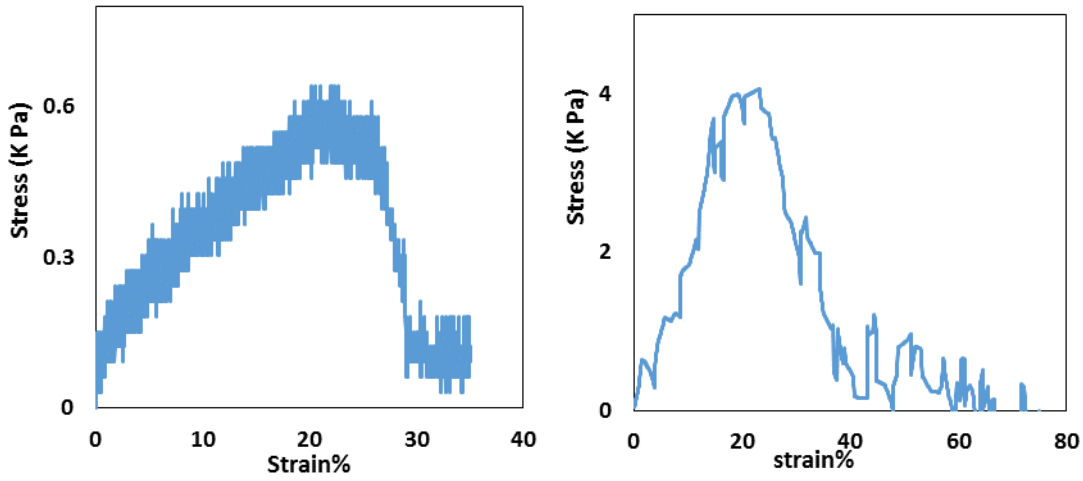

Fig 7.6 Load-strain curves of (a) non-pressed GF and (b) pressed GF.

The small but consistent noise in the signals in the pre-pressed foam, Fig 7.6b, is believed to arise from the contributions of breaking layers of graphene during stretching. In fact, the gradual progression allows for the majority of layers in the network to contribute positively to the mechanical strength of the foam, and this effect is shown in the sudden increased loads at certain points, as other layers try to maintain the integrity of the foam while some damaged layers are broken.

The improved mechanical properties of the pre-pressed GF, over pristine GF, can be related to the reduced thickness of the foam which leads to a more homogenised response[297].

7.4 Mechanical properties of SiC foams

The mechanical properties of the SiC foams were also investigated by conducting compressive tests under in-situ SEM imaging. For these tests, two SiC foams, SiC_a (ρ: 9-10 mg cm^{-3}) and SiC_b (ρ: 15-17 mg cm^{-3}), were investigated and compared. SiC_b was prepared by using a denser GF (ρ = 8-10 mg $cm^{-3)}$ for the carbothermal reduction.

Fig 7.7 shows a series of sequential SEM images during the SiC_a compression. Obviously, there is no sign of structure loss or catastrophic fracture in the images. Despite the high strains of compression at 26%, 33% and 76% for a-b, b-c and c-d, respectively, the foam kept its original shape and its main apparent features under increasingly high loads. Its unit cells, as shown with circles in Figs. 7.7a and 7.7c, are almost intact, and even under maximum compression the foam showed a good damage tolerance. This behaviour is due to elastic-plastic response of the foam which can be better explained by using the corresponding stress-strain curve.

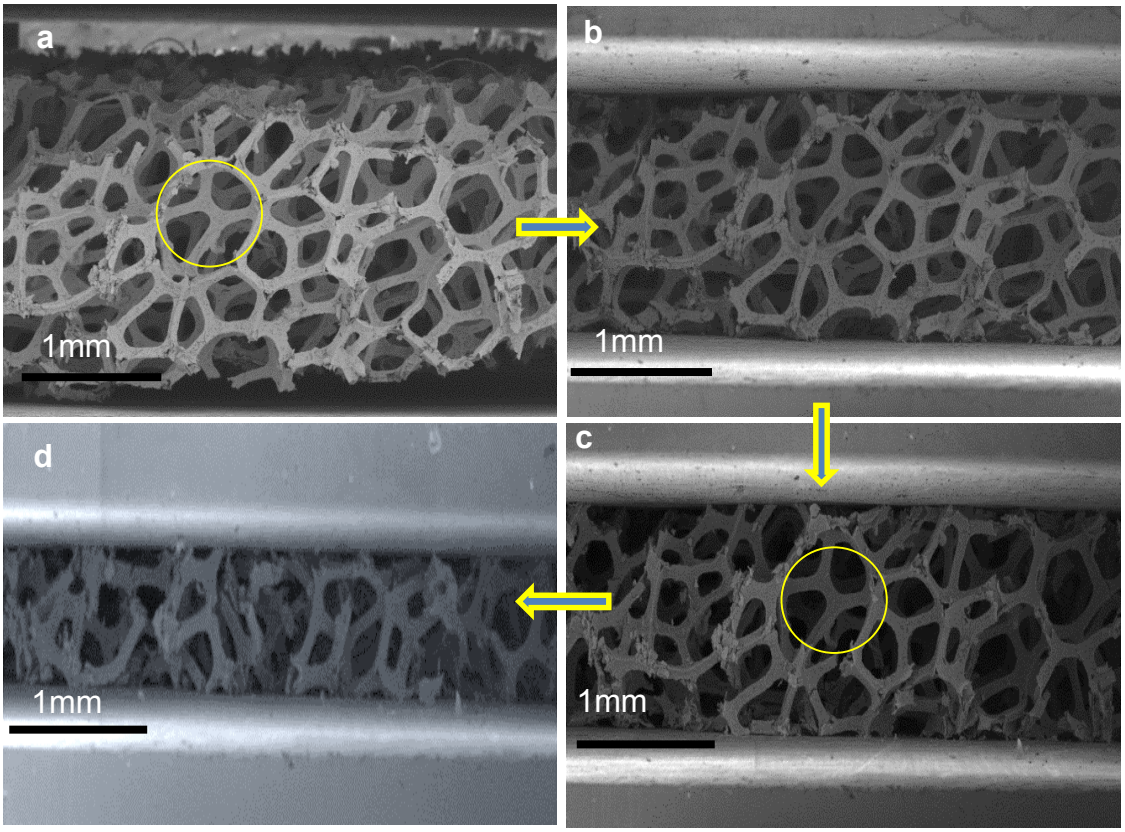

Fig 7.7 In-situ SEM images of the SiCa during the compression test. (a) Pre-compression, (b) under 0.8 N load, (c) under 1.3 N load, and (d) under 3.9 N load.

The stress-strain graphs were obtained from the load-displacement data and the information of cross-sectional area and thickness of the foam. As shown in Fig. 7.8, there are three distinct regions: an elastic region at low strain (ε), a plateau area, and a densification region, similar to the GFs.

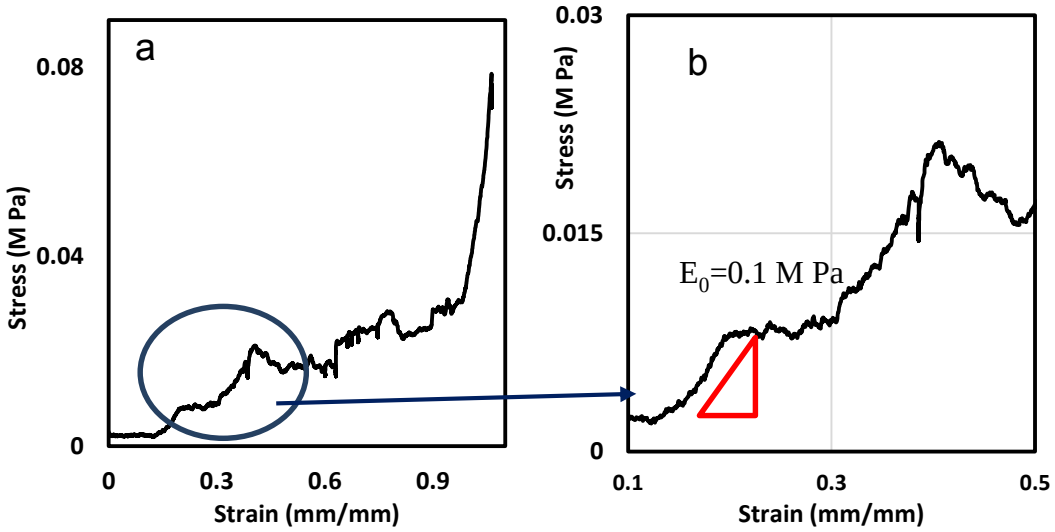

Fig 7.8 Compressive stress-strain curves of the SiC foams. (a) strain data of the SiC_a collected from the compression machine; (b) a magnified strain-stress plot of the SiC_a showing only the area in the circle in Fig. 6(a), and the small triangle represents the elastic trend.

From the elastic region in Fig 7.8b for foam SiC_a, marked by a small triangle, a value of 0.1 MPa for the Young's modulus (E_0) and a peak stress of 0.023 MPa were obtained. In the second region, the plateau step, the stress decreased slightly at first followed by a non-linear stress/strain change, which could be attributed to the buckling and wrinkling of the cell walls. The foam shows a long plateau step with continuous small stress changes. This behaviour is due to the interconnected feature of the 3D foam and the nanowires that act as supporting beams which together resisted and delayed the foam from sudden breakage.

Fig 7.9 shows in-situ SEM images of SiC_b (ρ = 15-17 mg cm^{-3}) under compression tests. Fig 7.9a is an SEM image of SiC_b before the comression tests. It shows a very dense 3D network that covers entirly with SiC nanowires. Fig 7.9b shows an image of the foam under 1.55 N load. Obviously there is no big structual difference from (a).

Despite under strain values of 20% (from a to b), 62% (from a to c) and 72% (from a to d), the foam kept its apparent 3D structure almost intact.

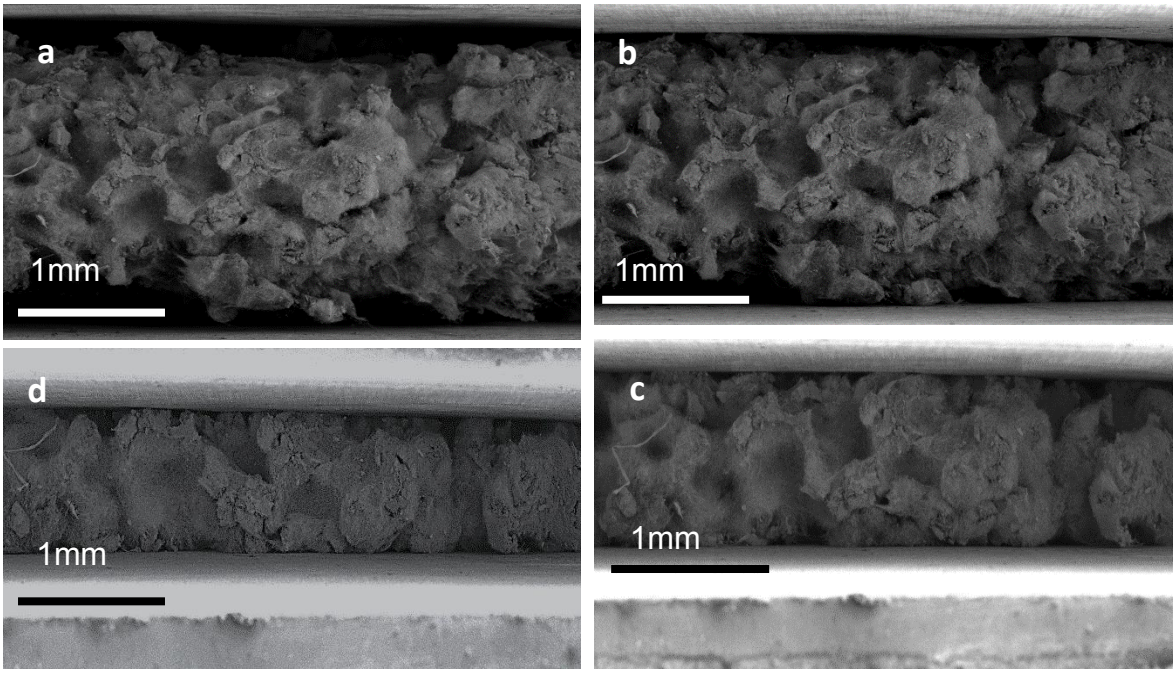

Fig 7.9 In-situ SEM images of the SiC_b during the compression test. (a) Pre-compression, (b) under 1.55 N load, (c) under 6 N load, and (d) under 17.5 N load.

Fig 7.10 shows the strain-stress graphs of SiC_b. It also consists of the initial elastic region, followed by the long plateau step plastic deformation. This implies that the sample responded to the applied stresses dominantly via the buckling mode, without experiencing a quick crush.

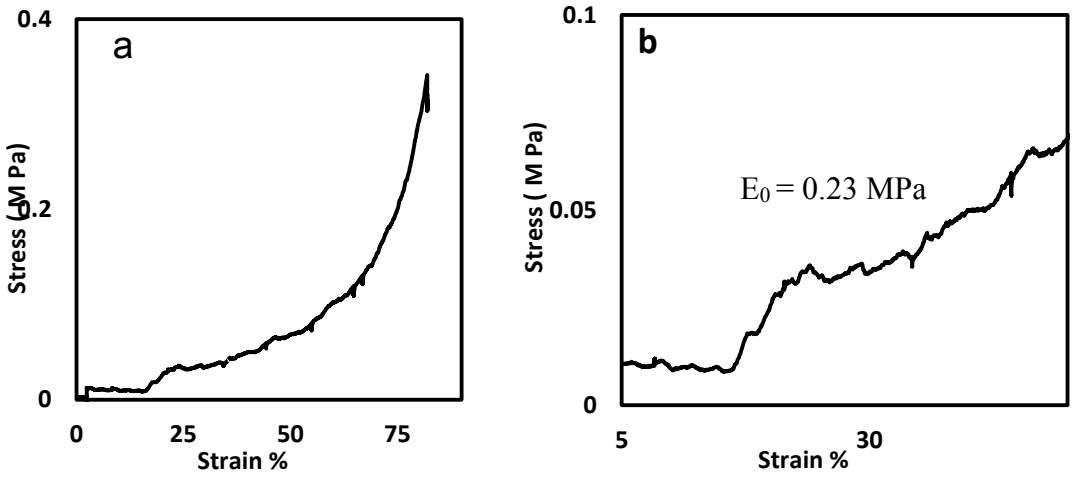

Fig 7.10 (a): The recorded stress-strain curve of the SiC_b foam and (b): a magnified strain-stress plot of the SiC_b.

Compared with SiC_a, SiC_b absorbed much higher loads at all strains, this phenomenon could be attributed to the increased density which originated from the increased thickness in the cell walls. We obtained a value of 0.23 MPa as the Young's modulus for SiC_b, with a plateau strength of 0.057 MPa at 44%.

Upon unloading, as shown in Fig 7.11, the foam recovered partially, with a 40% strain remaining. This partial recovery is due to the elastic buckling of some parts of the cell walls and also arises from the undamaged nodes in the foam which result in foam recovery even if some trusses are collapsed or damaged, similar to the GFs. However, this recovery feature is very unusual in ceramic materials, and it emphasises that the present SiC foams do not follow existing mechanical trend of bulk SiC materials or even lightweight SiC materials[298,299] , as other ceramics would be collapsed during the compression, subjecting to very little stains. In this context, the damage is likely to stay local in most parts, rather than affecting the entire integrity of the foam.

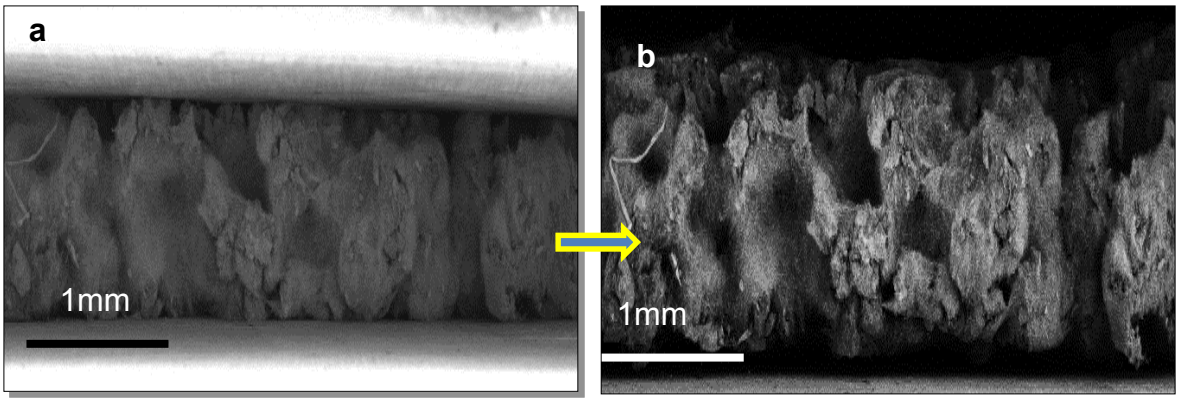

Fig 7.11In-situ SEM images of the SiC_b under testing. (a) Under maximum load, and (b) unloading stage.

It is noteworthy that compared with SiC_a, SiC_b exhibited less structural damage under comression tests, possibly because sample SiC_b contains a higher content of nanowires. As shown in chapter 6, the 1D SiC nanowires are highly flexible, thus they must have contributed positively to the foam integrity under stresses. An higher magnification SEM image, Fig 7.12, shows clearly that the nanowire is the most tolerablabe structure to the damage during compression. They appear to be tangled with each other from different angles and surfaces (both internally and externally) and provide excellent support, as a reinforcement phase, to hold the framework together when part of the SiC layers broke, improving the strength of the SiC foam.

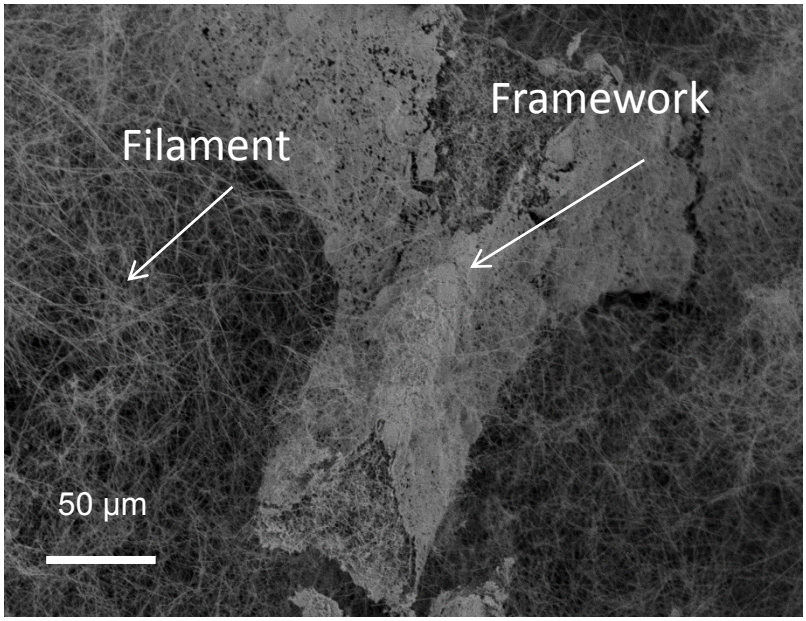

Fig 7.12 High magnification SEM image of the SiC_b.

These results are in cotrast to the obsereved behaviour of the GFs. In the GF, a foam with lower density showed much better tolerance to the applied compressive stress, since the higher porosity reduces the required void space for stress release. In other words, higher density in the GF results in less flexiblity. However, higher density results in higher contents of flexible nanowires, and leads to more flexible SiC foams.

Table 7.1 lists the compression values of various lightweight foams with density values of $\rho < 50$ mg cm^{-3}. The results have shown that our foams possess one of the highest compression strengths in the literature, even stronger than the GFs we have produced earlier.

The extremely lightweight SiC_a foam with a density of only 10 mg cm^{-3} reached a peak yield strength of 23 kPa, and the SiC_b reached a remarkable plateau strength of *ca*. 0.06 MPa which is higher than many lightweight foams, including BN [300], GFs and even some of the metallic micro-lattice [288].

The present lightweight SiC foams show some similarities with metamaterials reported in the literature [292,293], particularly the mechanical responses follow the same trend to the 3D hollow-tube alumina micro-lattice (ultrathin wall) reported by Geer's group. For example, they both showed a partial recovery upon unloading after very high strains. In the case of the alumina reported, its compression strength is even higher than current SiC foams, and we believe this could arise from the native 3D architecture used.

The hollow-tube alumina lattice was prepared by the laser lithography technique with a precise control over nano to micro scales [286], however the template used here is commercial random 3D foams and the 3D interconnected feature is not ideally placed for achieving maximum strength.

Further, we believe that, different from other 3D foams in which solid particles were stacked together via diffusion across grains to form a network with huge structural defects, the current 3D SiC foams were a direct conversion from the GFs during the carbothermal process. The continuous layer-by-layer carbothermal reaction resulted in covalently bonded 2D SiC sheets. This layered SiC defined the shape and properties of the resulting 3D foams. Finally, the strong and highly flexible 1D nanowires may have assisted the 2D SiC trusses in holding the integrity of the entire 3D foam, under extreme loading-unloading process, thus possessing outstanding mechanical properties for the ultralight structures.

7.5 Summary

The mechanical properties of the GF and SiC foams were investigated by conducting in-situ compression tests under SEM observation. Regardless of their low density, the GFs are mechanically robust and highly flexible. These foams can be used as components for energy absorber. These results also provide evidence for the excellent cyclic performance for the GF-based materials as electrode for energy storage applications.

Using highly porous and ultralight GFs as the template and carbon source, we have successfully produced the lightest SiC foams in the world. The resulting SiC foams have an average thickness of 2 mm, with density ranging from 9-17 mg cm^{-3}.

The 3D foams showed excellent compression strengths, being one of the strongest 3D foams against any other ultralight materials. They exhibited a 40 % recovery subjecting to compression strains exceeding 70 %. The unique features of the partly hollowed trusses, the 2D SiC flakes and the 1D nanowires all contributed to the ultralight, strong and flexible features of the foam. These new lightweight structures are promising for use as insulating materials and energy absorbers.

Chapter 8 : Conclusions and future work

8.1 introduction

The main aim of this PhD work was to investigate the synthesis and the properties of novel 2D and 3D graphene-related materials. In this thesis, 2D graphene, 3D GF and its 3D PPY-GF and PANI-GF composites, 2D SiC nanoflakes and 3D SiC foam structures have been generated, characterised and reported. Using GF as the starting materials and backbones, we have successfully extended its research to another brand new area, first investigated and created other graphene-based 2D and 3D and materials. This chapter will first present our main achievements, and then describe the potential future research prospects based on my own understandings from the research work.

8.2 The main achievements

1. The successful creation of large 3D GFs of extreme lightweight, high flexibility, with interconnected porous networks. These foams are ideally suitable for use as scaffold in the preparation of various free-standing 3D electrodes. This result promotes the research in graphene and 3D material synthesis, contributing to materials science.

2. When used as supercapacitor electrodes, our results confirmed that the GF and PPY-GF composite electrode demonstrated a near 100% capacity retention after 10,000 charge-discharge cycles. This excellent capacity retention refers to the high mechanical integrity of the foam, high flexibility of the foam and its porous structure. The open porosity feature of the foam is very helpful in stabilizing the surface morphology of the PPY redox counterpart, as the pores can function as a host to the redox elements and accommodate the strains in the entire electrode structure during

repeated charge-discharge cycles. This result has contributed significantly to tackling the challenging cyclic issues in EES devices, benefiting energy storage technology advances.

3. We have achieved very impressive 660 F g^{-1} capacitance for the PPY-GF composite electrode, with both the battery-like energy density and capacitor-like power density, which is one of the best values reported in open literature. The main reason behind this performance is the ideal 3D structure of the electrode which allows for very efficient charge storage process.

4. We have first realised the creation of a class of novel 3D SiC foams, using a conventional carbothermal reaction starting with the GF template. The resulting 3D SiC are made from continuous, hexagonal layered 2D SiC, reinforced with 1D 3C-SiC nanowires that grown simultaneous during the carbothermal formation, depending on the experimental parameters. This new 3D SiC thus is completely different from any existing 3D ceramics, due to its continuous layered SiC structures. Therefore, this has extended the 3D graphene research into a new arena.

5. After breaking the 3D SiC and purifying from 1D nanowires through a multi-step sonication procedure, we have successfully achieved large ultrathin SiC nanoflakes for the first time. The resultant 2D SiC are multi-layered (5-9 layers), with an average thickness of about 2 nm. The GF template-assisted creation allows for the control of the SiC layer numbers by utilising GFs with different layers, as the SiC nanoflakes will have very similar thickness to their paternal template. The SiC nanoflakes showed a slightly increased interlayer distance, 0.255 nm vs 0.252 nm for 2H SiC, and we believe that this enlarged spacing is due to the curvature and defects in the layers.

6. Finally, we have investigated the mechanical properties of both the GF and SiC foams by conducting in-situ compression tests. We have found that, similar to the GF, the SiC foams also exhibited an impressive high recovery after compression. We have analysed mechanisms for this unusual behaviour in ceramic foams, and discussed the advantageous of our synthesis approach. We have confirmed that the key role of the GF template and the layered structures for the SiC and the reinforcement effect of the nanowires all played a role in the ultralight, flexible and strong new structures. Importantly, we have confirmed that both foams are amongst the lightest and strongest structures reported to date. This will contribute to general advanced materials research, particularly to the emerging fields for ultralight and ultra-strong metamaterials.

8.3 Future work:

Based on the results and my observations, I would like to recommend the following works for future directions.

1- For the purpose of graphene foam productions, there is no need for long time *e.g.* 1 h synthesis process. H_2 is very dangerous gas. Thus, the best alternative would be to reduce the synthesis time to 10 min and to increase the flow rate of the carbon source accordingly.
2- The pre-pressed GF needs further investigation as it showed superiority over the GFs in both tensile test and electrochemical test. It can also be used as substrate for preparing other materials.
3- Ni-assisted CVD method can be used for generating other lightweight 3D materials, providing that one can practically uses a minimum flow rate for the injected reactants.

4- Although the produced SiC flakes are indeed a very interesting structures and the process itself was successful, further works need to be done in this field. Starting with carbon source, we really do not have to start with 3D graphene foam, instead graphene flakes can be used as the template. Further, the sonication process needs to be optimised. Thinner and larger flakes can be explored by changing the solvent and the exfoliation methods. Both surfactants solvents and polymer solvents can be used.

5- Finally, I do recommend graphene production from the synthesised SiC foam via graphitization method. Structural characterisation of the GF before and after SiC transformation can provide important structural information about both GF and SiC.

References

1 Stankovich, S. *et al.* Graphene-based composite materials. *Nature* **442**, 282-286 (2006).

2 Balandin, A. A. *et al.* Superior thermal conductivity of single-layer graphene. *Nano Lett* **8**, 902-907 (2008).

3 Chen, J.-H., Jang, C., Xiao, S., Ishigami, M. & Fuhrer, M. S. Intrinsic and extrinsic performance limits of graphene devices on SiO2. *Nature nanotechnology* **3**, 206-209 (2008).

4 Lee, C., Wei, X., Kysar, J. W. & Hone, J. Measurement of the elastic properties and intrinsic strength of monolayer graphene. *Science* **321**, 385-388 (2008).

5 Geim, A. K. Graphene: status and prospects. *Science* **324**, 1530-1534 (2009).

6 Jurewicz, I. *et al.* Insulator-Conductor Type Transitions in Graphene-Modified Silver Nanowire Networks: A Route to Inexpensive Transparent Conductors. *Advanced Functional Materials* **24**, 7580-7587 (2014).

7 Ghosh, S. *et al.* Dimensional crossover of thermal transport in few-layer graphene. *Nature materials* **9**, 555-558 (2010).

8 Allen, M. J., Tung, V. C. & Kaner, R. B. Honeycomb carbon: a review of graphene. *Chem Rev* **110**, 132-145 (2009).

9 Novoselov, K. S. *et al.* Electronic properties of graphene. *physica status solidi (b)* **244**, 4106-4111, (2007).

10 Allen, M. J., Tung, V. C. & Kaner, R. B. Honeycomb carbon: a review of graphene. *Chem Rev* **110**, 132-145, (2010).

11 Peschel, G. (2011). Carbon-Carbon bonds: Hybridization.

12 Kvashnin, A. G., Chernozatonskii, L. A., Yakobson, B. I. & Sorokin, P. B. Phase diagram of quasi-two-dimensional carbon, from graphene to diamond. *Nano Lett* **14**, 676-681 (2014).

13 Paulus, G. L., Wang, Q. H. & Strano, M. S. Covalent electron transfer chemistry of graphene with diazonium salts. *Accounts of chemical research* **46**, 160-170 (2012).

14 Castro Neto, A. H., Guinea, F., Peres, N. M. R., Novoselov, K. S. & Geim, A. K. The electronic properties of graphene. *Reviews of Modern Physics* **81**, 109-162, doi:10.1103/RevModPhys.81.109 (2009).

15 Palacios, T., Hsu, A. & Wang, H. Applications of graphene devices in RF communications. *IEEE Communications Magazine* **48**, 122-128, (2010).

16 Jin, Z. *et al.* Click Chemistry on Solution-Dispersed Graphene and Monolayer CVD Graphene. *Chemistry of Materials* **23**, 3362-3370, (2011).

17 Ritter, K. A. & Lyding, J. W. The influence of edge structure on the electronic properties of graphene quantum dots and nanoribbons. *Nature materials* **8**, 235-242 (2009).

18 Yu, Q. *et al.* Control and characterization of individual grains and grain boundaries in graphene grown by chemical vapour deposition. *Nature materials* **10**, 443-449 (2011).

19 Wang, X. N-doping of graphene through electrothermal reactions with ammonia (vol 324, pg 768, 2009). *Science* **329**, 1467-1467 (2010).

20 Enoki, T., Fujii, S. & Takai, K. Zigzag and armchair edges in graphene. *Carbon* **50**, 3141-3145, (2012).

21 Jia, X., Campos-Delgado, J., Terrones, M., Meunier, V. & Dresselhaus, M. S. Graphene edges: a review of their fabrication and characterization. *Nanoscale* **3**, 86-95, (2011).

22 Koskinen, P., Malola, S. & Häkkinen, H. Evidence for graphene edges beyond zigzag and armchair. *Phys Rev B* **80**, 073401 (2009).

23 Kim, K. S. *et al.* Large-scale pattern growth of graphene films for stretchable transparent electrodes. *Nature* **457**, 706-710 (2009).
24 Losurdo, M., Giangregorio, M. M., Capezzuto, P. & Bruno, G. Graphene CVD growth on copper and nickel: role of hydrogen in kinetics and structure. *Physical Chemistry Chemical Physics* **13**, 20836-20843 (2011).
25 Stankovich, S. *et al.* Synthesis of graphene-based nanosheets via chemical reduction of exfoliated graphite oxide. *Carbon* **45**, 1558-1565 (2007).
26 Reina, A. *et al.* Large area, few-layer graphene films on arbitrary substrates by chemical vapor deposition. *Nano Lett* **9**, 30-35, (2009).
27 Novoselov, K. S. *et al.* Electric field effect in atomically thin carbon films. *Science* **306**, 666-669 (2004).
28 Dreyer, D. R., Ruoff, R. S. & Bielawski, C. W. From conception to realization: an historial account of graphene and some perspectives for its future. *Angewandte Chemie International Edition* **49**, 9336-9344 (2010).
29 Stoller, M. D., Park, S., Zhu, Y., An, J. & Ruoff, R. S. Graphene-based ultracapacitors. *Nano Lett* **8**, 3498-3502, (2008).
30 Kim, K. S. *et al.* Large-scale pattern growth of graphene films for stretchable transparent electrodes. *Nature* **457**, 706-710, (2009).
31 Li, X., Cai, W., Colombo, L. & Ruoff, R. S. Evolution of graphene growth on Ni and Cu by carbon isotope labeling. *Nano Lett* **9**, 4268-4272 (2009).
32 Li, X. *et al.* Large-area synthesis of high-quality and uniform graphene films on copper foils. *Science* **324**, 1312-1314 (2009).
33 Bae, S. *et al.* Roll-to-roll production of 30-inch graphene films for transparent electrodes. *Nature nanotechnology* **5**, 574-578 (2010).
34 Si, Y. & Samulski, E. T. Synthesis of water soluble graphene. *Nano Lett* **8**, 1679-1682 (2008).
35 Wang, G. *et al.* Facile synthesis and characterization of graphene nanosheets. *The Journal of Physical Chemistry C* **112**, 8192-8195 (2008).
36 Decker, R. *et al.* Local electronic properties of graphene on a BN substrate via scanning tunneling microscopy. *Nano Lett* **11**, 2291-2295, (2011).
37 Decker, R. *et al.* Local electronic properties of graphene on a BN substrate via scanning tunneling microscopy. *Nano Lett* **11**, 2291-2295 (2011).
38 Dean, C. *et al.* Boron nitride substrates for high-quality graphene electronics. *Nature nanotechnology* **5**, 722-726 (2010).
39 Ando, T. The electronic properties of graphene and carbon nanotubes. *NPG Asia Materials* **1**, 17-21 (2009).
40 Lu, G., Yu, K., Wen, Z. & Chen, J. Semiconducting graphene: converting graphene from semimetal to semiconductor. *Nanoscale* **5**, 1353-1368 (2013).
41 Rafiee, M. A. *et al.* Enhanced mechanical properties of nanocomposites at low graphene content. *Acs Nano* **3**, 3884-3890 (2009).
42 Frank, I. W., Tanenbaum, D. M., van der Zande, A. M. & McEuen, P. L. Mechanical properties of suspended graphene sheets. *Journal of Vacuum Science & Technology B: Microelectronics and Nanometer Structures* **25**, 2558, (2007).
43 Lee, C., Wei, X., Kysar, J. W. & Hone, J. Measurement of the elastic properties and intrinsic strength of monolayer graphene. *Science* **321**, 385-388, (2008).
44 Liang, J. *et al.* Molecular-level dispersion of graphene into poly (vinyl alcohol) and effective reinforcement of their nanocomposites. *Advanced Functional Materials* **19**, 2297-2302 (2009).
45 Gong, L. *et al.* Interfacial stress transfer in a graphene monolayer nanocomposite. *Advanced Materials* **22**, 2694-2697, (2010).
46 Zhao, X., Zhang, Q., Chen, D. & Lu, P. Enhanced mechanical properties of graphene-based poly (vinyl alcohol) composites. *Macromolecules* **43**, 2357-2363 (2010).

47 Nair, R. *et al.* Fine structure constant defines visual transparency of graphene. *Science* **320**, 1308-1308 (2008).
48 Balandin, A. A. Thermal properties of graphene and nanostructured carbon materials. *Nature materials* **10**, 569-581 (2011).
49 Cahill, D. G. Thermal conductivity measurement from 30 to 750 K: the 3ω method. *Review of scientific instruments* **61**, 802-808 (1990).
50 Lee, S., Choi, S.-S., Li, S., and & Eastman, J. Measuring thermal conductivity of fluids containing oxide nanoparticles. *Journal of Heat Transfer* **121**, 280-289 (1999).
51 Crank, J. & Nicolson, P. in *Mathematical Proceedings of the Cambridge Philosophical Society.* 50-67 (Cambridge Univ Press).
52 Fuhrer, M. S., Lau, C. N. & MacDonald, A. H. Graphene: materially better carbon. *MRS Bulletin* **35**, 289-295 (2010).
53 Wang, X. *et al.* N-doping of graphene through electrothermal reactions with ammonia. *Science* **324**, 768-771 (2009).
54 McEvoy, N., Nolan, H., Kumar, N. A., Hallam, T. & Duesberg, G. S. Functionalisation of graphene surfaces with downstream plasma treatments. *Carbon* **54**, 283-290 (2013).
55 Chabi, S., Peng, C., Yang, Z., Xia, Y. & Zhu, Y. Three dimensional (3D) flexible graphene foam/polypyrrole composite: towards highly efficient supercapacitors. *RSC Advances* **5**, 3999-4008 (2015).
56 Liu, H., Liu, Y. & Zhu, D. Chemical doping of graphene. *Journal of Materials Chemistry* **21**, 3335-3345 (2011).
57 Yu, Y.-J. *et al.* Tuning the graphene work function by electric field effect. *Nano Lett* **9**, 3430-3434 (2009).
58 Qu, L., Liu, Y., Baek, J.-B. & Dai, L. Nitrogen-doped graphene as efficient metal-free electrocatalyst for oxygen reduction in fuel cells. *Acs Nano* **4**, 1321-1326 (2010).
59 Zheng, Y., Jiao, Y., Ge, L., Jaroniec, M. & Qiao, S. Z. Two-Step Boron and Nitrogen Doping in Graphene for Enhanced Synergistic Catalysis. *Angew Chem Int Ed Engl* **125**, 3192-3198 (2013).
60 Ai, W. *et al.* Nitrogen and Sulfur Codoped Graphene: Multifunctional Electrode Materials for High-Performance Li-Ion Batteries and Oxygen Reduction Reaction. *Advanced Materials* **26**, 6186-6192 (2014).
61 Wang, Z., Hu, H. & Zeng, H. The electronic properties of graphene nanoribbons with boron/nitrogen codoping. *Applied Physics Letters* **96**, 243110 (2010).
62 Nourbakhsh, A. *et al.* Bandgap opening in oxygen plasma-treated graphene. *Nanotechnology* **21**, 435203 (2010).
63 Chen, Z. *et al.* Three-dimensional flexible and conductive interconnected graphene networks grown by chemical vapour deposition. *Nature materials* **10**, 424-428 (2011).
64 Wu, Y. *et al.* High-frequency, scaled graphene transistors on diamond-like carbon. *Nature* **472**, 74-78 (2011).
65 Fowler, J. D. *et al.* Practical chemical sensors from chemically derived graphene. *Acs Nano* **3**, 301-306 (2009).
66 Palacios, T., Hsu, A. & Wang, H. Applications of graphene devices in RF communications. *Communications Magazine, IEEE* **48**, 122-128 (2010).
67 Wang, X., Zhi, L. & Müllen, K. Transparent, conductive graphene electrodes for dye-sensitized solar cells. *Nano Lett* **8**, 323-327 (2008).
68 Zhu, Y. *et al.* Graphene and graphene oxide: synthesis, properties, and applications. *Advanced Materials* **22**, 3906-3924, doi:10.1002/adma.201001068 (2010).
69 Weber, C. M. *et al.* Graphene-based optically transparent electrodes for spectroelectrochemistry in the UV-Vis region. *Small* **6**, 184-189, (2010).
70 Wang, H. *et al.* Graphene-wrapped sulfur particles as a rechargeable lithium–sulfur battery cathode material with high capacity and cycling stability. *Nano Lett* **11**, 2644-2647 (2011).

71 Gwon, H. *et al.* Flexible energy storage devices based on graphene paper. *Energ Environ Sci* **4**, 1277-1283 (2011).
72 Pumera, M. Electrochemistry of graphene: new horizons for sensing and energy storage. *Chem Rec* **9**, 211-223, (2009).
73 Aricò, A. S., Bruce, P., Scrosati, B., Tarascon, J.-M. & Van Schalkwijk, W. Nanostructured materials for advanced energy conversion and storage devices. *Nature materials* **4**, 366-377 (2005).
74 Guo, Y.-G., Hu, J.-S. & Wan, L.-J. Nanostructured Materials for Electrochemical Energy Conversion and Storage Devices (vol 20, pg 2878, 2008). *Advanced Materials* **20**, 4384-4384 (2008).
75 Song, M.-K., Park, S., Alamgir, F. M., Cho, J. & Liu, M. Nanostructured electrodes for lithium-ion and lithium-air batteries: the latest developments, challenges, and perspectives. *Materials Science and Engineering: R: Reports* **72**, 203-252 (2011).
76 Holmberg, S., Perebikovsky, A., Kulinsky, L. & Madou, M. 3-D Micro and Nano Technologies for Improvements in Electrochemical Power Devices. *Micromachines* **5**, 171-203 (2014).
77 Long, J. W., Dunn, B., Rolison, D. R. & White, H. S. Three-dimensional battery architectures. *Chem Rev* **104**, 4463-4492 (2004).
78 Arthur, T. S. *et al.* Three-dimensional electrodes and battery architectures. *MRS Bulletin* **36**, 523-531 (2011).
79 Liu, Y. *et al.* Architecturing hierarchical function layers on self-assembled viral templates as 3D nano-array electrodes for integrated Li-ion microbatteries. *Nano Lett* **13**, 293-300 (2012).
80 Dong, X.-C. *et al.* 3D graphene–cobalt oxide electrode for high-performance supercapacitor and enzymeless glucose detection. *Acs Nano* **6**, 3206-3213 (2012).
81 Wilson, J. R. *et al.* Three-dimensional reconstruction of a solid-oxide fuel-cell anode. *Nature materials* **5**, 541-544 (2006).
82 Wang, H., Sun, K., Tao, F., Stacchiola, D. J. & Hu, Y. H. 3D Honeycomb-Like Structured Graphene and Its High Efficiency as a Counter-Electrode Catalyst for Dye-Sensitized Solar Cells. *Angew Chem Int Ed Engl* **125**, 9380-9384 (2013).
83 Chabi, S., Peng, C., Hu, D. & Zhu, Y. Ideal Three-Dimensional Electrode Structures for Electrochemical Energy Storage. *Advanced Materials* **26**, 2440-2445 (2014).
84 Ramos-Fernández, J. M., Martínez-Escandell, M. & Rodríguez-Reinoso, F. Production of binderless activated carbon monoliths by KOH activation of carbon mesophase materials. *Carbon* **46**, 384-386, (2008).
85 Reddy, A. L. M., Gowda, S. R., Shaijumon, M. M. & Ajayan, P. M. Hybrid nanostructures for energy storage applications. *Advanced Materials* **24**, 5045-5064 (2012).
86 Chmiola, J., Largeot, C., Taberna, P. L., Simon, P. & Gogotsi, Y. Monolithic Carbide-Derived Carbon Films for Micro-Supercapacitors. *Science* **328**, 480-483, doi:DOI 10.1126/science.1184126 (2010).
87 Heon, M. *et al.* Continuous carbide-derived carbon films with high volumetric capacitance. *Energ Environ Sci* **4**, 135-138, (2011).
88 Hu, Y. S. *et al.* Synthesis of hierarchically porous carbon monoliths with highly ordered microstructure and their application in rechargeable lithium batteries with high-rate capability. *Advanced Functional Materials* **17**, 1873-1878, doi:DOI 10.1002/adfm.200601152 (2007).
89 Ruiz, V. *et al.* An activated carbon monolith as an electrode material for supercapacitors. *Carbon* **47**, 195-200, doi:DOI 10.1016/j.carbon.2008.09.048 (2009).
90 Chmiola, J., Largeot, C., Taberna, P.-L., Simon, P. & Gogotsi, Y. Monolithic carbide-derived carbon films for micro-supercapacitors. *Science* **328**, 480-483 (2010).
91 Hu, Y. S. *et al.* Synthesis of hierarchically porous carbon monoliths with highly ordered microstructure and their application in rechargeable lithium batteries with high-rate capability. *Advanced Functional Materials* **17**, 1873-1878 (2007).

92 Garcia-Gomez, A., Miles, P., Centeno, T. & Rojo, J. Why carbon monoliths are better supercapacitor electrodes than compacted pellets. *Electrochemical and Solid-State Letters* **13**, A112-A114 (2010).
93 Conway, B. E. Electrochemical supercapacitors. (1999).
94 Chen, Z. *et al.* Three-dimensional flexible and conductive interconnected graphene networks grown by chemical vapour deposition. *Nat Mater* **10**, 424-428, (2011).
95 Fan, Z. *et al.* A Three-Dimensional Carbon Nanotube/Graphene Sandwich and Its Application as Electrode in Supercapacitors. *Advanced Materials* **22**, 3723-3728 (2010).
96 Wang, W. *et al.* Three dimensional few layer graphene and carbon nanotube foam architectures for high fidelity supercapacitors. *Nano Energy* **2**, 294-303 (2013).
97 Ye, S. B., Feng, J. C. & Wu, P. Y. Deposition of Three-Dimensional Graphene Aerogel on Nickel Foam as a Binder-Free Supercapacitor Electrode. *ACS Appl Mater Interfaces* **5**, 7122-7129, (2013).
98 Xu, Y. X. *et al.* Flexible Solid-State Supercapacitors Based on Three-Dimensional Graphene Hydrogel Films. *Acs Nano* **7**, 4042-4049, (2013).
99 Zhang, H., Yu, X. & Braun, P. V. Three-dimensional bicontinuous ultrafast-charge and -discharge bulk battery electrodes. *Nat Nano* **6**, 277-281, (2011).
100 Fan, L. Z. *et al.* High electroactivity of polyaniline in supercapacitors by using a hierarchically porous carbon monolith as a support. *Advanced Functional Materials* **17**, 3083-3087 (2007).
101 Chen, M. S., Wu, T. B. & Wu, J. M. Effect of textured LaNiO3 electrode on the fatigue improvement of Pb (Zr0. 53Ti0. 47) O3 thin films. *Appl Phys Lett* **68**, 1430-1432 (1996).
102 Wilson, M. S. & Gottesfeld, S. Thin-film catalyst layers for polymer electrolyte fuel cell electrodes. *Journal of Applied Electrochemistry* **22**, 1-7 (1992).
103 Morita, T., Kurosawa, M. K. & Higuchi, T. A cylindrical micro ultrasonic motor using PZT thin film deposited by single process hydrothermal method (/spl phi/2.4 mm, L= 10 mm stator transducer). *Ultrasonics, Ferroelectrics, and Frequency Control, IEEE Transactions on* **45**, 1178-1187 (1998).
104 Bai, X. X. *et al.* In situ polymerization and characterization of grafted poly (3,4-ethylenedioxythiophene)/multiwalled carbon nanotubes composite with high electrochemical performances. *Electrochimica Acta* **87**, 394-400, (2013).
105 Peng, C., Jin, J. & Chen, G. Z. A comparative study on electrochemical co-deposition and capacitance of composite films of conducting polymers and carbon nanotubes. *Electrochimica Acta* **53**, 525-537, (2007).
106 Chen, K. W., Chen, L. B., Chen, Y. Q., Bai, H. & Li, L. Three-dimensional porous graphene-based composite materials: electrochemical synthesis and application. *Journal of Materials Chemistry* **22**, 20968-20976, (2012).
107 Chabi, S., Peng, C., Hu, D. & Zhu, Y. Q. Ideal Three-Dimensional Electrode Structures for Electrochemical Energy Storage. *Advanced Materials* **26**, 2440-2445, (2014).
108 Lu, X. J. *et al.* Polypyrrole/carbon nanotube nanocomposite enhanced the electrochemical capacitance of flexible graphene film for supercapacitors. *Journal of Power Sources* **197**, 319-324, (2012).
109 Huang, Y. *et al.* Self-assembly of ultrathin porous NiO nanosheets/graphene hierarchical structure for high-capacity and high-rate lithium storage. *Journal of Materials Chemistry* **22**, 2844-2847, doi:Doi 10.1039/C2jm15865e (2012).
110 Yang, S. *et al.* Bottom-up approach toward single-crystalline VO2-graphene ribbons as cathodes for ultrafast lithium storage. *Nano Lett* **13**, 1596-1601 (2013).
111 Huang, Y. S. *et al.* Assembly of Tin Oxide/Graphene Nanosheets into 3D Hierarchical Frameworks for High-Performance Lithium Storage. *Chemsuschem* **6**, 1510-1515, (2013).
112 Meyer, J. C. *et al.* The structure of suspended graphene sheets. *Nature* **446**, 60-63, (2007).
113 Pacilé, D., Meyer, J. C., Girit, C. O. & Zettl, A. The two-dimensional phase of boron nitride: Few-atomic-layer sheets and suspended membranes. *Appl Phys Lett* **92**, 133107, (2008).

114 Naguib, M. *et al.* Two-dimensional nanocrystals produced by exfoliation of Ti3 AlC2. *Advanced Materials* **23**, 4248-4253, doi:10.1002/adma.201102306 (2011).
115 Naguib, M. *et al.* Two-dimensional transition metal carbides. *Acs Nano* **6**, 1322-1331 (2012).
116 Priede, L. M. & Meza-Montes, L. Electron-Energy-Loss Spectra of Free-Standing Silicene. *arXiv preprint arXiv:1405.4204* (2014).
117 Kunets, V. P. *et al.* Electron transport in quantum dot chains: Dimensionality effects and hopping conductance. *J Appl Phys* **113**, 183709, (2013).
118 Pakdel, A., Zhi, C., Bando, Y. & Golberg, D. Low-dimensional boron nitride nanomaterials. *Materials Today* **15**, 256-265, (2012).
119 Weitzel, C. E. *et al.* Silicon carbide high-power devices. *Electron Devices, IEEE Transactions on* **43**, 1732-1741 (1996).
120 Yang, Y. *et al.* Monocrystalline silicon carbide nanoelectromechanical systems. *Appl Phys Lett* **78**, 162-164 (2001).
121 Edmond, J. A. (Google Patents, 1991).
122 Singh, R. & Palmour, J. W. (Google Patents, 1998).
123 Edgar, J., Yu, Z., Smith, D. J., Chaudhuri, J. & Cheng, X. X-ray diffraction and high resolution transmission electron microscopy of 3C-SiC/AlN/6H-SiC (0001). *Journal of electronic materials* **26**, 1389-1393 (1997).
124 Long, C., Ustin, S. A. & Ho, W. Structural defects in 3C–SiC grown on Si by supersonic jet epitaxy. *J Appl Phys* **86**, 2509, (1999).
125 Wieligor, M., Wang, Y. & Zerda, T. W. Raman spectra of silicon carbide small particles and nanowires. *Journal of Physics: Condensed Matter* **17**, 2387-2395, doi:10.1088/0953-8984/17/15/010 (2005).
126 Zhu, Y. *et al.* SiC–SiO x heterojunctions in nanowires. *Journal of Materials Chemistry* **9**, 3173-3178 (1999).
127 Komarov, S., Kuznetsov, D., Terakado, O., Levina, V. & Hirasawa, M. Characterization of Si-based nanoparticulates produced by carbothermic reduction of silica-containing slag. *Materials transactions* **46**, 3044-3050 (2005).
128 Huda, M. N., Yan, Y. & Al-Jassim, M. M. On the existence of Si–C double bonded graphene-like layers. *Chemical Physics Letters* **479**, 255-258, doi:10.1016/j.cplett.2009.08.028 (2009).
129 Lin, X. *et al.* Optical and electronic properties of two dimensional graphitic silicon carbide. *arXiv preprint arXiv:1205.5404* (2012).
130 Zhang, H., Ding, W., He, K. & Li, M. Synthesis and characterization of crystalline silicon carbide nanoribbons. *Nanoscale Res Lett* **5**, 1264-1271 (2010).
131 Wei, G. *et al.* Large-Scale Synthesis and Photoluminescence Properties of Aligned Multicore SiC–SiO2 Nanocables. *J Nanosci Nanotechno* **10**, 1964-1968 (2010).
132 Powell, J. A. Crystal Growth of 2H Silicon Carbide. *J Appl Phys* **40**, 4660, (1969).
133 Choi, H.-J., Seong, H.-K., Lee, J.-C. & Sung, Y.-M. Growth and modulation of silicon carbide nanowires. *Journal of crystal growth* **269**, 472-478 (2004).
134 Yao, Y., Lee, S. & Li, F. Direct synthesis of 2H–SiC nanowhiskers. *Chemical Physics Letters* **381**, 628-633 (2003).
135 Li, X. *et al.* Synthesis of nanometre silicon carbide whiskers from binary carbonaceous silica aerogels. *Carbon* **39**, 159-165 (2001).
136 Torrisi, L. *et al.* Single crystal silicon carbide detector of emitted ions and soft x rays from power laser-generated plasmas. *J Appl Phys* **105**, 123304 (2009).
137 Wang, F.-L., Zhang, L.-Y. & Zhang, Y.-F. SiC nanowires synthesized by rapidly heating a mixture of SiO and arc-discharge plasma pretreated carbon black. *Nanoscale Res Lett* **4**, 153-156 (2009).
138 Hu, J., Odom, T. W. & Lieber, C. M. Chemistry and physics in one dimension: synthesis and properties of nanowires and nanotubes. *Accounts of chemical research* **32**, 435-445 (1999).

139 Zivkovic, I. & Murk, A. Characterization of open cell SIC foam material. *Progress In Electromagnetics Research B* **38**, 225-239 (2012).
140 Ren, F., Zhai, G., Ma, Z., Chen, X. & Volinsky, A. A. Microstructure and quality of SiC foam filters for casting. *Journal of Ceramic Processing Research* **12**, 691-694 (2011).
141 Li, Z., Zhang, J., Meng, A. & Guo, J. Large-area highly-oriented SiC nanowire arrays: synthesis, Raman, and photoluminescence properties. *The Journal of Physical Chemistry B* **110**, 22382-22386 (2006).
142 Bao, X., Nangrejo, M. & Edirisinghe, M. Preparation of silicon carbide foams using polymeric precursor solutions. *Journal of materials science* **35**, 4365-4372 (2000).
143 Peng, H., Fan, Z. & Evans, J. Factors affecting the microstructure of a fine ceramic foam. *Ceramics international* **26**, 887-895 (2000).
144 Sun, H., Xu, Z. & Gao, C. Multifunctional, ultra-flyweight, synergistically assembled carbon aerogels. *Advanced Materials* **25**, 2554-2560, (2013).
145 Xu, M., Liang, T., Shi, M. & Chen, H. Graphene-like two-dimensional materials. *Chemical reviews* **113**, 3766-3798 (2013).
146 Geim, A. & Grigorieva, I. Van der Waals heterostructures. *Nature* **499**, 419-425 (2013).
147 Miyamoto, Y. & Yu, B. D. Computational designing of graphitic silicon carbide and its tubular forms. *Appl Phys Lett* **80**, 586, (2002).
148 Mélinon, P., Masenelli, B., Tournus, F. & Perez, A. Playing with carbon and silicon at the nanoscale. *Nature materials* **6**, 479-490 (2007).
149 Li, P., Zhou, R. & Zeng, X. C. The search for the most stable structures of silicon–carbon monolayer compounds. *Nanoscale* **6**, 11685-11691 (2014).
150 Bekaroglu, E., Topsakal, M., Cahangirov, S. & Ciraci, S. First-principles study of defects and adatoms in silicon carbide honeycomb structures. *Phys Rev B* **81**, 075433 (2010).
151 Yu, M., Jayanthi, C. S. & Wu, S. Y. Theoretical predictions of a bucky-diamond SiC cluster. *Nanotechnology* **23**, 235705, (2012).
152 Gao, B.-L. *et al.* Band-gap modulation of graphane-like SiC nanoribbons under uniaxial elastic strain. *Physics Letters A* **378**, 565-569 (2014).
153 Lin, X. *et al.* Ab initio study of electronic and optical behavior of two-dimensional silicon carbide. *Journal of Materials Chemistry C* **1**, 2131-2135 (2013).
154 Yu, M., Jayanthi, C. S. & Wu, S. Y. Geometric and electronic structures of graphitic-like and tubular silicon carbides: Ab-initio studies. *Phys Rev B* **82**, (2010).
155 Kara, A. *et al.* A review on silicene — New candidate for electronics. *Surface Science Reports* **67**, 1-18, (2012).
156 Kara, A. *et al.* A review on silicene—new candidate for electronics. *Surface Science Reports* **67**, 1-18 (2012).
157 Syväjärvi, M., Yakimova, R. & Janzén, E. Cross-sectional cleavages of SiC for evaluation of epitaxial layers. *Journal of crystal growth* **208**, 409-415 (2000).
158 Avramov, P. V. *et al.* Intrinsic edge asymmetry in narrow zigzag hexagonal heteroatomic nanoribbons causes their subtle uniform curvature. *The Journal of Physical Chemistry Letters* **3**, 2003-2008 (2012).
159 Hwang, J.-Y., Kuo, C.-C., Chen, L.-C. & Chen, K.-H. Correlating defect density with carrier mobility in large-scaled graphene films: Raman spectral signatures for the estimation of defect density. *Nanotechnology* **21**, 465705 (2010).
160 Ponomarenko, L. *et al.* Effect of a high-κ environment on charge carrier mobility in graphene. *Phys Rev Lett* **102**, 206603 (2009).
161 <https://www.purdue.edu/ehps/rem/rs/sem.htm>
162 Goldstein, J. *et al. Scanning electron microscopy and X-ray microanalysis: a text for biologists, materials scientists, and geologists*. (Springer Science & Business Media, 2012).
163 Feng, Y. *et al.* Micro-CT characterization on porosity structure of 3D C f/SiC m composite. *Composites Part A: Applied Science and Manufacturing* **42**, 1645-1650 (2011).

164 Cullity, B. Elements of. *X-ray! Jiffraction* (1978).
165 http://barrett-group.mcgill.ca/tutorials/nanotechnology/nano02.htm
166 Meyer, J. C., Girit, C. O., Crommie, M. & Zettl, A. Imaging and dynamics of light atoms and molecules on graphene. *Nature* **454**, 319-322 (2008).
167 http://web.physics.ucsb.edu/~hhansma/biomolecules.htm
168 http://bwtek.com/raman-theory-of-raman-scattering/
169 Chae, S. J. *et al.* Synthesis of large-area graphene layers on poly-nickel substrate by chemical vapor deposition: wrinkle formation. *Adv. Mater* **21**, 2328-2333 (2009).
170 Sun, Z. *et al.* Growth of graphene from solid carbon sources. *Nature* **468**, 549-552 (2010).
171 Vlassiouk, I. *et al.* Role of hydrogen in chemical vapor deposition growth of large single-crystal graphene. *Acs Nano* **5**, 6069-6076 (2011).
172 Wang, Y. *et al.* Template effect in the competition between Haeckelite and graphene growth on Ni (111): Quantum chemical molecular dynamics simulations. *Journal of the American Chemical Society* **133**, 18837-18842 (2011).
173 Chae, S. J. *et al.* Synthesis of large-area graphene layers on poly-nickel substrate by chemical vapor deposition: wrinkle formation. *Advanced Materials* **21**, 2328-2333 (2009).
174 Yu, Q. *et al.* Graphene segregated on Ni surfaces and transferred to insulators. *Appl Phys Lett* **93**, 113103 (2008).
175 Al-Shurman, K. & Naseem, H. CVD Graphene Growth Mechanism on Nickel Thin Films.
176 Umair, A. & Raza, H. Controlled synthesis of bilayer graphene on nickel. *Nanoscale Res Lett* **7**, 1-5 (2012).
177 Park, H. J., Meyer, J., Roth, S. & Skákalová, V. Growth and properties of few-layer graphene prepared by chemical vapor deposition. *Carbon* **48**, 1088-1094 (2010).
178 Pirkle, A. *et al.* The effect of chemical residues on the physical and electrical properties of chemical vapor deposited graphene transferred to SiO2. *Appl Phys Lett* **99**, 122108 (2011).
179 Jiao, L., Zhang, L., Wang, X., Diankov, G. & Dai, H. Narrow graphene nanoribbons from carbon nanotubes. *Nature* **458**, 877-880 (2009).
180 Ferrari, A. C. & Robertson, J. Raman spectroscopy of amorphous, nanostructured, diamond–like carbon, and nanodiamond. *Philosophical Transactions of the Royal Society of London A: Mathematical, Physical and Engineering Sciences* **362**, 2477-2512 (2004).
181 Ferrari, A. *et al.* Raman spectrum of graphene and graphene layers. *Physical review letters* **97**, 187401 (2006).
182 Zheng, M. *et al.* Metal-catalyzed crystallization of amorphous carbon to graphene. *Appl Phys Lett* **96**, 063110 (2010).
183 Bao, Q. *et al.* Atomic-layer graphene as a saturable absorber for ultrafast pulsed lasers. *Advanced Functional Materials* **19**, 3077-3083 (2009).
184 Mecklenburg, M. *et al.* Aerographite: ultra lightweight, flexible nanowall, carbon microtube material with outstanding mechanical performance. *Advanced Materials* **24**, 3486-3490 (2012).
185 Worsley, M. A. *et al.* Properties of single-walled carbon nanotube-based aerogels as a function of nanotube loading. *Acta Materialia* **57**, 5131-5136 (2009).
186 Gutiérrez, M. C. *et al.* Biocompatible MWCNT scaffolds for immobilization and proliferation of E. coli. *Journal of Materials Chemistry* **17**, 2992-2995 (2007).
187 Ji, H. *et al.* Ultrathin graphite foam: a three-dimensional conductive network for battery electrodes. *Nano Lett* **12**, 2446-2451 (2012).
188 Worsley, M. A. *et al.* Synthesis of graphene aerogel with high electrical conductivity. *Journal of the American Chemical Society* **132**, 14067-14069 (2010).
189 Frackowiak, E. & Beguin, F. Carbon materials for the electrochemical storage of energy in capacitors. *Carbon* **39**, 937-950 (2001).
190 Miller, J. R., Outlaw, R. & Holloway, B. Graphene double-layer capacitor with ac line-filtering performance. *Science* **329**, 1637-1639 (2010).

191 Simon, P. & Gogotsi, Y. Materials for electrochemical capacitors. *Nature materials* **7**, 845-854 (2008).
192 Han, L., Karthikeyan, K., Anderson, M. A. & Gregory, K. B. Exploring the impact of pore size distribution on the performance of carbon electrodes for capacitive deionization. *J Colloid Interf Sci* **430**, 93-99 (2014).
193 Candelaria, S. L. *et al.* Nanostructured carbon for energy storage and conversion. *Nano Energy* **1**, 195-220 (2012).
194 Das, A., Chakraborty, B. & Sood, A. Raman spectroscopy of graphene on different substrates and influence of defects. *Bulletin of Materials Science* **31**, 579-584 (2008).
195 Ferrari, A. C. Raman spectroscopy of graphene and graphite: disorder, electron–phonon coupling, doping and nonadiabatic effects. *Solid state communications* **143**, 47-57 (2007).
196 Balducci, A. *et al.* High temperature carbon–carbon supercapacitor using ionic liquid as electrolyte. *Journal of Power Sources* **165**, 922-927 (2007).
197 Lang, J.-W., Kong, L.-B., Wu, W.-J., Luo, Y.-C. & Kang, L. Facile approach to prepare loose-packed NiO nano-flakes materials for supercapacitors. *Chem Commun (Camb)*, 4213-4215 (2008).
198 Hong, M. S., Lee, S. H. & Kim, S. W. Use of KCl aqueous electrolyte for 2 V manganese oxide/activated carbon hybrid capacitor. *Electrochemical and Solid-State Letters* **5**, A227-A230 (2002).
199 Meng, C., Liu, C., Chen, L., Hu, C. & Fan, S. Highly flexible and all-solid-state paperlike polymer supercapacitors. *Nano Lett* **10**, 4025-4031 (2010).
200 Snook, G. A., Kao, P. & Best, A. S. Conducting-polymer-based supercapacitor devices and electrodes. *Journal of Power Sources* **196**, 1-12 (2011).
201 Xi, K. *et al.* Binder free three-dimensional sulphur/few-layer graphene foam cathode with enhanced high-rate capability for rechargeable lithium sulphur batteries. *Nanoscale* **6**, 5746-5753 (2014).
202 Johne, C., Fritzsch, R. & Ignaszak, A. Three-Dimensionally Ordered Polypyrrole Electrode: Electrochemical Study on Capacity and Degradation Process. *Electroanal* (2014).
203 Rolison, D. R. *et al.* Multifunctional 3D nanoarchitectures for energy storage and conversion. *Chemical Society Reviews* **38**, 226-252 (2009).
204 Ji, J. *et al.* Nanoporous Ni (OH) 2 thin film on 3D ultrathin-graphite foam for asymmetric supercapacitor. *Acs Nano* **7**, 6237-6243 (2013).
205 Jiang, H., Lee, P. S. & Li, C. 3D carbon based nanostructures for advanced supercapacitors. *Energ Environ Sci* **6**, 41-53 (2013).
206 Du, F. *et al.* Preparation of tunable 3D pillared carbon nanotube–graphene networks for high-performance capacitance. *Chemistry of Materials* **23**, 4810-4816 (2011).
207 Cao, X. *et al.* Preparation of novel 3D graphene networks for supercapacitor applications. *Small* **7**, 3163-3168 (2011).
208 Kuilla, T. *et al.* Recent advances in graphene based polymer composites. *Progress in polymer science* **35**, 1350-1375 (2010).
209 Huang, X., Qi, X., Boey, F. & Zhang, H. Graphene-based composites. *Chemical Society Reviews* **41**, 666-686 (2012).
210 Peng, C., Zhang, S., Jewell, D. & Chen, G. Z. Carbon nanotube and conducting polymer composites for supercapacitors. *Progress in Natural Science* **18**, 777-788 (2008).
211 Al-Saleh, M. H. & Sundararaj, U. A review of vapor grown carbon nanofiber/polymer conductive composites. *Carbon* **47**, 2-22 (2009).
212 Hughes, M., Chen, G. Z., Shaffer, M. S., Fray, D. J. & Windle, A. H. Electrochemical capacitance of a nanoporous composite of carbon nanotubes and polypyrrole. *Chemistry of Materials* **14**, 1610-1613 (2002).
213 Ma, S.-B. *et al.* Electrochemical properties of manganese oxide coated onto carbon nanotubes for energy-storage applications. *Journal of Power Sources* **178**, 483-489 (2008).

214 Hou, Y., Cheng, Y., Hobson, T. & Liu, J. Design and synthesis of hierarchical MnO2 nanospheres/carbon nanotubes/conducting polymer ternary composite for high performance electrochemical electrodes. *Nano Lett* **10**, 2727-2733 (2010).
215 Wang, J., Yang, J., Xie, J. & Xu, N. A novel conductive polymer–sulfur composite cathode material for rechargeable lithium batteries. *Advanced Materials* **14**, 963-965 (2002).
216 Skotheim, T. A. *Handbook of conducting polymers*. (CRC press, 1997).
217 Chang, H.-H., Chang, C.-K., Tsai, Y.-C. & Liao, C.-S. Electrochemically synthesized graphene/polypyrrole composites and their use in supercapacitor. *Carbon* **50**, 2331-2336 (2012).
218 Sahoo, S., Dhibar, S. & Das, C. Facile synthesis of polypyrrole nanofiber and its enhanced electrochemical performances in different electrolytes. *Express Polymer Letters* **6**, 965-974 (2012).
219 Ansari, R. Polypyrrole conducting electroactive polymers: synthesis and stability studies. *Journal of Chemistry* **3**, 186-201 (2006).
220 Sadki, S., Schottland, P., Brodie, N. & Sabouraud, G. The mechanisms of pyrrole electropolymerization. *Chemical Society Reviews* **29**, 283-293 (2000).
221 Biswas, S. & Drzal, L. T. Multilayered nanoarchitecture of graphene nanosheets and polypyrrole nanowires for high performance supercapacitor electrodes. *Chemistry of Materials* **22**, 5667-5671 (2010).
222 Stoller, M. D., Park, S., Zhu, Y., An, J. & Ruoff, R. S. Graphene-based ultracapacitors. *Nano Lett* **8**, 3498-3502 (2008).
223 Mani, A. *et al.* Graphene-Polypyrrole Nanocomposite: An Ideal Electroactive Material for High Performance Supercapacitors. *Graphene Materials: Fundamentals and Emerging Applications*, 225-244 (2015).
224 Zhang, D. *et al.* Enhanced capacitance and rate capability of graphene/polypyrrole composite as electrode material for supercapacitors. *Journal of Power Sources* **196**, 5990-5996 (2011).
225 Yu, G., Xie, X., Pan, L., Bao, Z. & Cui, Y. Hybrid nanostructured materials for high-performance electrochemical capacitors. *Nano Energy* **2**, 213-234, doi:10.1016/j.nanoen.2012.10.006 (2013).
226 Abdullah, H. S. Electrochemical polymerization and Raman study of polypyrrole and polyaniline thin films. *International Journal of Physical Sciences* **7**, 5468-5476 (2012).
227 Dong, X. *et al.* Doping Single-Layer Graphene with Aromatic Molecules. *Small* **5**, 1422-1426 (2009).
228 Bose, S. *et al.* In-situ synthesis and characterization of electrically conductive polypyrrole/graphene nanocomposites. *Polymer* **51**, 5921-5928 (2010).
229 Iqbal, M., Singh, A. K., Iqbal, M. & Eom, J. Raman fingerprint of doping due to metal adsorbates on graphene. *Journal of Physics: Condensed Matter* **24**, 335301 (2012).
230 Casiraghi, C. Probing disorder and charged impurities in graphene by Raman spectroscopy. *physica status solidi (RRL)-Rapid Research Letters* **3**, 175-177 (2009).
231 Kalbac, M. *et al.* The influence of strong electron and hole doping on the Raman intensity of chemical vapor-deposition graphene. *Acs Nano* **4**, 6055-6063 (2010).
232 Yan, J. *et al.* Preparation of exfoliated graphite containing manganese oxides with high electrochemical capacitance by microwave irradiation. *Carbon* **47**, 3371-3374 (2009).
233 Jeong, H.-K. *et al.* Enhanced electric double layer capacitance of graphite oxide intercalated by poly (sodium 4-styrensulfonate) with high cycle stability. *Acs Nano* **4**, 1162-1166 (2010).
234 Si, Y. & Samulski, E. T. Exfoliated graphene separated by platinum nanoparticles. *Chemistry of Materials* **20**, 6792-6797 (2008).
235 Liu, T. *et al.* Polyaniline and polypyrrole pseudocapacitor electrodes with excellent cycling stability. *Nano letters* **14**, 2522-2527 (2014).

236 Zhang, Y. *et al.* Progress of electrochemical capacitor electrode materials: A review. *International journal of hydrogen energy* **34**, 4889-4899 (2009).
237 Yan, J. *et al.* Advanced asymmetric supercapacitors based on Ni (OH) 2/graphene and porous graphene electrodes with high energy density. *Advanced Functional Materials* **22**, 2632-2641 (2012).
238 Cheng, Y., Zhang, H., Lu, S., Varanasi, C. V. & Liu, J. Flexible asymmetric supercapacitors with high energy and high power density in aqueous electrolytes. *Nanoscale* **5**, 1067-1073 (2013).
239 Zhang, L. C. *et al.* Rice paper-derived 3D-porous carbon films for lithium-ion batteries. *Electrochimica Acta* **89**, 310-316, (2013).
240 El-Kady, M. F., Strong, V., Dubin, S. & Kaner, R. B. Laser scribing of high-performance and flexible graphene-based electrochemical capacitors. *Science* **335**, 1326-1330 (2012).
241 Basnayaka, P. A., Ram, M. K., Stefanakos, L. & Kumar, A. Graphene/polypyrrole nanocomposite as electrochemical supercapacitor electrode: electrochemical impedance studies. *Graphene* **2**, 81 (2013).
242 Bose, S., Kim, N. H., Kuila, T., Lau, K.-t. & Lee, J. H. Electrochemical performance of a graphene–polypyrrole nanocomposite as a supercapacitor electrode. *Nanotechnology* **22**, 295202 (2011).
243 Park, J. H., Ko, J. M., Park, O. O. & Kim, D.-W. Capacitance properties of graphite/polypyrrole composite electrode prepared by chemical polymerization of pyrrole on graphite fiber. *Journal of Power Sources* **105**, 20-25 (2002).
244 Singh, A. & Chandra, A. Graphite oxide/polypyrrole composite electrodes for achieving high energy density supercapacitors. *Journal of Applied Electrochemistry* **43**, 773-782 (2013).
245 Zhang, D. *et al.* Preparation of a Three-Dimensional Ordered Macroporous Carbon Nanotube/Polypyrrole Composite for Supercapacitors and Diffusion Modeling. *The Journal of Physical Chemistry C* **117**, 20446-20455 (2013).
246 Zhang, L. L. & Zhao, X. Carbon-based materials as supercapacitor electrodes. *Chemical Society Reviews* **38**, 2520-2531 (2009).
247 Wang, D.-W., Li, F. & Cheng, H.-M. Hierarchical porous nickel oxide and carbon as electrode materials for asymmetric supercapacitor. *Journal of Power Sources* **185**, 1563-1568 (2008).
248 Hughes, M. *et al.* Electrochemical capacitance of nanocomposite films formed by coating aligned arrays of carbon nanotubes with polypyrrole. *Advanced Materials* **14**, 382-385 (2002).
249 Park, K.-S. *et al.* Long-term, high-rate lithium storage capabilities of TiO 2 nanostructured electrodes using 3D self-supported indium tin oxide conducting nanowire arrays. *Energ Environ Sci* **4**, 1796-1801 (2011).
250 Jurewicz, K., Delpeux, S., Bertagna, V., Beguin, F. & Frackowiak, E. Supercapacitors from nanotubes/polypyrrole composites. *Chemical Physics Letters* **347**, 36-40 (2001).
251 Chen, Y., Zhang, X., Zhang, D., Yu, P. & Ma, Y. High performance supercapacitors based on reduced graphene oxide in aqueous and ionic liquid electrolytes. *Carbon* **49**, 573-580 (2011).
252 Chan, S., Khor, K. & Xia, Z. A complete polarization model of a solid oxide fuel cell and its sensitivity to the change of cell component thickness. *Journal of Power Sources* **93**, 130-140 (2001).
253 Genies, E., Syed, A. & Tsintavis, C. Electrochemical Study Of Polyaniline In Aqueous And Organic Medium. Redox And Kinetic Properties. *Molecular Crystals and Liquid Crystals* **121**, 181-186 (1985).
254 Sk, M. M., Yue, C. Y. & Jena, R. K. Facile growth of heparin-controlled porous polyaniline nanofiber networks and their application in supercapacitors. *RSC Advances* **4**, 5188-5197 (2014).
255 Casady, J. & Johnson, R. W. Status of silicon carbide (SiC) as a wide-bandgap semiconductor for high-temperature applications: A review. *Solid-State Electronics* **39**, 1409-1422 (1996).

256 Suyama, S., Kameda, T. & Itoh, Y. Development of high-strength reaction-sintered silicon carbide. *Diamond and related materials* **12**, 1201-1204 (2003).
257 Suwanmethanond, V. *et al.* Porous silicon carbide sintered substrates for high-temperature membranes. *Ind Eng Chem Res* **39**, 3264-3271 (2000).
258 Geim, A. K. & Novoselov, K. S. The rise of graphene. *Nature materials* **6**, 183-191 (2007).
259 Liu, Y. F. *et al.* Modular pathway engineering of Bacillus subtilis for improved N-acetylglucosamine production. *Metab Eng* **23**, 42-52 (2014).
260 Nakamura, D., Yamaguchi, S., Gunjishima, I., Hirose, Y. & Kimoto, T. Topographic study of dislocation structure in hexagonal SiC single crystals with low dislocation density. *Journal of crystal growth* **304**, 57-63 (2007).
261 Zhu, Y. Q. *et al.* Novel analgesic peptides from the tree frog of Hyla japonica. *Biochimie* **99C**, 38-43 (2014).
262 Li, T., Xu, L., Wang, L., Yang, L. & Qian, Y. Synthesis and characterization of 3C and 2H-SiC nanocrystals starting from SiO 2, C 2 H 5 OH and metallic Mg. *Journal of Alloys and Compounds* **484**, 341-346 (2009).
263 Chafai, M. *et al.* Raman scattering from LO phonon-plasmon coupled modes and Hall-effect in n-type silicon carbide 4H–SiC. *J Appl Phys* **90**, 5211, (2001).
264 Freitas Jr, J. & Moore, W. Optical Studies of Undoped and Doped Wide Bandgap Carbide and Nitride Semiconductors. *Brazilian journal of physics* **28**, 12-18 (1998).
265 Seo, W. S., Koumoto, K. & Aria, S. Morphology and Stacking Faults of β-Silicon Carbide Whisker Synthesized by Carbothermal Reduction. *Journal of the American Ceramic Society* **83**, 2584-2592 (2000).
266 Iwata, H., Lindefelt, U., Öberg, S. & Briddon, P. Stacking faults in silicon carbide. *Physica B: Condensed Matter* **340**, 165-170 (2003).
267 Miao, M. & Lambrecht, W. R. in *Materials science forum.* 351-354 (Trans Tech Publ).
268 Tang, C. *et al.* Growth of SiC nanorods prepared by carbon nanotubes-confined reaction. *Journal of crystal growth* **210**, 595-599 (2000).
269 Zhang, H.-F., Wang, C.-M. & Wang, L.-S. Helical crystalline SiC/SiO2 core-shell nanowires. *Nano letters* **2**, 941-944 (2002).
270 Hwang, H. J., Lee, K.-J., An, Y.-T., Choi, B.-H. & Seo, W.-S. Synthesis of β-silicon carbide nanofiber from an exfoliated graphite and amorphous silica. *Mater Chem Phys* **134**, 13-15, (2012).
271 Konishi, H., Tsuda, H., Mabuchi-Nakatani, H., Morii, K. & Okamura, K. in *Proc. 5th Int. Conf. on High Temperature Ceramic Matrix Composites (HTCMC-5).*
272 Liu, Y. *et al.* Three-dimensional network current collectors supported Si nanowires for lithium-ion battery applications. *Electrochimica Acta* **88**, 766-771, (2013).
273 Zhou, D. & Seraphin, S. Production of silicon carbide whiskers from carbon nanoclusters. *Chemical physics letters* **222**, 233-238 (1994).
274 Dai, H., Wong, E. W., Lu, Y. Z., Fan, S. & Lieber, C. M. Synthesis and characterization of carbide nanorods. *Nature* **375**, 769-772 (1995).
275 Munoz, E. *et al.* Synthesis of SiC nanorods from sheets of single-walled carbon nanotubes. *Chemical physics letters* **359**, 397-402 (2002).
276 Sun, X.-H. *et al.* Formation of silicon carbide nanotubes and nanowires via reaction of silicon (from disproportionation of silicon monoxide) with carbon nanotubes. *Journal of the American Chemical Society* **124**, 14464-14471 (2002).
277 Han, W., Fan, S., Li, Q. & Hu, Y. Synthesis of gallium nitride nanorods through a carbon nanotube-confined reaction. *Science* **277**, 1287-1289 (1997).
278 Shenoy, V. B. & Gracias, D. H. Self-folding thin-film materials: From nanopolyhedra to graphene origami. *Mrs Bulletin* **37**, 847-854 (2012).
279 Yu, M., Jayanthi, C. & Wu, S. Theoretical predictions of a bucky-diamond SiC cluster. *Nanotechnology* **23**, 235705 (2012).

280 Kim, K. J. *et al.* Structural and optical characteristics of crystalline silicon carbide nanoparticles synthesized by carbothermal reduction. *J Am Ceram Soc* **92**, 424-428 (2009).
281 Yushin, G. N., Cambaz, Z. G., Gogotsi, Y., Vyshnyakova, K. L. & Pereselentseva, L. N. Carbothermal Synthesis of α-SiC Micro-Ribbons. *Journal of the American Ceramic Society* **91**, 83-87 (2008).
282 Wieligor, M., Wang, Y. & Zerda, T. Raman spectra of silicon carbide small particles and nanowires. *Journal of Physics: Condensed Matter* **17**, 2387 (2005).
283 Perova, T. *et al.* Micro-Raman Mapping of 3C-SiC Thin Films Grown by Solid–Gas Phase Epitaxy on Si (111). *Nanoscale research letters* **5**, 1507-1511 (2010).
284 Naderi, N., Hashim, M., Saron, K. & Rouhi, J. Enhanced optical performance of electrochemically etched porous silicon carbide. *Semiconductor Science and Technology* **28**, 025011 (2013).
285 Zou, G. *et al.* Low-temperature solvothermal route to 2H-SiC nanoflakes. *Appl Phys Lett* **88**, 1913 (2006).
286 Powell, J. A. Crystal growth of 2H silicon carbide. *J Appl Phys* **40**, 4660-4662 (1969).
287 Nardecchia, S., Carriazo, D., Ferrer, M. L., Gutiérrez, M. C. & del Monte, F. Three dimensional macroporous architectures and aerogels built of carbon nanotubes and/or graphene: synthesis and applications. *Chemical Society Reviews* **42**, 794-830 (2013).
288 Schaedler, T. *et al.* Ultralight metallic microlattices. *Science* **334**, 962-965 (2011).
289 Si, Y., Yu, J., Tang, X., Ge, J. & Ding, B. Ultralight nanofibre-assembled cellular aerogels with superelasticity and multifunctionality. *Nature communications* **5** (2014).
290 Yin, J., Li, X., Zhou, J. & Guo, W. Ultralight three-dimensional boron nitride foam with ultralow permittivity and superelasticity. *Nano Lett* **13**, 3232-3236 (2013).
291 Chen, N. & Pan, Q. Versatile fabrication of ultralight magnetic foams and application for oil–water separation. *Acs Nano* **7**, 6875-6883 (2013).
292 Meza, L. R., Das, S. & Greer, J. R. Strong, lightweight, and recoverable three-dimensional ceramic nanolattices. *Science* **345**, 1322-1326 (2014).
293 Zheng, X. *et al.* Ultralight, ultrastiff mechanical metamaterials. *Science* **344**, 1373-1377 (2014).
294 Schaedler, T. A. *et al.* Ultralight metallic microlattices. *Science* **334**, 962-965, (2011).
295 Zou, J. *et al.* Ultralight multiwalled carbon nanotube aerogel. *Acs Nano* **4**, 7293-7302 (2010).
296 Qiu, L., Liu, J. Z., Chang, S. L., Wu, Y. & Li, D. Biomimetic superelastic graphene-based cellular monoliths. *Nature communications* **3**, 1241, (2012).
297 He, Y. *et al.* Freestanding three-dimensional graphene/MnO2 composite networks as ultralight and flexible supercapacitor electrodes. *Acs Nano* **7**, 174-182 (2012).
298 Harnisch, B., Kunkel, B., Deyerler, M., Bauereisen, S. & Papenburg, U. Ultra-lightweight C/SiC mirrors and structures. *ESA bulletin* **95**, 148-152 (1998).
299 Goodman, W. A., Mueller, C. E., Jacoby, M. T. & Wells, J. D. in *International Symposium on Optical Science and Technology.* 468-479 (International Society for Optics and Photonics).
300 Yin, J., Li, X., Zhou, J. & Guo, W. Ultralight three-dimensional boron nitride foam with ultralow permittivity and superelasticity. *Nano Lett* **13**, 3232-3236, (2013).